Aus der Klinik für Strahlentherapie
Direktorin: Frau Prof. Dr. med. R. Engenhart-Cabillic
des Fachbereichs Medizin der Philipps-Universität Marburg

Passive ion beam modulation techniques for particle therapy facilities utilizing active pencil beam scanning delivery systems

Inaugural-Dissertation zur Erlangung des Doktorgrades
Dr. rer. med.
dem Fachbereich Medizin der Philipps-Universität Marburg

vorgelegt von

Toke Printz Ringbæk
aus Toftlund/Nørre-Rangstrup, Dänemark

Marburg 2017

Angenommen vom Fachbereich Medizin der Philipps-Universität Marburg am: 19. Dezember 2017

Dekan: Herr Prof. Dr. Helmut Schäfer

Referenten: Herr Prof. Dr. Klemens Zink

Frau Prof. Dr. Rita Engenhart-Cabillic

1. Korreferent: Herr Prof. Dr. Christoph Bert

Manuscripts in Peer-Review Journals

Die vorliegende kumulative Dissertation stellt eine Zusammenfassung der Forschungsergebnisse dar, welche wie folgt in Fachzeitschriften publiziert wurden:

The present cumulative dissertation contains a compilation of the research results which were published in peer review journals in the following papers:

[1] Fluence inhomogeneities due to a ripple filter induced Moiré effect. **Ringbæk T. P.,** Brons S, Naumann J, Ackermann B, Horn J, Latzel H, Scheloske S, Gelonska M, Bassler N, Zink K and Weber U. Phys Med Biol 2015;7;60(3):N59-69

[2] Dosimetric comparisons of carbon ion treatment plans for 1D and 2D ripple filters with variable thicknesses. **Ringbæk T. P.,** Weber U, Santiago A, Simeonov Y, Fritz P, Krämer M, Wittig A, Bassler N, Engenhart-Cabillic R and Zink K. Phys Med Biol 2016;61(11):4327-41

[3] Modulation power of porous materials and usage as ripple filter in particle therapy. **Ringbæk, T. P.**, Simeonov, Y., Witt, M., Engenhart-Cabillic, R., Kraft, G., Zink, K. and Weber, U. Phys Med Biol 2017;62(7): 2892-2909.

Die Publikationen werden im Text, entsprechend der oben definierten Reihenfolge, mit den Nummern 1-3 referenziert. Die aufgelisteten Publikationen wurden verfügbar gemacht mit einer Abdruckgenehmigung von Institute of Physics (IOP) Publishing.

The publications are referenced in the text according to the order defined above with **the numbers 1-3.** The listed publications are printed with permission from Institute of Physics (IOP) Publishing.

Conference contributions

In der Lauf von der Dissertationsarbeit wurden die folgenden relevanten Konferenz-Beiträge präsentiert:

During the dissertation the following relevant conference contributions were presented:

PTCOG53, Shanghai, China, oral presentation

DGMP 2014 Dreiländertagung: Joint conference of the DGMP, SGSMP and ÖGMP, Zürich, Switzerland, oral presentation.

DKFZ symposium: ”Precision, Speed and Flexibility: New radiation detection methods for ion beam radiotherapy”, Heidelberg, oral presentation as invited speaker.

BiGART2015, 13th Acta Oncologica Symposium, Aarhus, Denmark, poster presentation.

DGMP 2015, Marburg, Germany, poster presentation.

DEGRO2016, Mannheim, Germany, poster presentation.

Zusammenfassung

Die Partikeltherapie ist eine Alternative zur konventionellen Strahlentherapie mit hochenergetischen Photonen, die aufgrund der physikalischen und strahlenbiologischen Eigenschaften der Partikelstrahlung besondere Möglichkeiten für eine konforme und schonende Tumorbehandlung bietet. Die Partikeltherapie wird entweder mit passiven oder aktiven Applikationsverfahren realisiert. Bei der letztgenannten Technik, dem Rasterscanning-Verfahren, werden Magnete verwendet, um einen feinen Partikel-Nadelstrahl über die laterale Ausdehnung des Tumors zu scannen. In Strahlrichtung erfolgt eine Energiemodulation des Strahls entsprechend der Tiefenausdehnung des Tumors. Hierdurch resultiert eine hochkonforme Dosisverteilung. Einige der gegenwärtigen Einschränkungen des Rasterscanning-Verfahrens sind längere Bestrahlungszeiten und eine Anfälligkeit der resultierenden Dosisverteilungen gegenüber interfraktionellen Bewegungen des Tumors. In Synchrotron-basierten Partikeltherapiezentren ist die Bestrahlungszeit direkt mit dem Strahldurchmesser und der Breite des Bragg Peak korreliert. Die Zeit, die vom Beschleuniger benötigt wird um die Energie der Partikel zu ändern bestimmt im Wesentlichen die Bestrahlungszeit des Patienten. Die Zahl der Energieschritte die erforderlich ist, um für einen typischen Tumor eine homogene Dosisabdeckung zu erreichen, kann insbesondere für Ionen, die schwerer als Protonen sind, in der Größenordnung von Hunderte liegen. Mit der Verbreiterung des primären Bragg-Peaks durch den Einsatz von passiven Energiemodulatoren kann die Anzahl der Energieschritte gesenkt werden, was nicht nur die Bestrahlungszeit reduziert, sondern auch eine höhere Partikelfluenz pro Energieschritt zur Folge hat, was zu einer höheren Präzision in den Strahlüberwachungssystemen führt.

Diese Arbeit befasst sich mit der Implementierung derartiger passiver Energiemodulatoren, insbesondere des Ripple-Filters. Eine erste Generation von Ripple Filtern wird derzeit in der Kohlenstoff-Ionen-Therapie in Deutschland, Italien, China und Japan eingesetzt. Diese Ripple-Filtern besteht aus feinen 1D Rillen, die auf einer homogenen Materialschicht aufgebracht sind. Diese Materialschicht führt zu einer unerwünschten zusätzlichen Streuung der Partikel. Darüber hinaus sind 1D Ripple-Filtern aufgrund des Herstellungsprozesses auf eine maximale Dicke von 3 mm beschränkt. Eine neue, zweite Generation von Ripple-Filtern wurde entwickelt mit 2D Strukturen. Im Vergleich zum alten

Design sind die Auflösung und die Massenverteilung deutlich verbessert, wodurch Streueffekte und damit die resultierende laterale Strahlbreite reduziert wird. Mit dem 3D-Druck Methode für die Herstellung ist die erzielbare Dicke der Ripple-Filter höher, und als Ergebnis können eine größere Breite des Bragg-Peaks und damit kürzere Bestrahlungszeiten erreicht werden. Das neue 2D-Design ist vermutlich auch bei Proton-Behandlungen verwendbar, bei denen bislang keine Ripple-Filter verwendet werden.

In dieser Dissertation wird eine methodische Bestrahlungsplanungstudie mit Anwendung der zweiten Generation von Ripple-Filtern vorgestellt. Es wurde festgestellt, dass Bestrahlungspläne mit 4- und 6-mm- dicken 2D- Ripple-Filtern für die untersuchten Fälle vergleichbare dosimetrische Ergebnisse in Bezug auf die Dosishomogenität und Konformität im Zielvolumen liefern, wie die derzeit eingesetzten 3 mm dicken 1D- Ripple-Filter, aber mit deutlich reduzierten Bestrahlungszeiten: in Vergleich zu dem 3 mm 1D-Ripple-Filter senken die 4 und 6 mm 2D-Ripple-Filter die Bestrahlungszeit um 25-30% bzw. 45-49%. Die Dosishomogenität und -konformität sind für dünnere Ripple-Filter etwas besser, aber für alle Filter wurden klinisch akzeptable Ergebnisse erreicht. Die Ergebnisse sind im Allgemein besser für höhere Eindringtiefe wegen Streuungseffekte. Die Untersuchungen zeigen aber auch, dass der Einsatz der 2D-Ripple-Filter für sehr kleine und oberflächennahe Tumore kritisch ist, d.h. zu klinisch nicht akzeptablen Dosisverteilungen führen kann. Neben der eigentlichen Geometrie der Ripple-Filter sind der Durchmesser des Partikelstrahls sowie die Fokussierung des Strahls beim Auftreffen auf den Ripple-Filter entscheidende Einflussgrößen für eine optimale Wirkung der Filter. Auch diese Untersuchungen sind Teil der vorliegenden Dissertation.

Neben den neuen 2D-Ripplefiltern sind im Rahmen der Arbeit auch poröse Materialien wie Schaumstoffe und Lungenersatzmaterialien experimentell und theoretisch untersucht worden, die als passive Energiemodulatoren in ähnlicher Weise wie Ripple-Filter verwendet werden können und darüber hinaus auch die Reichweite der Partikel verändern („Range Shifter”). Der Einsatz dieser Materialien könnte zukünftig bei oberflächennah gelegenen Tumoren zu einer geringeren Aufstreuung des Strahls und damit zu einer verbesserten Dosiskonformität im Patienten führen.

Diese Arbeit enthält außerdem einen kurzen Ausblick mit einer Perspektive auf andere Methoden, die die Energieveränderungen vom Beschleuniger reduzieren könnten, sowie Kommentare zu zukünftige Designs von passiven Energiemodulatoren.

Summary

Particle therapy (PT) cancer treatment is an alternative to conventional radiotherapy with the possibility for more conformal and tissue sparing treatments. PT is realized using either passive or active beam delivery methods. With the latter, also coined the scanned beam technique, magnets are used to cover the target laterally and for in-depth variation energy modulation is deployed, making the dose delivery even more conformal. However some of the current limitations of scanned beams are the longer irradiation times and a sensitivity to intra-fractionally moving targets. In PT centers with synchrotrons the irradiation time is directly related to the spot scan size and the width of the Bragg peak (BP), with the time needed from the accelerator to change energy as the bottleneck. The number of energy shifts required to cover a typical tumour in a homogeneous manner can in particular for heavy ions be as large as many hundreds. By broadening the BPs through the use of passive energy modulators, the number of energy shifts can be lowered, which would not only reduce the irradiation time but also results in a higher particle fluence per energy step, leading to higher precision in the beam monitoring systems.

This work addresses the implementation of such passive energy modulators, in particular the ripple filter (RiFi). A “first generation” RiFi is currently used in carbon ion treatments in Germany, Italy, China and Japan. This first generation RiFi has 1D groove shapes, which requires a non-modulating base layer of material leading to unnecessary scattering. It is furthermore restricted to a maximum thickness of 3 mm. A new second generation RiFi with two-dimensional cone structures has been designed. Compared to the old design the resolution and the mass distribution are significantly improved, reducing the overall lateral beam width. Using 3D printing for manufacturing, the obtainable RiFi thickness is higher, with further BP widening and shorter irradiation times as a results. The new 2D design is thought to be usable in treatments with protons as well, where RiFis as of now are commonly not used in proton treatments.

In this thesis, we show a methodological presentation of planning with the second generation RiFi design. It was found that treatment plans with 2D RiFis with 4 and 6 mm thicknesses yielded for the studied cases comparable dosimetric results to the standard 3 mm thick RiFi in terms of plan homogeneity and conformity but with significantly reduced irradiation times: Compared to the 3 mm RiFi, the 4 and 6 mm RiFis lower the irradiation

time by 25-30% and 45-49% respectively. Plan homogeneity and conformity were slightly improved for thinner RiFis but satisfactory results are obtained for all cases with RiFi performances in general increasing with penetration depth due to straggling and scattering effects. Certain plans for 6 mm RiFis indicate that there might be an upper limit on the RiFi thickness in treatments of small and very superficial tumours.

The work of this thesis also continues the investigations of the RiFi-induced fluence inhomogeneities and dose range inhomogeneities begun in the author's master thesis and covers new findings in this topic related to the beam spot sizes and the ion optical focusing of the beam.

Lastly, during the thesis, plates of porous materials such as foams or lung substitutes will be shown to be usable as passive energy modulators in a manner similar to RiFis and to furthermore function as a range shifter, which placed close to the patients leads to reduced beam penumbras for low penetration depths.

This work furthermore contains a short outlook with a perspective on other methods reducing the energy shifts as well as comments on new future designs of energy modulators.

Table of Contents

TABLE OF CONTENTS

Abbreviations

3DS:	3D-Schilling Prototypen GmbH, Sondershausen, Germany
AUH:	Ernst-Abbe-Hochschule, Jena, Germany
BAMS:	Beam Application and Monitoring System
BP:	Bragg Peak
BURMS:	Fa. BURMS, Jena. Germany
CNAO:	Centro Nazionale de Adroterapia Oncologica, Pavia, Italy
CNC:	Computer Numerical Control
CT:	Computer Tomography
CTV:	Clinical Target Volume
DDD:	Deph Dose Distribution
FWHM:	Full-Width Half-Maximum
GSI:	The Helmholtzzentrum für Schwer-ionenforschung, Darmstadt, Germany
GTV:	Gross Target Volume
HFJV:	High-Frequency Jet Ventilation
HIMAC:	Heavy Ion Medical Accelerator in Chiba, Chiba, Japan
HIT:	The Heidelberg Ionenstrahl-Therapiezentrum, Heidelberg, Germany
IES:	Iso-Energy Slice(s)
IMRT:	Intensity Modulated RadioTherapy (photons)
IMPT:	Intensity Modulated Particle Therapy
LEM:	Local Effect Model
MC:	Monte Carlo
MIT:	Marburger Ionenstrahl-Therapiezentrum, Marburg, Germany
MLC:	Multi-Leaf Collimator
MR:	Magnetic Resonance
MWPC:	MultiWire Propertional Chambers
NSCLC:	Non-Small Cell Lung Cancer
OAR:	Organ At Risk
PSI:	Paul Scherrer Institut, Villigen, Switzerland

ABBREVIATIONS

PT:	Particle Therapy
PTV:	Planning Target Volume
RBE:	Relative Biological Effectiveness
RiFi:	Ripple Filter
SIS:	Synchrotron Control System
SOBP:	Spread-Out Bragg Peak
SPC:	SPeCtra (of all particles, including fragments and secondary particles).
SPHIC:	Shanghai Proton and Heavy Ion Center, Shanghai, China,
TRiP:	TReatment Planning for Particles
VOI:	Volume of Interest

1. Introduction

1.1 Cancer and cancer treatments

Cancer is the joined name for a group of diseases where an abnormal cell growth caused by cell mutations is observed with the potential to invade other healthy parts of the body. Cancer is one of the highest-ranking causes of morbidity and mortality worldwide with ~8.2 million deaths related to cancer observed in 2012 (World Cancer Report 2014). The same year 14 million new cases worldwide were reported and the number is expected to rise with about 70% over the next 2 decades to 22 million, making cancer an increasing health issue (World Cancer Report 2014).

Depending on the specific patient cases, cancer is treated with surgery, chemotherapy, radiotherapy or a combination of these. The aim for the treatment can either be curative with the goal to ultimately cure the patient or when this not possible palliative, where the goal instead is to improve the quality of life for the patient and relieve the patient of some of the pain related to the disease. A successful curative treatment requires the removal of the tumor or at least a termination of the tumor's ability to grow and to spread.

After surgery, radiotherapy plays the most frequent role in cancer treatments with more than half of all patients with localized malignant tumors treated with radiation (Schardt et al 2010). In what is often coined “conventional” radiotherapy (simply because it was the first to be clinically used), photon radiation with energies in the MeV range is deployed to kill the tumor cells. While one can also apply the irradiation by internal means by inserting a source inside the tumor region (brachytherapy), this work focus only on external irradiation generated by particle accelerators.

1.2 Treatment planning in radiotherapy

Treatment planning in radiotherapy requires a rendition of volumes of interest (VOIs), such as the tumor volume and relevant organs at risk (OAR). Their locations are assessed by CT and/or MR images from which 3D contours of all VOIs are drawn. The dose is typically optimized and evaluated relative to the planning target volume (PTV), based on the macroscopic tumor extension or gross target volume (GTV) together with an additional margin called the clinical target volume (CTV), which accounts for the spread of the cancer cells beyond the visual tumour. The plan optimization is performed for a prescribed fraction

dose and takes into consideration the tolerance doses of the surrounding normal tissues and OARs. The number of fields, their corresponding directions and (in the case of particles) their fluence are obtained through the optimization process by the aim of giving the prescribed dose in a homogeneous manner to the PTV and at the same time spare the OARs and the surrounding normal tissue as much as possible. The biggest challenge in treatment plan optimization is thus the presence of multiple conflicting objectives, such as to cover the PTV in a satisfactory manner, avoid under- or over-dosage, spare multiple surrounding organs and all affected normal tissue and minimize the complexity and delivery time of the treatment (Baumann et al 2016). A plan should furthermore be robust, meaning the calculated and the delivered dose must be in agreement, also in the presence of various uncertainties and systematic errors (McGowan et al 2015).

1.3 Particle therapy and its clinical benefits

Particle therapy (PT) cancer treatment is an alternative to conventional radiotherapy (Wilson 1946), which is becoming increasingly common throughout the world with more than 137.000 patients treated worldwide and ~64 centers currently in operation with many more under construction (PTCOG 2016). PT has many advantages over conventional radiotherapy; most importantly it presents a better control of the dose distribution in the patient. Unlike photons, where the dose deposited after an initial dose build-up decreases with penetration depth with no finite range, particles have a well-defined range in matter beyond which no dose is deposited for protons and only a small dose for heavy ions (Kraft 2000, Schardt et al 2010). This range depends on the kinetic energy of the particle and can be fixed with millimeter precisions in the clinical setting. The energy loss of particles in matter – the stopping power theory – is well-described by Bethe (Bethe 1930) with corrections of Lindhard and Scharff (Lindhard and Scharff 1961), Barkas and Andersen, Bloch and others. For more detail see (Ziegler et al 1999, Kraft et al 2000). It is well-known that most of the particle dose is deposited in a sharp peak near the end of the particles' range; the Bragg peak (BP) (Bragg 1905). PT thus have the potential to enable better treatment of tumors near dose-sensitive organs or normal tissue, such as in skull-base chordomas. When using PT compared to conventional radiotherapy, high conformity of the high-dose regions to the PTV can be achieved with fewer beam directions, leading to significantly lower exposure of normal tissues to low and intermediate doses (Baumann et

al 2016). A reduction in integral dose to healthy normal tissue by up to 65% can be obtained even when compared to modern IMRT (Lomax et al. 1999, Nill et al 2004, Loeffler et al. 2013). PT thus allows for a more conformal dose distribution, increasing the therapeutic window between the dose response of the tumor and the complications of the normal tissue.

Protons are insofar the most used particles for PT, mainly since they are the least complex choice; one issue is that larger and much more expensive machinery is needed in order to use heavier ions in a clinical setting, in particular if a moving gantry is desired. On the other hand, the broadening effects of protons are approximately 3.5 times larger than for carbon ions for the same penetration depth due to differences in the charge-to-mass ratio and the lower proton energies for the same range (Weber and Kraft 2009). The scattering of particles are composed of many small-angle Coulomb scatterings with the electrons of the target nuclei and rare larger-angle scatterings due to collision with the nuclei themselves. The former is well described by Moliére's multiple scattering law (Moliére 1948, Bethe 1953) or the simpler Highland-approximation (Highland 1975, Highland 1979). Due to being scattered less, heavier ions than protons offer an even more precise dose delivery. However, heavy ions colliding with target nuclei have a possibility of fragmenting into a number of different, smaller isotopes with a wide energy distribution and a greater range than the primary ions. This leads to dose from such fragments being deposited after the BP, resulting in the so-called fragmentation tail, which is higher the heavier the primary ions. On the plus side, certain such radioactive isotope fragments can be used for PET imaging to estimate the in vivo range of the particle beam [Enghardt 1999].

Another advantage of heavier ions compared to protons is based on the fact that the same physical dose deposited by heavy ions has a higher cell-killing effect as compared to photons or even protons (IAEA 2008), which results in a higher relative biological effectiveness (RBE). DNA-damage from higher RBE beams is less dependent on the presence of oxygen, so treatments of hypoxic tumours in particular might benefit from this (Ma et al 2013). RBE is however still under scrutiny with clinical trials severely needed (Baumann et al 2016).

Due to the statistical nature of scattering events, fluctuations occur in the energy deposited by a particle traversing an absorber element and the net energy loss must be described by a probability distribution (Bohr 1915, Vavilov 1957, Ahlen et al 1980). Because of this energy loss straggling, the stopping positions of particles with the same initial beam energy

are shifted in respect to each other and the resulting BP is enlarged. This effect is larger for higher energies and larger penetration depths as well as for lighter particles due to their lower mass. Still, the general width of a BP in the beam direction is narrow; less than 1 mm full-width half-maximum (FWHM) for carbon ions with initial energies below 360 MeV/u (Bourhaleb et al., 2008). Thus, in the clinical setting it is required to deliver the beam in a manner so that the BP is “spread out” into a SOBP.

1.4 Particle therapy beam delivery techniques and irradiation times

PT is realized using either passive or active beam delivery methods with the latter, also coined pencil beam scanning, being the preferred choice in most new facilities. Solutions incorporating “hybrid-techniques” are also fairly frequently used (Chu et al 1993).

Passive modulated beams are shaped to encompass the PTV with scatter elements. A range compensator or bolus shape the distal edge to the target and cut blocks or MultiLeaf Collimators (MLCs) shape the beam in the transversal plane orthogonal to the beam direction. In active beam scanning systems, the lateral displacement of a pencil beam is done by fast scanning magnets while the displacement in depth is done by changing the beam energy either with a degrader (passive modulation) or the accelerator (active modulation) (Haberer et al. 1993, Goitein et al 1983, Kanai et al 1980). Multiple iso-energy slices (IES) of a finite step size in depth are used, each yielding a BP located at a specific target depth. A three-dimensional reconstruction of the tumor is divided into individual IES and the treatment proceeds slice by slice, starting from the distal slice (Weber et al 2000).

Generally, compared to the passive scattering technique, active beam scanning can reduce integral dose (Shiomi et al 2016) and make field patching techniques and IMPT possible (Schippers and Lomax 2011) as well as making available more complex dose distributions and robust or risk adapted optimization (Lui 2012). There is no need for changing or producing patient specific components. Less material in the beam path reduces the amount of undesired generated secondary particles, such as neutrons. It has been shown that neutrons emerging from passive scattering systems can cause a secondary dose contribution ten times higher as for full active scanning systems (Yan et al. 2002. Agosteo et al. 1998), although in modern passive scattering facilities the beam is “cleaned” of undesired particles by deflection units before hitting the patient (Gottschalk, 2006).

Current limitations of the pencil beam scanning technique are the longer irradiation time, its

sensitivity to intra-fractionally moving targets and that the lateral beam penumbra in general is broader than achievable with cut blocks or MLCs. For pencil beam scanning, the total time required for target irradiation is directly related to the spot scan size and the width of the BP, with the time needed for the accelerator to change the beam energy as the bottleneck. The BPs are especially very sharp at low penetration depths and for heavy ions an unreasonably large number of up to hundreds of individual EIS is required for a homogeneous irradiation of the tumor to be obtained. This costs much more time than what is achieved with passive beam application systems and has other disadvantages related to intra-fractional motion effects as well, such as the interplay effect where the scanning of the beam interacts with target motions (Phillips et al 1992, Bert et al. 2008, Bert & Durante 2011). For modern cyclotrons, the energy can be changed in a matter of milliseconds with a fast degrader like at proton therapy facilities such as the Paul Scherrer Institute (PSI), Villigen, Switzerland (Lomax 2004, Pedroni 2011) and the Rinecker Facility, Münich, Germany. For heavier particles, synchrotrons insofar remain the only suitable accelerator choice for treatment facilities. For a synchrotron, the energy change is composed of the dumping of the beam, the injection and acceleration of a new one and lastly the extraction. Each energy change can take some seconds so here techniques to reduce the number of energy changes are required. A solution is using a passive ion beam modulater to enlarge the BP width, either in the form of a plastic plate with beam-modulating structures on the macro-scale (section 1.5 and 1.6) or a block of porous material with beam-modulating structures on the micro-scale (section 1.7).

1.5 Ripple filters; usage and production

Lowering the accelerator energy steps without taking further action produces dose ripples in the superimposed SOBP. Therefore, a so-called ripple filter (RiFi) was introduced in the late 90s for carbon ion therapy (Weber & Kraft 1999). The RiFi is a thin passive (meaning static) energy modulator with a periodic structure of typically 1.5 or 1.6 mm. Due to alternating scattering of the particles, depending on where they hit the inhomogeneous mass distribution of the RiFi, the BP is extended and smoothed to a Gaussian peak with a larger half-width, which reduces the number of energy steps necessary to cover the target and thereby shortens the overall irradiation time. Apart from counteracting some of the issues concerning intra-fractional motion and increasing patient comfort, this also results in a

higher particle fluence per energy step and consequently higher precision in the beam monitoring systems (Krämer et al 2000). The BP width enlargement depends on the maximum RiFi thickness. It is our experience that a RiFi with an optimized shape and material density between 1.1 and 1.2 g/cm^2 of a certain thickness in mm enables the same size in mm of the energy steps. This is clinically proven for 3 mm thick RiFis and simulated for thicker ones (Ringbæk et al 2014). Thus, the 3 mm thick RiFi of a one-dimensional pin structure design which have been applied for carbon ion beam treatments for years at the Helmholtzzentrum für Schwerionenforschung (GSI), Darmstadt, Germany, at the Heidelberg Ionenstrahl-Therapiezentrum (HIT), Heidelberg, Germany and at the Shanghai Proton and Heavy Ion Center (SPHIC), Shanghai, China, makes up to 3 mm energy steps in treatment planning possible. With a similar design but a slightly cruder triangular shape RiFis are also used for patient treatment at Centro Nazionale de Adroterapia Oncologica (CNAO), Pavia, Italy (Bourhaleb et al 2008) and the Heavy Ion Medical Accelerator in Chiba (HIMAC), Chiba, Japan (Furukawa et al 2010).

However, this “first generation” design has two shortcomings. First, the one-dimensional pin structure demands a base layer of non-modulating homogeneous material to hold together the structure. This base layer of typically 0.3 to 0.5 mm thickness is an unnecessary source of scattering and gives an unintended lateral widening of the scanned beam spots. Second, unless one uses a simple triangular pin structure, thicknesses of more than the established 3 mm cannot be realized, in turn due to the mechanical process of how the RiFi is currently made by cutting the pin structure out of a plastic or an aluminum plate using a Computer Numerical Control (CNC) machine and a vacuum table.

To overcome these shortcomings a new second generation RiFi has been designed (Weber et al n.d., Weber et al 2015). Using instead a two-dimensional pin structure, the need for a base layer is eliminated and the peak resolution is improved compared to the 1D design. By additionally using 3D printing techniques like rapid prototyping or stereolitheography (History of Stereolithography 2011) larger thicknesses can be obtained in a shorter time span and for a reduced cost than with the CNC method. Building an object up in layers instead of using “subtractive” techniques allows many more geometric possibilities and a better resolution. With the availability of medical-grade materials printed with sub-millimeter accuracies, proton beam modulation using printed plastic devices has been proven possible (Lindsay et al 2015, Lindsay 2016).

1.6 Investigation topics of ripple filters

There are small avoidable as well as unavoidable issues connected to the insertion of a RiFi of any design in the beam path in scanned beam treatments, which have to be taken into account before implementation, at best already at the commissioning stage. Increasing the RiFi thickness may enlarge the effect of some of these issues, so additional investigations are required before the possible superiority of the second generation design can be established.

1.6.1 Lateral beam scattering of ripple filters

One obvious unavoidable drawback is the increase of material in front of the patient and the related enlargement of the angular beam spreading. There are two different contributions to the angular beam spreading which have to be considered in practice (Schardt et al 2010, Weber and Kraft 2009). The first is the one coming from the materials in front of the patient, e.g. in the beam application and monitoring system (BAMS) with beam shaping devices such as a RiFi and the second is the scattering in tissue between the patient surface and the end of the particle range. At higher beam energies, the scattering within the patient becomes more critical and at large penetration depths the contribution from the material in front of the patient becomes partly negligible compared to the scattering in tissue (Schardt et al 2010). For low energy beams, the scattering before the patient is the dominant factor, since even a small angular spread results in a large broadening of the beam spot due to the relative long distance (as much as 1 meter) between the scattering elements and the patient. Therefore, the material in the beam path in front of the patient should be kept to an absolute minimum and be as close to the patient as possible. A RiFi for 3 to 6 mm energy steps typically requires from 0.2 to 0.4 mm g/cm^2 additional plastic material in the beam path, respectively. The new RiFi design offers a larger filter effect for less material and the removal of the base layer ensures that all the material of the RiFi is used for beam modulation. One can counteract the beam broadening prior to the patient by treating the patient closer to the exit nozzle, even at non-isocentric setups (Jelen et al 2013, Gevillot 2015). Alternatively or additionally, one can use a range shifter and higher initial particle energies for the same penetration depth as without the range shifter (Titt et al 2010, Weber et al 2014).

For scanned protons, the scattering prior to the patient is much more critical than for carbon

ions, which is one reason for why RiFis are not normally used in proton treatments. Another reason is that protons with their much larger energy loss straggling effect already for most energies have BPs so broad that a 3 mm thick RiFi does not result in any further relevant broadening. The new 6 mm thick 2D RiFi on the other hand broadens the proton BP enough for it to yield a potential clinical benefit in terms of irradiation time reduction and an increased robustness for moving targets, in particular for low energies.

1.6.2 Ripple filter induced fluence and dose range inhomogeneities

The inclusion of the inhomogeneous RiFi mass distribution in the beam path can lead to similar inhomogeneities in the particle fluence distribution after the RiFi. Up to a certain distance from the RiFi (<60 cm for carbon ions and <17 cm for protons) and for specific beam settings, these inhomogeneities can be seen at the target surface (Ringbæk et al 2014). Additionally, since the particles are traveling through a variable amount of material depending on where they hit the RiFi, their range is changed accordingly, which in turn can lead to observed dose range inhomogeneities within the patient at the end of the particle ranges for carbon ion beams at RiFi-to-patient distances less than 20 cm with initial beam energies smaller than 200 MeV/u (Ringbæk et al 2014). Even though these are not relevant issues for isocentric treatment distances at most facilities, certain special situations can occur where inhomogeneities *are* observed clinically, such as when the pencil beam width at the RiFi plane is small compared to the RiFi structure period, e.g. when the beam is focused near the RiFi plane by the ion optics as will be shown in this work (section 2.3). Also, since one might want to treat the patient closer to the exit nozzle in order to reduce the lateral beam width, it is important to investigate RiFi-induced fluence inhomogeneities and how far from the patient the RiFi needs to be placed.

1.6.3 Thicker ripple filters in treatment planning

Having understood and considered the various possible non-beneficial physical phenomena RiFis can induce when used in treatments, it is then important to establish in a clinical setting the actual benefit of the RiFi for various tumour types and patient cases. In this work in particular the focus will be on showing the aptitude of the new thicker 2D RiFis in treatment planning of selected relevant patient cases compared to the in-use 3 mm 1D RiFi. Proving the usefulness of the new RiFi design in treatment planning is a key step to

implement this design in actual treatments and will be the main research topic of this thesis. There is in this regard in particular one issue that one has to be aware of. Since a tumor shape is often irregular, to cover it conformally with IES can be challenging and can be done better with many thin slices than with fewer larger ones. The challenge increases the smaller the tumour is. Therefore, for small and irregular tumours, IES with a large in-depth length, such as the ones made possible with the 6 mm thick RiFi, could result in so-called “dose spikes” outside the PTV with a slightly higher dose coverage in the near-adjacent normal tissue. This has to be investigated prior to opting for a thicker RiFi and could potentially set a limit for how thick a RiFi should be or be a reason for having a range of RiFis with different thicknesses available for different treatments.

1.7 Porous materials and potential clinical usage as a complementary ripple filter

It is known that porous materials with microscopic structures like foam, sponges, lung tissues and lung substitutes have particular characteristics, which differ from those of solid materials (Witt et al 2015, Titt et al 2015, Witt 2014, Sawakuchi et al. 2008). When an ion beam passes through a porous material a stronger straggling effect than expected for non-porous materials of the same thickness is observed and the BP is broadened depending on the size of the microscopic structure, the density of the material and its thickness. Porous plates thus represent another passive ion beam modulation technique to be used in particle therapy facilities similar to the RiFi, presenting new research topics. In addition, a porous plate can, when placed very close to the patient, be used as a range shifter, which as mentioned before reduces the BAMS scattering and improves the lateral fall-off of the scanned beams. To fully evaluate the possible usage of porous plates in a clinical setting, one first have to understand and quantify the effect of the modulation from these materials: A mathematical “binary voxel” model, experimental data and MC simulations will be used to this end.

1.8 Treatment planning with particles in TRiP98

All treatment plans were performed with the treatment planning software TRiP98. TRiP98 was developed for scanned carbon ion beam radiotherapy during the GSI pilot project (Krämer et al. 2000; Krämer & Scholz 2000; Krämer & Durante 2010) and is the basis for the commercial particle therapy planning system Syngo PT Planning (Siemens Healthcare).

For the optimization of the dose, the PTV is divided for each field into IES corresponding to a constant initial energy of the ions and for each IES into voxels. The optimization then prescribes a certain number of ions to each voxel in order to achieve a homogeneous dose distribution with mono-energetic Bragg curves super-positioned to generate the SOBP. The planning procedure requires as input the 3D information of the particle composition at each position in the field. The main input is the depth-dose distribution as a function of target depth of each pencil beam at all available energies (DDD). Optionally, double-Gaussian FWHMs can be given to approximate the widening of the lateral beam width with penetration depth inside the patient. Synchrotron Control System (SIS) tables contain the energy steps and the associated focus and intensity steps accessible from the accelerator as well as the initial beam width of each pencil beam just leaving the BAMS. Lastly, one can provide files containing energy spectra and related histograms of the various particles created when the projectile undergoes nuclear interactions in the traversed matter (SPC).

In order to account for the lateral dose fall-off at the PTV edges, TRiP98 has a lateral "virtual contour extension" implemented; a lateral margin in which additional dose spots are allowed around the PTV during the optimization phase. This contour extension is defined as an adjustable fraction of the beam's FWHM at the isocenter (Krämer et al 2000). In the standard version, no contour extension in the longitudinal direction can be given, with the argument that for carbon ion beams, even when using a 3 mm 1D RiFi, the longitudinal dose fall-off is much steeper than in the lateral direction. When using a passive energy modulator for energy steps larger than 3 mm (RiFis or porous plates) or when using lighter ions like protons, this no longer holds true.

TRiP98 can handle biological optimization using Local Effect Model (LEM) (Krämer & Scholz 2000), although for this work the radiobiological effects of the ions is of minor relevance and will not be described in detail.

1.9 Monte Carlo codes SHIELD-HIT12A and FLUKA

To solve the equations in the underlying theory of particle transportation can be a very complex task for anything but very simple geometries. Often the equations can only be solved numerically. A frequently used tool for this is Monte Carlo (MC) simulations. In the MC method, originally presented by Metropolis and Ulam (Metropolis 1949), the equations are solved by a large number of repeated random sampling of all possible outcomes. MC

codes have a widespread use across fields, only limited by computer power, and while MC codes are normally deemed too slow to be used directly for treatment planning, this is bound to change in the near future with GPU-based codes (Jia et al 2012) and other solutions (Iancu et al 2015).

For ion therapy, the MC codes most commonly used are FLUKA (Fassò et al., 2005, Böhlen et al 2014), Geant4 (Agostinelli et al., 2003, Allison et al., 2006) and SHIELD-HIT12A (Bassler et al 2014). While the latter has been predominantly used in this work, simulations with FLUKA will also be presented.

SHIELD(-HIT) is a MC code specialized for ion therapy., which strains from the SHIELD code (Dementyev et al 1999). The newer SHIELD-HIT(12A) has been validated in works concerning particle therapy (Ringbæk et al 2014, Bassler et al. 2014 and 2008, Hansen, Lühr, Herrman et al 2012, Hansen, Lühr, Sobolevsky et al 2012, Lühr et al. 2011). SHIELD-HIT12A can handle beam divergence and beam (de)focusing. This has been used to investigate RiFi-induced dose inhomogeneities as a function of ion-optical beam focusing. The (de)focusing implementation is based on a model for the ion optical phase space distribution in a simplified form of the Fermi-Eyges formalism (Eyges 1948, Hollmark et al. 2004). In SHIELD-HIT12A, a RiFi or a similar structure periodic in one or two dimensions is simulated by using an external data file containing the periodic structure information and the position, while a solid slab of the material in question is simulated at the place of the RiFi. When a particle hits the beginning of the slab at a specific point it is shifted along the axis of the primary beam direction according to the periodic structure information at this point, ignoring the surrounding material (Bassler et al 2010). This method introduces an error proportional to the angle between the incoming particle before the shift and the normal vector of the structure, which is negligible compared to the angular spread from the BAMS scattering and the initial divergence.

Physical base data files for TRiP (DDD and SPC) can be generated in SHIELD-HIT12A, which makes it possible to include in treatment plans different ion types, new RiFis or other beamlines than the GSI one already available in the TRiP library. Furthermore, accelerator raster files for the distribution of the primaries obtained in TRiP can be used as input for simulations. When generating the base data, the simulation of the full periodic structure of the RiFi is replaced with a random sampling over the structure and pencil beams are used in the simulations in order to get correct lateral beam distributions (Bassler et al. 2013).

FLUKA is not a dedicated MC code for particle therapy and has to balance speed and accuracy while remaining as general in terms of energy and particle type as possible. While RiFis can be simulated in FLUKA by the implementation of a special user routine by Y. Simeonov, partially inspired by the routine implemented in SHIELD-HIT12A, in this work FLUKA was used only to simulate porous materials with microscopic fine structures represented by low- and high-density voxels. The external Pydicom v. 0.9.9 module (Mason 2011) was used to import binary CT data and convert them to a 3D voxel grid.

2. Summary of the results

This chapter summarizes the results of the present dissertation, mainly the ones presented in the corresponding peer-reviewed papers but results from work task leading up to those as well as relevant follow-up results obtained afterwards are additionally shown.

First follows a description of the software tools used, including the full simulation model of the BAMS at MIT. Then the results of each of the published papers [1-3] will be summarized with knowledge of the content of the corresponding papers required for a full understanding. All published figures and tables are only referred to and not given in this chapter, although two yet unpublished figures providing further valuable information are presented to be evaluated as work for this dissertation.

2.1 Establishment of software tools

While DDD files and SPC files for TRiP98 could already be generated using SHIELD-HIT12A (Ringbæk et al 2014) prior to this work, the scripts handling the simulation setup and the data processing have been improved. The generation of SIS files was included in the routines to get realistic accelerator energy step sizes matching thicker RiFis. A rewriting of the DDD fitting procedure was performed and by scaling the lateral profile with the radius, fitting *D(r)*r* instead of just *D(r)*, a more precise parametrization was obtained. *D(r)*r* are fitted with a double Gaussian distribution (Parodi et al 2013), which is more precise than using a single Gaussian distribution.

The generated base data from SHIELD-HIT12A was carefully benchmarked. Base data generated for the in-use 1D 3 mm thick RiFi was compared with DDD files for this RiFi design already present in the TRiP98 database with no observable difference. In TRiP98, the RiFi implementation is done by convolution of the DDDs for pristine BPs with a RiFi transfer function. While this method was used for benchmarking the MC generated DDDs for thicker RiFis, it was opted for using MC generated base data for the treatment planning. This is thought to be more precise and provides additionally information about the lateral scattering of the beam and the fragmentation sprectra.

PyTRiP (Toftegaard et al 2014), a graphical user interface for TRiP98, was used for plan visualization and evaluation with minor bug-fixes of the software as part of this work.

As mentioned in section 1.8, TRiP98 has a lateral contour extension implemented but not a

longitudinal one. For carbon ion DDDs along the beam axis, a 40% and 58% increase in the 20%-80% longitudinal dose fall-off was found for the lowest (70 MeV/u) and the highest (430 MeV/u) energy available for treatment (section 2.1.1., **article 2**) when using a 6 mm thick RiFi instead of a 3 mm thick one. It was thus deemed necessary to implement a longitudinal contour extension and a slightly modified in-house version by Dr U. Weber with longitudinal contour extensions included has been used throughout this work. The new version was extensively tested: For fixed longitudinal contour extensions, the lateral contour extensions have been evaluated and vice versa. In **article 2** it was indeed found that longitudinal contour extensions of 0.9 to 2.8 times the isocenter FWHM could lower the relative dose ripples and dose spikes and thereby improve the planning conformity.

2.2 Beamline model

Because of the scattering and energy straggling effects in the BAMS, the entire BAMS had to be included in detail in the MC simulations. The design by Siemens currently in use at the Marburger Ionenstrahl-Therapiezentrum (MIT), Marburg, Germany, and based on the original design from GSI (Haberer et al. 1993) has been modelled in SHIELD-HIT12A previously by the author (Ringbæk et 2014). This model was improved by also adding the inhomogenic mass distributions in the multiwire proportional chambers (MWPCs) and by comparing simulated data to measurements. The 1.0 mm intermediate wire spacing in the MWPCs can result in systematic fluence ripples similar to those caused by a RiFi. Compared to these however, they are much smaller in amplitude and disappear after some centimeters distance. MWPC stripes are present at most centers and the effect is known and accounted for and not an issue relevant for treatment. The MWPCs also functions as passive energy modulators but the BP enlargement is negligible compared to straggling effects in the BAMS and the enlargement from dedicated passive energy modulators like RiFis, as tested in this work (**article 1**) as well as in other works (Baumann 2015).

In the FLUKA simulations, the scattering in the BAMS was taken into account using water in front of the beam with the same water-equivalent thickness as the BAMS.

Fluence inhomogeneities were measured in experiments with radiographic films (**article 1,** Ringbæk, Weber et al 2014) and therefore photometric films with envelopes were added in the MC simulations as the scoring volumes. The films were modelled with an inner polyester part and an outer gelatin part while the envelopes were modelled with an inner

PVC plastic part and an outer cellulose paper part. The geometric dimensions and densities for the individual parts were obtained by measurements and the chemical compositions estimated from available technical handbooks and/or the libdEdx library (Lühr et al 2012).
For most simulations, an initial beam divergence of 1 mrad was used. This value was later confirmed in **article 1** (see section 2.2) as a realistic choice.

2.3 Ripple filter induced fluence inhomogeneities

As mentioned in section 1.6.2, the RiFi structure can induce inhomogeneities in the fluence distribution after the RiFi. These were investigated prior to this work with MC simulated pencil beams focused at the isocenter (Ringbæk et al. 2014), which has since been backed up by measurements performed as part of this dissertation (Ringbæk, Weber et al 2014, Ringbæk, Brons et al 2014). An oscillating fitting procedure was developed to quantify the fluence inhomogeneities, fitting a product of a flat non-oscillating function and a sinusoidal oscillating function to 1D lateral Gaussian fluence profiles obtained by integration in one lateral direction of 2D fluence profiles. For details, the reader is referred to (Ringbæk et al. 2014). The inhomogeneity is then defined as $\Delta I/I = I_{max} - I_{min} / I_{mean}$, with (excluding the lateral fall-off region) I being the intensity (dose or fluence), I_{max} and I_{min} being the maximum and minimum intensity respectively and I_{mean} the mean value of the distribution or the maximum intensity of the non-oscillating function.
It was found that for specific distances from the RiFi, inhomogeneities from the mean dose are observed but that these are blurred out by scattering at a distance much smaller than the typical nozzle-to-isocenter distance and thus are without any clinical importance.

2.3.1 The Moiré effect

In what first appeared to be a contrast to what is stated above, it was seen at HIT that when focusing the scanned pencil beams sharply at the RiFi plane, lateral periodic fine structures in the fluence distribution were observed at the isocenter with clinically unacceptable $\Delta I/I>8\%$ (see figure 1, **article 1**). While the fluence inhomogeneities described above always have a period λ_{ripple} identical to the RiFi structure period λ_{RiFi}, the observed λ_{ripple} values at HIT are always magnitudes larger than that. They disappear when either the RiFi is removed or the beam spots in the RiFi plane is enlarged by shifting the longitudinal position of the ion optical focus away from the RiFi plane.

As presented in **article 1,** this phenomenon can be described as a Moiré effect: a pattern that occurs when one set of lines is superimposed on another where each differ in relative size, spacing or angle. This corresponds to a situation where beam spot sizes σ_x are smaller than λ_{RiFi}, such as when the beam is focused at the RiFi plane, if the scan step size λ_{scan} (the distance between two beam spots at the focus plane) are not equal to λ_{RiFi}. The resulting inhomogeneous periodic fluence distribution at the RiFi plane will then interfere with the inhomogeneous periodic RiFi mass distribution, with beam spots hitting either the RiFi peaks, the valleys or in-between. The sharper the focusing of the beam spots, the higher the values of the observed inhomogeneity.

From equation (1), **article 1,** the ripple period λ_{ripple} is given by the Moiré effect as:

$$1/\lambda_{ripple} = 1/\lambda_{RiFi} - 1/\lambda_{scan} \quad (1)$$

While λ_{ripple} is of minor clinical interest compared to $\Delta I/I$, it can be confirmed that it is indeed a Moiré effect causing the inhomogeneities by comparing values of λ_{ripple} from simulations with those found by measurements. Experiments and MC simulations were thus used to prove the Morié effect; the latter making it possible to investigate a larger range of parameter values than with experiments alone. The ion optic implementation in SHIELD-HIT12A was used to simulate focused pencil beams (section 2.2 in **article 1**). For both experiments and simulations, 150 MeV/u carbon-12 ions were used and fluence distributions obtained 30 mm in front of the isocenter were fitted with the mentioned oscillating fitting procedure in order to get $\Delta I/I$ and λ_{ripple} (examples are shown in figure 4, **article 1**, for experiments and in figure 3 and figure 5, **article 1,** for simulations). The first generation 1D RiFi was used, being the one implemented at HIT.

For a proper comparison of the experimental and simulated data, certain “uncertainties” had to be included. First, the scanning divergency not present in the simulations had to be taken into account. The scanning divergency at the HIT gantry is ~2% and by assuming a 2% change from the λ_{scan} value at the RiFi plane to the corresponding value at the isocenter, all simulated λ_{ripple} values were found to match equation 1. Second, the beam divergence as well as the beam spot sizes at the RiFi planes could only be roughly estimated in the experimental setting while beam spot sizes at any plane can be obtained by Gaussian fits in the MC simulations. By plotting simulated curves for two different beam spot sizes and for two different beam divergency values, representing the “minimum” and “maximum” expected values, this was also taken into account: Figure 6b, **article 1**, shows that the

experimental data best match the simulated data set with an initial beam divergency of 1 mrad, thus also confirming the estimation of section 2.1.

In figure 3 bottom figure, **article 1,** it is shown that a low ratio of σ_x/λ_{scan} leads to inhomogeneities in the BAMS and that an interference of this inhomogeneity with the inhomogenic RiFi mass distribution results in the Moiré effect observed at the isocenter with $\lambda_{ripple}>\lambda_{RiFi.}$ When an asymmetrically focused beam with a narrow beam width in one lateral direction only is used, the Moiré effect are observed only in the lateral direction in which the beam was narrow (post-publication results).

The inhomogeneity values $\Delta I/I$ are plotted as a function of σ_x at the RiFi plane for a fixed λ_{scan}=2.0 mm (figure 6a, **article 1**) and as a function of λ_{scan} for two different σ_x values (figure 6b, **article 1**). Figure 6a shows that the smaller the beam width at the RiFi plane, the higher the value of $\Delta I/I$. Figure 6b illustrates that local maxima and minima of $\Delta I/I$ occurs as a function of λ_{scan}. This comes from a combination of effects: 1) When λ_{scan} equals λ_{RiFi} times an integer, every pencil beam goes through an identical amount of RiFi material, suppressing the Moiré effect. 2) When λ_{scan} equals λ_{RiFi} times an integer and a half (here 2.4 mm), the pencil beams hit every second RiFi valley as well as every second RiFi peak, partly suppressing the Moiré effect. 3) The local minima from 1) and 2) lead to local maxima. 4) For $\lambda_{scan}\geq$3.2 mm $\Delta I/I$ values increase rapidly due to an inhomogeneous PTV coverage caused by a too large spacing between beam spots, independent of the Moiré effect. Post-publication, the Moiré effect was additionally investigated for the 2D RiFis with similar results. Due to the larger RiFi thickness, the inhomogeneity values were correspondingly larger and a shift of the curves caused by the slight difference in λ_{RiFi} (1.5 mm for 2D RiFis vs 1.6 mm for 1D RiFis) were observed.

2.4 Comparisons of carbon ion treatment plans for 1D and 2D ripple filters

In order to investigate the clinical relevance of thicker 2D RiFis and whether or not they can reduce irradiation time of treatments with a dosimetric performance equivalent to that of the 1D 3 mm RiFi, carbon ion treatment plans for 4 and 6 mm thick 2D RiFis and for the 3 mm thick 1D RiFi were calculated with the planning objective to deliver at least 95% of the prescribed dose to 98% of the PTV. The treatment planning was done with our in-house version of TRiP98 (section 1.8 and 2.1) with base data for each investigated RiFi generated

by SHIELD-HIT12A (section 1.9).

In TRiP98, spherical PTVs in water with arbitrary radii, locations and Hounsfield values can be "simulated" and a range (radii 20-36 mm at isocenter depths 60-175 mm) of such PTVs were used for a systematic analysis for plans with one to three fields. Plans were furthermore calculated for a cohort of selected patient cases composed by eight patients with peripheral stage I non-small cell lung cancer (NSCLC) (14.9-78.3 cm^3), four patients with skull base chordoma (72.4-203.4 cm^3) and three prostate cancer patients (54.5-75.9 cm^3). All NSCLC patients were previously treated with photon stereotactic body radiation therapy (SBRT) under high-frequency jet ventilation (HFJV) (Santiago et al. 2013, 2015). HFJV is a mechanical ventilative support technique where respiratory rates far greater than the normal value and very small tidal volumes prevent tumor movement and deformation with respiration, which could potentially allow for hypofractionated scanned particle beam therapy (Santiago et al. 2013). The chordoma and the prostate cancer cases were originally treated with carbon ions at the GSI pilot project (Schulz-Ertner et al. 2002, 2007, Nikoghosyan et al. 2011).

A λ_{scan} value of 2.0 mm was used, which in **article 1** is shown to sufficiently cover the PTV in a homogeneous manner. The energy step size was set equal to the maximum thickness of the RiFi in question (see section 1.5). For all plans the beams were focused at the set treatment isocenter 108 cm from the RiFi, so no Moirè-effect would be seen as per the results in **article 1** and all fluence inhomogeneities would be blurred out by scattering before reaching the patient. All plans were calculated using physically optimized dose since we found that the difference in dose coverage for various RiFis as well as for the RiFi-induced dose ripples and dose spikes are negligible when comparing physically and biologically optimized dose (see supplementary material of **article 2**). IMPT optimization was used for all plans. For the NSCLC cases a horizontal angle of 0 degree and an oblique-vertical of 45 degree (according to the two fixed beam lines at MIT) was used with some three-field plans additionally calculated. For the skull-base chordoma and the prostate cancer cases the two-beam configurations originally used at GSI were opted for (Schulz-Ertner et al. 2002, 2007, Nikoghosyan et al. 2011). Details on fields configurations, dose constraints and planning strategies are given in **article 2.**

For evaluation of the PTV coverage $V_{95\%}$, the volume receiving at least 95% of the prescribed dose, was used. To address the homogeneity of the PTV dose coverage and the

planning conformity, we opted for the homogeneity index HI and the conformity index CI as by Wu (Wu et al. 2003). For a given treatment plan the aim was to obtain for each RiFi similar values of $V_{95\%}$ and HI.

Table 1, **article 2,** shows the overall dosimetric performance of each investigated RiFi for 1-field spherical plans, averaged over all PTV radii, isocenter depths and contour extension values. Figure 2, **article 2,** shows the dosimetric indexes for selected spherical PTVs and for all the investigated patient cases. The PTV coverage was comparable between RiFis with a 0.1-0.7 percentage point difference. HI and CI values were comparable for the 1D 3 mm and the 2D 4 mm, while the 2D 6 mm RiFi resulted in a CI increase of 4%-14% and thus slightly less sparing of surrounding normal tissue. This is thought to be partly due to the slightly larger scattering effect of a thicker RiFi but in particular to the aforementioned dose spike effect (section 1.6), which is illustrated in figure 1, **article 2,** for 1- and 3- field treatment plans using 1D 3 mm RiFis and 2D 6 mm RiFis for a spherical PTV with radius 36 mm at an isocenter depth of 60 mm. Dose spikes are seen in the dose distribution near and around the distal edge of the PTV for the 1-field 2D 6 mm RiFi case with more fields reducing this effect. Independent of fields, for more deep-seated tumors the RiFis perform better because for deeper penetration depths straggling and scattering effects blur out the inhomogeneities and broadens the BPs and for larger PTVs because such PTVs are less challenging to cover with the rectangular IES. This benefits in particular the thickest RiFi and the difference in performance between the RiFis decreases with increasing PTV volume and penetration depth.

The DVHs for the three groups of patient plans are shown in figure 3, 4 and 5, **article 2** for the 1D 3 mm RiFi and the 2D 6 mm RiFi for comparison. For the smallest NSCLC cases a slight dose increase to certain ribs was observed for the thicker RiFi but with little actual clinical impact and for the larger cases only a negligible overall dose difference of >1% was seen. This fit with the work of (Matsuura et al 2016) who treated lung tumours with a mini ridge-filter. For the prostate cancer cases, no differences in the dose were observed. For the skull base chordoma cases, only very marginal differences in dose to selected OARs were observed for three out of four patients but for one case – a large tumour located next to the chiasma and the eye region – small increases in the overall integral dose of 5.8% to the brainstem and 7.2% for the spinal cord were detected.

RiFis of 3 mm thicknesses of the first and second generation design yield identical RiFi performances (table 2, **article 2**).

The irradiation time *T* was calculated to estimate the benefit of the thicker RiFis:

$$T = n_s \cdot t_{nS} + n_p \cdot t_{nP} \quad (2)$$

where n_S is the total number of IES, n_P the total number of beam spots, t_{nS} is the time for a synchrotron cycle with the extraction time subtracted and t_{nP} the time per scanned beam spot for a given energy slice n_S. Here *T* symbolizes the actual time of irradiation from the accelerator beam request for the first slice of a field up to the last beam spot of the last slice. The "off-beam" time periods, including movement of the treatment table, repositioning, eventually imaging and the preparation time were excluded, since these do not differ whether or not a passive beam modulating technique is applied. Values of n_S and n_P were extracted from TRiP98 raster files with n_S typically ranging from 10 to 100 and n_P being some thousands. We assumed for calculations of *T*, using as an example the setup for a fast intensity controlled continuous raster scanning system with a synchrotron, such as at HIT or MIT (Haberer et al 1993), a range of values of 4-6 s for t_{nS} and 3-8 ms for $t_{nP,}$ which are conservative compared to a reported 4.5 s between extractions (Schömers et al 2014).
Figure 6, **article 2** and figure B1 **article 2 suppl. material** show the sum over all fields of *T* for the investigated cases. The vertical bars in the figures were calculated using the estimated ranges for the times t_{nS} and t_{nP} (section 2.3 in **article 2**). The use of 4 and 6 mm RiFis lead to an overall reduction of the irradiation time of 26-30% and 45-49% respectively. It is not exactly 33% and 50% since either the first or the last energy slice at either the proximal or distal PTV edge remains unchanged for different energy step sizes.

2.5 Proton planning with the 6 mm ripple filter; preliminary results

In addition to plans with carbon ions, protons plans have been calculated in TRiP98 for no RiFi and the 2D 6 mm RiFi using the same patient cohorts although they have not yet been published. Selected results for four spherical PTVs for protons compared to the corresponding carbon ion plans originally shown in figure 2, **article 2**, are presented in Figure 1 for the sake of discussion. 2D 6 mm RiFis are compared to no RiFi for the proton plans and compared to 1D 3 mm RiFis for the carbon ion plans, being the two respective modalities for 3 and 6 mm energy step sizes. These initial results validate that the 2D 6 mm

RiFi can be used in proton treatment plans, which is supported by yet unpublished proton Bragg curve measurements for 2D RiFi samples (Weber et al, n.d., Ringbæk et al n.d.). It can furthermore be seen that the differences in CI and HI values for the RiFis as a function of PTV size and isocenter depth are more pronounced for protons than for carbon ions as a results of larger scattering effects. For small superficial PTVs requiring low beam energies, the RiFi might result in an unacceptable large lateral broadening of the beam.

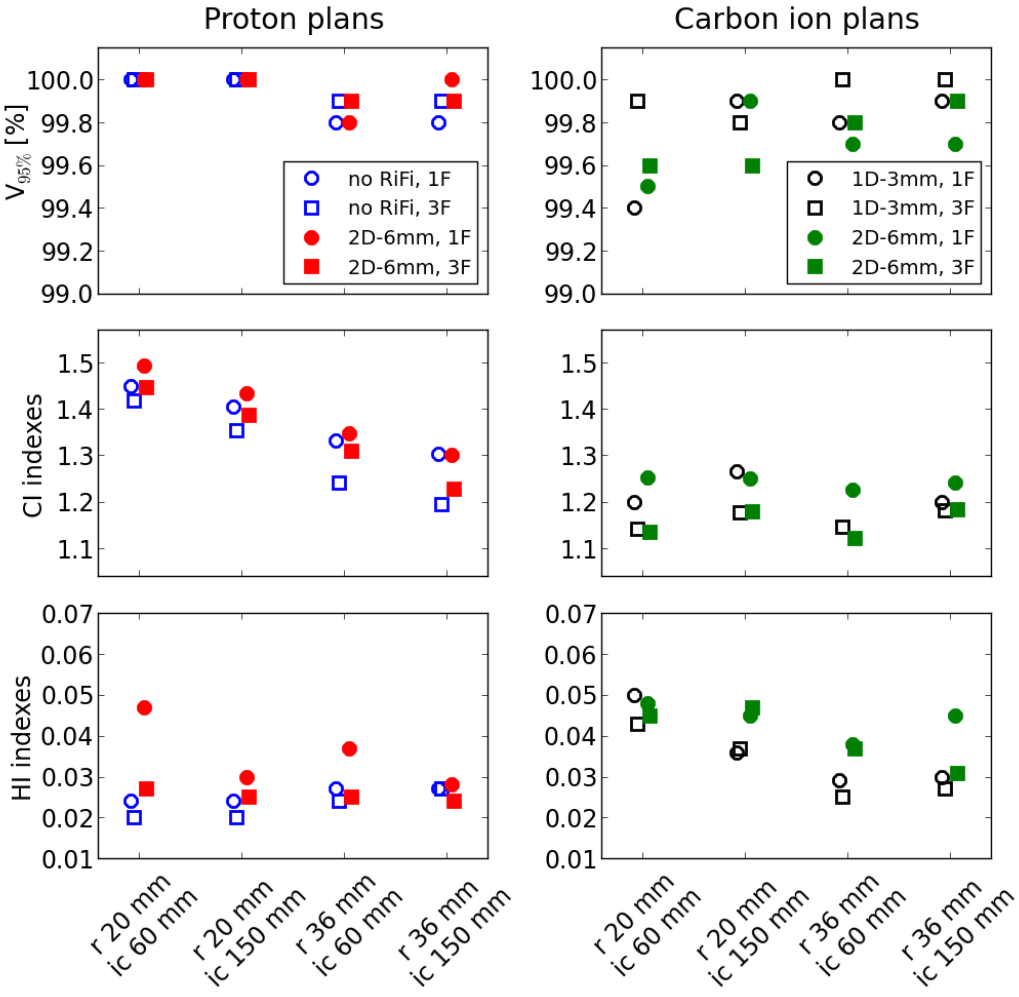

Figure 1: Dosimetric indexes for spherical PTVs in water phantoms with different radii *r* and isocenter depths *ic* for proton plans with and without a 2D 6 mm RiFi (left side) and carbon ion plans for a 1D 3 mm RiFi compared to a 2D 6 mm RiFi (right side). The term *F* in the legends indicates number of used field directions.

2.6 Modulation power of porous materials and potential usage as ripple filters

Since porous materials broadens the BP due to a larger straggling effect than what would be expected for non-porous materials (section 1.7 in this thesis), they represent another passive option for an ion beam modulation technique, similar to RiFis, to be used in PT facilities.

In order to describe the correlation between the physical parameters of porous materials and the strength of the corresponding beam modulation, a "binary voxel model" had been developed prior to this work, which is for the first time published in **article 3**. Readers are referred to the article (**section 2.1 and figure 1**) for a detailed description but the basic idea is that a porous plate is modelled by small cubic voxels with some voxels having a high density (probability *p*) and the remaining a very low density (1-*p*). Particles traveling through this inhomogeneous sample are subjected to a different energy loss and scattering effect depending on which row of voxels they go through, leading to a net range modulation that can be described by the probability density function of the sample in the form of a binominal distribution. The corresponding normal distribution with its Gaussian width σ can then be used to calculate the modulated Bragg curve by convolution with the pristine Bragg curve. The value of σ then gives the degree of enlargement for the BP width in correspondence with the work of (Titt et al. 2015).

From that we defined the "modulation power" P_{mod} (**article 3,** equation 5):

$$P_{mod} = \sigma^2 / t \tag{3}$$

where *t* is the mean water-equivalent thickness of the target in the beam direction. The values of σ and *t* can be found by fits to measured Bragg curves. The larger P_{mod} the larger the BP enlargement while for homogeneous (non-porous) targets $P_{mod} = 0$.

To validate the binary voxel model, the Bragg curves in a water phantom were scored with a porous as well as a non-porous block with the same composition and value of *t* (details in **article 3**). The Bragg curve of the solid block was convoluted with the correspondingly obtained normal distribution and compared with the MC curve. The result is shown in Figure 5, **article 3,** validating the binary voxel model.

To show the energy straggling effect of porous materials and to find values of P_{mod}, carbon-12 Bragg curve measurements were carried out at HIT using a water column (PTW PeakFinder T41030) and a range of porous materials with variable texture and thicknesses. Bragg curves were also measured for the build-in 1D 3 mm RiFi, for a range of probes of 2D 4 and 6 mm RiFis and for a partly-inflated ex vivo porcine lung. The measured curves

are shown in Figure 4, **article 3**. From these curves the modulation parameters such as P_{mod} of the respective materials could be determined as listed in table 1, **article 3**; details on calculations and uncertainties are given in section 2.3.1, **article 3**. Once the P_{mod} value of a given porous material is obtained, the BP enlargement for absorbers of any thickness can be predicted. As a matter of example, it was thus found that porous plates of 20 and 50 mm thick Gammex LN300 lung substitute material (Gammex 2004) would lead to a flat SOBP for energy steps of 3 and 6 mm, respectively; “flat” here defined as less than 1% dose inhomogeneity in SOBP plateau. Calculated unfiltered and filtered SOBPs in Figure 6, **article 3,** illustrate this. The unfiltered SOBPs are superpositions of a measured BP shifted in depth and the filtered SOBPs are calculated from the unfiltered ones with the obtained modulation parameters for LN300. The BP weights are the same for all SOBPs and optimized for the unfiltered ones.

The usage of porous targets as combined RiFis and range shifters were investigated with FLUKA MC simulations and a 50 mm thick LN300 plate, in analog to the investigations above. The general concept and the setup are shown in Figure 3, **article 3**: With the plate a higher proton energy can be chosen for the same penetration depth in water as compared to when no plate is included. The higher energy lowers the total scattering prior to the plate, which reduces the lateral width of the beam at a certain distance from the plate (Titt et al 2010). To show this, the lateral beam width (in FWHM) at the end of the particle range for setups using either a porous plate or no plate were scored. The FWHM values were obtained from Gaussian fits to dose distributions scored at the BP position in a water phantom in a plane perpendicular to the beam axis. The results can be seen in Figure 7, **article 3**, with three different initial beam energies for each setup. The ranges in water for the three beam energies for the setup without the plate matches the ranges in water for the three energies with the plate included. When comparing the beam widths at small distances from the plate it is seen how the lateral beam width is reduced for the plate setup compared to when using no plate and a lower energy. As a highlighted example, the net beam width reduction for a distance of 2 cm from the plate is 21.4% for a 3.1 cm penetration depth and 7.3% for a 6.2 cm penetration depth. For a 9.9 cm penetration depth there is only a very limited beam width reduction for distances of less than a few centimeter from the plate and instead for larger distances the beam widths increase. This could imply that using a porous plate is only beneficial in treatment cases with penetration depths smaller than ≈10 cm.

2.7 Lateral beam enlargement of passive energy modulators

The lateral beam widths for 120 MeV protons for a various number of RiFi designs and configurations as well as for no RiFi were obtained from Gaussian fits to 1D fluence profiles from experimental as well as simulated fluence distributions orthogonal to the beam axis. X-Omat V photometric films were used in the experiments and modelled in the simulations as the scoring volumes. Three sets of simulations were done with pencil beam widths at the RiFi plane $\sigma_x = \sigma_y$ of 1.0 mm, 1.2 mm and 1.4 mm, which as seen in **article 1** are realistic values when focusing the beam at the isocenter. For each of these, the beams were centred at the RiFi structure peak, the valley and in-between, respectively, and the corresponding datasets averaged for the final result in order to take into account the effect of hitting the RiFi structure at different places.

This work was carried out as part of the dissertation and will be published soon (Ringbæk et al n.d.) but is here simply summarized in Figure 2. Figure 2 shows for different RiFi configurations FWHM values for a simulated 120 MeV proton beam with σ_x =1.2 mm at various distances and FWHM values measured at the isocenter. The FWHM values are shown as a function of the distance in air from the beam nozzle after having passed the RiFi in question and the BAMS. Since all external RiFi probes were attached to a self-made wooden frame outside of the BAMS, the curves related to these start 80 mm after the nozzle. The plotted uncertainties are estimated from low, middle and high fluence spots in the calibration films. The investigated RiFi probes are listed in the figure legend and were manufactured by the 3D printing companies 3DS and BURMS and the Ernst-Abbe Hochschule (AUH), Jena, Germany (Weber et al 2015). Crossed configurations were also tested. When crossing two 1D RiFis a broader BP can be obtained than with one RiFi alone; two crossed 1D 3 mm RiFis make energy step sizes of 4 mm possible, similar to a 2D 4 mm RiFi. The groove structures of the two RiFis have to be placed orthogonal to each other, corresponding to the convolution of two linear transfer functions giving as a result a non-linear transfer function. It can be seen in Figure 2 that less than 200 mm from the RiFi, the difference between the RiFis are yet too small to be seen but as the beam widens with distance the difference increases. At the isocenter, where comparisons with measurements validate the simulations, FWHM differences in the measurements for the 1D 3 mm RiFi, the 2D 4 mm RiFi, the 2D 6 mm RiFi, the crossed 1D 3 mm RiFis and the crossed DeltaRiFis when compared to no RiFi are found to be 17(+/-2)%, 17(+/-1)%, 24(+/-2)%,

31(+/-1)% and 32(+/-1)%, respectively. From the MC data, a <0.5% difference in the lateral beam profiles where found when comparing pencil beams centred at the peak, the valley or in-between in agreement with Matsuura et al (2016) since the beam spot size at the RiFi plane is larger than some RiFi periods. For σ_x = 1.0 mm and σ_x = 1.4 mm the results differ only at distances of >200 mm from the RiFi with <3%.

Protons were chosen for investigation since their higher scattering power makes the difference between the various configurations more pronounced. However, since RiFis are normally used in heavy ion therapy, it would be more clinical relevant to look at these. It has been found previously by MC simulations that the difference in FWHM values for medium and high energetic carbon ions is, compared to no RiFi, 8(+/-1)% for a 2D 3.6 mm RiFi and 11(+/-1)% for a 2D 6 mm RiFi (Ringbæk et al 2014).

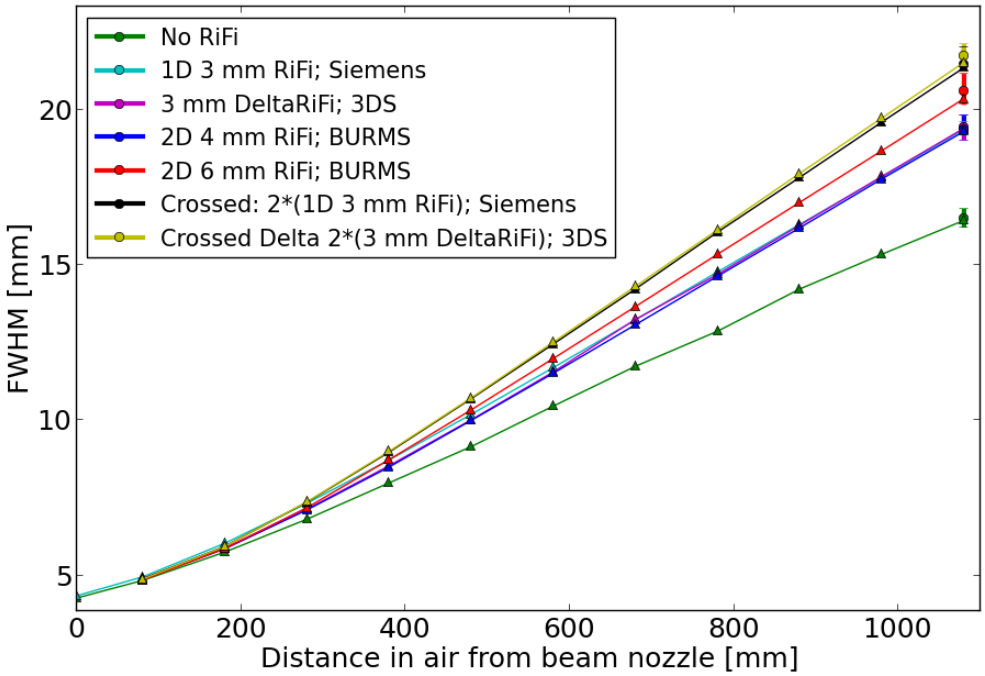

Figure 2: FWHM values for 120.05 MeV proton beams with σ_x = 1.2 mm at the RiFi plane passing through selected RiFi configurations as well as no RiFi. FWHM values are obtained from fits to fluence profiles from calibrated radiographic films at the isocenter (circles) as well as from fits to simulated fluence profiles at various distances *d* from the RiFi in question (triangles). The uncertainties of the measurements have been obtained by comparing results from low, middle and high fluence spots. “DeltaRiFi” is the triangular 1D RiFi of the CNAO design (Bourhaleb et al 2008). Some probes have been omitted to make the figure transparent.

3. Aim and Contribution

3.1 Aim of the Dissertation

It is known prior to this work that a RiFi with a 1D pin structure can be used as a passive energy modulator in scanned beam PT to enlarge the BP and reduce the number of energy shifts from the accelerator and thereby the irradiation time. A new RiFi design with a 2D pin structure has been developed using rapid prototyping, which optimizes the beam-modulating material and enables thicknesses of up to 6 mm.

The novel aim of this work is to first evaluate possible clinical disadvantages in the beam delivery caused by a RiFi of any design (**article 1**) and then to present a methodological presentation of treatment plans with the new thicker 2D RiFi design and investigate whether or not this design can reduce the irradiation time with an equivalent dosimetric performance as compared to the in-use 1D 3 mm RiFi (**article 2**). Additionally it was found that plates of porous materials with micro-structures could function as passive energy modulators in treatments too for replacement of RiFis while at the same time be used as range shifters (**article 3)**.

The work of this thesis presents and improvement of the general understanding of scattering effects of inhomogeneous objects like the RiFis and the porous materials. As a continuation it makes the usage of such devices safer by describing the Moirè-effect.

3.2 Contributions

Below is listed the contributions written by and seen from the viewpoint of the author of this dissertation. They include the three featured peer-reviewed publications as well as selected conference presentations relevant for the present study.

3.2.1 Publication 1:

Fluence inhomogeneities due to a ripple filter induced Moiré effect.

U. Weber had the idea for the study based on measured data obtained by S. Brons, J. Naumann, B. Ackermann, J. Horn, H. Latzel, S. Scheloske and M. Galonska and originally presented by J. Naumann. The study was then designed by U. Weber, K. Zink and me. Additional experimental data was obtained at HIT by U. Weber, S. Brons and me. The mathematical description of a (de)focused beam in phase-space originally formulated by U.

Weber was implemented in SHIELD-HIT12A by N. Bassler and tested by me. I performed all the simulations and did all the data analysis. I interpreted the data aided by U. Weber and K. Zink. I wrote the bulk of the paper with all authors contributing with comments and corrections. I made all figures apart from figure 1, which was provided by J. Naumann, and figure 2, which was made together with U. Weber.

3.2.2 Publication 2:

Dosimetric comparisons of carbon ion treatment plans for 1D and 2D ripple filters with variable thicknesses.

The study was conceived and designed by U. Weber, K. Zink and myself. A. Santiago and A. Wittig provided the CT data sets for the NSCLC patients, originally treated by P. Fritz and contoured for research-purposes by A. Wittig. M. Krämer provided CT data sets for the skull-base chordoma patients and the prostate patients. A. Santiago and Y. Simeonov provided technical advice related to the treatment planning procedure and the handling of the CT data sets. U. Weber compiled a slightly modified version of TRiP98 which was used for treatment planning. M. Krämer assisted with TRiP98 questions as well as providing access to said software on the GSI cluster. I performed all the MC simulations and scripting needed to generate the base data for the treatment planning based on work by N. Bassler with N. Bassler further aiding by debugging the MC code. I did all the benchmarking connected to the base data generation. I performed the treatment planning, the corresponding data analysis and the interpretation of the data. I wrote the bulk of the paper and did all figures with all authors contributing with comments and corrections, in particular U. Weber and K. Zink.

3.2.3 Publication 3:

Modulation power of porous materials and usage as ripple filter in particle therapy

The study was conceived and designed by U. Weber and K. Zink, partly based on findings presented originally in the master thesis of M. Witt. The binary voxel model, also used in that work, is developed by U. Weber. The experiments were conducted by U. Weber, M. Witt and myself with all of us performing various parts of the data analysis. Y. Simeonov did all the MC simulations in FLUKA. U. Weber and K. Zink assisted in the interpretation of the data and in restructuring the manuscript to make it acceptable for publication. I wrote

the bulk of the paper with all authors contributing with comments and corrections. Figures 3 to 8 were provided by U. Weber and finalized by me.

3.2.4 Conference presentations:

As part of the work of this dissertation, additional MC simulations have been performed by me and experimental data have been obtained and analyzed together with U. Weber. Some of these findings are going to be published in the upcoming year(s) in a manuscript by U. Weber describing the manufacturing aspect of the new RiFi design with me as co-author (Weber et al, n.d.) as well as in another manuscript by me describing proton therapy treatment planning with the new RiFis (Ringbæk et al, n.d.). Some of these results have already been presented by me at oral presentations or poster presentations at a number of conferences in 2014, 2015 and 2016. The citable of these oral presentations (but not the latest one) was being held at PTCOG53 in Shanghai (Ringbæk, Brons et al 2014). In the latest (non-citable) oral presentations at the DKFZ symposium *"Precision, Speed and Flexibility: New radiation detection methods for ion beam radiotherapy"* in Heidelberg, the results of the lateral scattering for RiFis, which are in this thesis included as Figure 2, was presented. In (non-citable) poster sessions in 2016, the initial results for the proton planning study with 2D RiFis — part of what is made into Figure 1 in this thesis — where presented for the first time. Additionally, work done by me in relation to this dissertation has been included in other conference presentations, such as by U. Weber (Weber et al 2015), where simulated Bragg curves for different RiFis as well as simulated planned dose distributions on simple PTVs done by me were shown.

In the version of the dissertation submitted for evaluation, the "Richtigkeit der gemachten Angaben bezüglich des Eigenanteiles von Toke Printz Ringbæk an den aufgeführten Publikationen und Beiträgen" was confirmed by signatures from the author as well as from both supervisors. These signatures have been omitted from this revised version.

4. Discussion

4.1 Benefits of the new ripple filter design

In **article 2** it was shown that in carbon ion treatment planning the new and thicker second generation RiFi design with two-dimensional pin structures yield similar results in terms of PTV coverage and dose homogeneity compared to the in-use first generation RiFi with one-dimensional pin structures for spherical PTVs in water and patients with early stage NSCLC, skull-base chordoma and prostate cancer. A slightly worse conformity around the PTV edge for thicker RiFis were observed, but this only influences treatments in specific situations where the PTV is superficial and located next to OARs or dose sensitive normal tissue. The new RiFis shorten irradiation times even more than the established one with an overall reduction of the irradiation time of 26-30% and 45-49% for the 2D 4 and 6 mm RiFis respectively, compared to a 1D 3 mm RiFi.

The new 2D design lowers the amount of lateral scattering compared to a 1D RiFi of the same thickness (section 2.7), leading to smaller beam spot sizes at the isocenter. The FWHM at the isocenter was found to be similar for the 1D 3 mm RiFi and the 2D 4 mm RiFi (Figure 2) and thus it is concluded that the removal of the base layer from the 1D to the 2D design makes it possible to add at least 1 additional millimeter of beam-modulating material, increasing the energy step size accordingly. Even though increasing the beam spot size can sometimes be clinically beneficial as an option for motion mitigation (Richter et al 2014) and can potentially lead to an overall increased robustness as well (Van de Water et al 2012), there is a general consensus that smaller beam spot sizes gives better OAR and normal tissue sparing (Lomax et al 2008) and in robust optimization methods a higher degree of freedom, e.g. smaller spot sizes, could give better results (Liu et al 2016). Therefore, typically the smallest possible beam spot size for the largest possible ripple effect is desired, which as shown in the present study is best obtained with the new 2D design.

By using a double filtering configuration with two crossed 1D RiFis, 4 mm energy step sizes are made possible in treatment planning, similar to when using a non-crossed 2D 4 mm RiFi. Additionally, such double filtering configurations can for RiFis with a cruder design, such as rough triangular shapes (Bourhaleb et al 2008), result in a satisfactory Gaussian smoothing of the BP that would otherwise not be achieved with such a RiFi.

However, the double filtering configuration introduces more non-modulating material in the beam path in the form of two times the base layer. As was seen when comparing the size of the lateral fluence profile, there is an 11-14% difference in FWHM values for a crossed RiFi setup compared to a 2D 4 mm RiFi. It is the opinion of the author that using a rougher shape or a double filtering configuration is in sense of minimized lateral scattering for maximum beam modulation effect less efficient than manufacturing a better suited RiFi, like of the 2D design.

It has been postulated that the usage of better optimized 2D RiFis is unnecessary when simpler RiFi designs can be used in non-isocentric treatments with very small distances from the RiFi to the target surface (Gevillot et al 2015). This however contradicts the findings in this work, where a certain distance from the RiFi of ~17 cm for protons and ~60 cm for carbon ions is needed to blur out the RiFi-induced fluence imhomogeneities. Non-isocentric treatments might also prove troublesome in daily QA routines in the clinic.

The (preliminary) findings presented in Figure 1 show that the new 2D 6 mm RiFi could be used in proton treatments too, as opposed to the 1D 3 mm RiFi. Other teams have looked into thicker 1D filters for proton treatments in the lung (Courneyea et al 2014, Matsuura et al 2016); the former with plans on phantoms with simulated base data for filter thicknesses up to 24.6 mm and the latter in actual treatments with only one filter. The shape of these filters is cruder than the 1D 3 mm RiFi (Weber et al 1999) and thicker filters are needed for the same energy step size, which make these designs not suited for treatments with heavier ions or for setups where the patient is not close to the nozzle. The design of Matsuura et al is interesting since it is in clinical use while the new 2D RiFi design is not yet applied for clinical treatments. It has a total thickness of 8 mm but only reduces the number of energy steps with around 50% as does the new 2D RiFi of 6 mm and it therefore seems to be a worse trade-off than the 2D design presented in this work, even though it is not directly shown how much the beam spot size is enlarged with and without the filter. Direct comparisons between beam spot sizes across facilities is not straight-forward due to differences in facility setup and nozzle-to-patient distances.

4.2 Porous plates in particle therapy treatments

Measurements and MC simulations show that porous plates can function as a RiFi and that, as a matter of example, a 20 mm LN300 plate of Gammex lung substitute material would lead to a flat SOBP similar to that of the 1D 3 mm RiFi while a 50 mm LN300 plate would match the results achieved with the 2D 6 mm RiFi for the corresponding energy step sizes. Although it is tempting to then choose the much cheaper and simpler porous plate to be used instead of a RiFi, care must be taken. The RiFi shape (of any design) is optimized to produce a maximum filter effect on the dose ripple with the minimum possible mass while a porous plate is not and therefore much more material is required to obtain the same filter effect for a porous plate than for a RiFi. The 20 mm LN300 plate might yield the same filter effect as a 3 mm RiFi but it has a mass thickness of 0.57 g/cm^2 compared to 0.2 g/cm^2 of the RiFi (table 1, **article 3**). Therefore, if the LN300 plate is installed at the same place as the RiFi – at the end of the BAMS – a flat SOBP would indeed be obtained for the same number of energy steps but with much larger beam spots. In contrast to RiFis however, porous plates can be positioned directly in front of the patient without inducing neither a fluence nor a dose range inhomogeneity. Thus either a RiFi should be installed at the nozzle or a porous plate placed close to the patient instead.

As was also shown in **article 3**, porous plates have potentially an additional clinical benefit when placed very close to the patient since they can act like a range shifter and decrease the lateral beam width. This effect is of particular interest for proton beam therapy, where the protons' physical nature leads to a larger scattering effect. Even though thicker RiFis seem to be applicable in proton therapy, for superficially located tumours where low beam energies are required, the insertion of such RiFis might results in unacceptably large beam spot sizes. In such treatments it might be better to opt for a porous plate, which as a combined RiFi and range shifter would simultaneously reduce the irradiation time and increase the sharpness of the beam. It is this duality that makes the porous plates lucrative. If one solely desires the range shifter effect, a solid plate with a smaller mass thickness as shown by Titt et al (2010) would be a better choice.

The binary voxel model used to describe the straggling effects of porous materials was found in **article 3** to be in very good agreement with reality for simpler porous structures. For macroscopic structures, such as present in RiFis, it cannot be directly used and obtained

values can only be used for comparison. The model also has shortcomings for more complex biological structures, like for example real lung tissue, where a normal distributed modulation is achieved only for the pathways through the lung where no macroscopic structures like larger blood vessels or the respiratory tract are present (Witt 2014). While an important topic in its own right, the modulation effect of the lung is not a part of this work and therefore these shortcomings will not be further addressed.

4.3 Clinical implementation of passive beam modulating techniques

This work shows the beneficial usage of passive energy modulators like a RiFi or a porous plate in active scanning PT treatments of tumours in the lung, prostate and brainstem. However, the implementation of passive energy modulators could potentially benefit treatments of all tumour types in such PT facilities, which is roughly half of all centers operating worldwide (PTCOG 2016). Of these, around 30 are using protons exclusively, one is using carbon ions and five have the option to choose between both.

One-third of the proton facilities and all of the heavy ion facilities are using synchrotrons. Although for protons the time for an accelerator energy shift is shorter than for heavier ions due to the lower required beam energy (at MIT it is around 3.5 s for protons compared to around 5 s for carbon ions), the time gain of an implemented RiFi would be of the magnitude presented in this work. For all of the heavy ion facilities, the 1D RiFi is already used and the implementation of the new design should therefore be straight-forward. When treatment modalities can be changed between carbon ions and protons, the new design adds the further advantage that it might be beneficial in proton treatments as well and could thus be used in both modalities. This is in opposition to most other new thicker designs, which as described previously is only optimized for proton treatments.

The remaining two-thirds of the proton facilities are using cyclotrons, where the gain in treatment time when using RiFis is presumably less, since cyclotrons already have passive degraders in the beam path and can potentially change energies much faster than synchrotrons. At the PSI an energy shift can be done as fast as ~80 ms for energy steps of 3 MeV (Safai et al 2012), even though normally it takes around 1 s (Zenklusen et al 2010). For a generic proton facility with a cyclotron however, the time for an energy shift can be up to 2 s (in conversation with U. Weber). When the time span for energy step changes is in seconds, the time reduction of a RiFi would still be clinically beneficial for cyclotron

facilities, although somewhat smaller in magnitude than when using synchrotrons.

Where cyclotrons compared to synchrotrons have a lower cost and a more stable and intense beam current, they also have larger beam-losses and a higher degree of material activation. As of now, treatments for particles heavier than protons are not feasible using cyclotrons mainly due to relativistic issues. Additionally, the beam degradation in cyclotrons for heavier ions would induce fragments (Schardt et al 2010), but systems with filters can be designed to obtain a purer fragmentless beam (Jorgen et al 2013). In the future, heavy ion PT using modern superconducting multi-ion cyclotrons treatments might be made possible (Jorgen et al 2010, Jorgen et al 2013).

The porous plates are mostly suitable for proton therapy centers where their dual range shifter and RiFi modality can be fully used. Of the 29 PT centers under construction, 26 are proton facilities with most opting for the scanned beam technique (PTCOG 2016).

To implement any new type of equipment in a PT treatment facility requires a number of validation and commissioning steps including measurements. Since the 2D 4 mm RiFi is not much thicker than the 1D 3 mm RiFi and yield similar beam spot sizes, this new RiFi should be easily implemented in facilities already using the 1D 3 mm RiFi. Any commercial TPS is thought to be able to handle the newer thicker RiFis, even though some minor changes might be required. In **article 2** a small dependency for the lateral contour extension and a strong dependency for the longitudinal contour extension on the conformity was found for all RiFis and for the thickest in particular. It was therefore concluded that a longitudinal virtual contour extension should be implemented in a TPS handling RiFis thicker than 3 mm.

The dose spike effect of larger energy step sizes might not be in reality so visible as is shown in figure 1, **article 2.** They have not been directly observed for any actual patient treatment plan but only in the cases of “simulated” spherical PTVs in water phantoms. The visibility of the effect could partly be due to the rough division of CT layers for simulated CTs in TRiP98 (in private conversation with S. Hild). No matter the case, the planning studies of this work clearly show that the thicker the RiFis the worse the planning conformity, which is still attributed in turn to the dose spike effect.

4.4 Moving targets and shorter irradiation times

The early stage NSCLC patients of the planning study in **article 2** were originally treated under HFJV, which means that the PTVs could be assumed to be stationary for planning (Santiago et al 2013, 2015). In general, breath-hold methods (Hanley et al 1999) are deemed more and more useful in PT treatments (Boda-Heggemann et al 2016). The effect of mini-ridge filters on breath-hold treatment of lung tumours has previously been studied with MC simulations (Courneyea et al. 2014), showing it to be a viable option for motion mitigation in such tumour cases. For patients under breath-hold, in particular under apnea (such as but not limited to under HFJV), a shorter irradiation time is still preferable in terms of patient comfort or for patients with limited lung capacities even though it would in such situations not lower the negative effects on the dose distribution caused by target motions since no motion is present.

In treatments were tumour motion cannot be ignored, a reduced irradiation time would not only counteract problems such as the interplay effect but would also make treatments with the more time-demanding motion mitigation techniques rescanning (Phillips et al 1992), gating (Ohare et al 1989, Furukawa et al 2007) or a combination of the two possible within an acceptable treatment time (Furukawa et al 2010). Currently single-field irradiation of liver tumours at HIT takes more than 30 minutes with gating opposed to 10 minutes without (Presentation by O. Jäkel, GSI september 2016). To establish how beneficial the thicker RiFis would be in such cases, treatment plans with intra-fractionally moving targets and the new RiFis are required. Such studies demand a treatment planning system capable of handling moving targets with as minimum the inclusion of 4D CT data sets and was outside the scope of this work. A version of TRiP98 exists, which can handle 4D CT data, 4D planning and even 4D dose optimization (Graeff et al 2013, Graeff 2014). Since this software uses as input the same base data files as generated for the normal TRiP98 version, repeating the planning study in **article 2** with moving targets should be straight-forward.

4.5 Additional methods for irradiation time reduction

Recently, a method to reduce the energy step sizes without the use of passive energy modulators is emerging. IES numbers can also be reduced in the optimization phase of the treatment planning if the TPS is accordingly programmed (van de Water et al 2015). First a normal plan with a constant equal energy step and no special optimization is made and this

plan is then used to re-optimize, aiming at minimizing the beam spots per energy layer. By then removing the energy layers with very few beam spots and compensate with the other pencil beams to make the plan acceptable, which can only be done for IMPT, the irradiation times can be reduces with 28% for prostate cancer cases (as a selected example). This is similar to the time reduction found in the present work when moving from a 1D 3 mm RiFi to a 2D 4 mm RiFi. This special optimization method is insofar only for proton planning due to their larger beam spots and BPs. In the future, a combination of thicker 2D RiFis and energy step size optimization algorithms could potentially reduce the irradiation times even more and such RiFis might yield sufficiently large BPs to use these algorithms also in treatments with heavier ions.

Currently a synchrotron cycle can provide only one specific energy, leading to the t_{nS} period of some seconds where the particles are dumped, injected and accelerated. However, the number of particles that are typically accelerated in one such cycle exceeds the number of required particles for one individual IES. A new synchrotron modality is currently investigated where remaining particles are re-accelerated or decelerated after the first extraction phase (Schömers et al 2014, Iwata et al 2010). In this scenario, multiple numbers of IES can be irradiated within the same cycle, which in turn can severely reduce the irradiation time, with an estimated 50-60% reduction. When such a synchrotron modality is used, the benefits from a RiFi would be reduced but still some benefits from RiFis would be achieved with the time reduction factor presented in this work remaining.

4.6 Outlook

Before the new RiFi design can be deemed fully beneficial in treatments with protons, planning with a commercial TPS dedicated to proton treatments is necessary to support the findings from TRiP98. We have access to the TPS Proton Eclipse and scripts have been written to turn simulated output from SHIELD-HIT12A into Eclipse input files. While proton treatment plans were not calculated prior to the submission of this dissertation, in the time between submission and the disputiation plans have been made for the NSCLC cases presented in this work. Due to the larger scattering effects of the lighter proton projectiles and because a 2D 6 mm RiFi is compared to a setup without any RiFi, the difference in conformity between the two modalities were found to be in general larger than for the carbon ion plans (Ringbæk et al, n.d.).

The robustness of plans with a larger energy step size should also be addressed. It would have to be investigated if for some patient cases a smaller energy step size than the one equal to the RiFi thickness should be opted for to make the plans more robust.

The dose inhomogeneity that can be observed at the skin when using a RiFi at an insufficient RiFi-to-target distance would also benefit from further investigations. Due to "the prompt microscopic biological repair effect" (Dilmanian et al 2015, Girst et al 2015) and "the dose-volume effect" (Withers et al 1998), faster biological repair of an area exposed with an inhomogeneous fluence field yielding spots of under- and over-dosage can be expected via the regeneration of cells in the high-dose spots from surviving cells in low-dose spots. Therefore the RiFi-induced fluence inhomogeneity effect might not be strictly a clinical disadvantage, besides initial patient discomfort.

Lastly, when opting for a passive energy beam modulator, like the RiFi or a porous plate, the optimal clinical settings have to be established for common tumour types, including establishment of treatment protocols. It has to be defined which cases in particular will benefit from the technical improvements in regard to beam modulation by a RiFi (or a porous plate) and how these clinical benefits can be reached. An investigation in regard to the beam spot grid size and energy step size for specific ion types and tumour types should then also be included. For this to be possible, the 2D RiFi design needs to be available for clinics, which is thought to be the case in a few years from now.

A new three-dimensional energy modulator has been designed in our group (Simeonov et al 2016, Simeonov et al 2017) based on the concept of the 2D RiFis and "stacked" 3D ridge filters (Sakae et al 2000). While this work is still in an early phase, experimental data supports that a spherical dose distribution can be obtained with one initial beam energy using this passive energy modulator, which might make it possible in the future to irradiate a small target in a matter of seconds. It should here be noted that these PTVs are the exact ones that cause the thick 2D RiFis the most problems in terms of conformity and maybe a combination of the two new filters could be used, with the best option chosen from treatment to treatment.

If small 3D printing manufacturing machines were in the future to be available to clinics on a daily basis, RiFis of 2D and 3D designs could be optimized and printed on the spot after clinical demand, combining passive and active beam delivery techniques and opening up for more patient-specific treatments.

5. References

Ahlen, S. P (1980). Theoretical and experimental aspects of the energy loss of relativistic heavily ionizing particles. *Rev. Mod. Phys.* 52:121–173.

Agosteo, S., C. Birattari, M. Caravaggio, M. Silari, and G. Tosi (1998). Secondary neutron and photon dose in proton therapy. *Radiother. Oncol.* 48:293–305.

Agostinelli, S., Allison, J., Amako, K., Apostolakis, J., Araujo, H. and Arce, P. et al (2003). Geant4 - a simulation toolkit. *Nucl. Instrum. Methods Phys. Res. A.* 506(3):250–303.

Allison, J., Amako, K., Apostolakis, J., Araujo, H., Dubois, P. A., and Asai, M. et al (2006). Geant4 developments and applications. *IEEE Transactions on Nuclear Science.* 53(1):270–278.

Bassler, N., Hansen, D. C., Lühr, A., Thomsen, B., Petersen, J. P. & Sobolevsky, N. (2014). SHIELD-HIT12A - a Monte Carlo particle transport program for ion therapy research. *Journal of Physics: Conference Series* 489(1).

Bassler, N., Jäkel, O., Soendergaard, C. S. & Petersen, J. B. (2010). Dose- and let- painting with particle therapy. *Acta Oncol. 49:*1170-1176.

Bassler, N., Hansen, J. W., Palmans, H., Holzscheiter, M. H., and Kovacevic, S (2008). The antiproton depth-dose curve measured with alanine detectors. *Nucl. Instrum. Methods Phys. B.*, 266:929–936.

Bassler, N., Kantemiris, I., Engelke, J., Holzscheiter, M. and Petersen, J. B (2010). Comparison of optimized single and multifield irradiation plans of antiproton, proton and carbon ion beams. *Radiother. Oncol.* 95:87–93.

Baumann, K. (2015). *Master Thesis:* Modellierung der patientennahen Strahlführung einer

Partikeltherapieanlage mit Hilfe des Monte-Carlo-Codes FLUKA unter exakter Berücksichtigung modulierender Elemente . *Technische Hochschule Mittelhessen (University of Applied Sciences).*

Baumann, M., Krause, M., Overgaard, J., Debus, J., Bentzen, S., Daartz, J., Richter, C., Zips, D. and Bortfield, T (2016). Radiation oncology in the era of precision medicine. *Nature Reviews Cancer* 16:234-249.

Bethe, H. A (1930). Zur Theorie des durchgangs schneller Korpuskularstrahlen durch Materie. *Ann. Phys.* 5.

Bethe, H. A (1953). Moliére's theory of multiple scattering. *Rev. Mod. Phys.* 89:1256–1266.

Bert, C. & Durante, M. (2011). Motion in radiotherapy: particle therapy. *Phys. Med. Biol.* 56, R113-R144.

Bert, C., Grözinger, S. O. & Rietzel, E. (2008). Quantification of interplay effects on scanned particle beams and moving targets. *Phys. Med. Biol.* 53.

Boda-Heggemann J, Knopf AC, Simeonova-Chergou A, Wertz H, Stieler F, Jahnke A, Jahnke L, Fleckenstein J, Vogel L, Arns A, Blessing M, Wenz F, Lohr F (2016). Deep inspiration breath hold-based radiation therapy: A clinical review. *Int J Radiat Oncol Biol Phys.* 94:478–92.

Bohr, N (1915). The penetration of atomic particles through matter. *Radiother. Oncol.* 30:581.

Bourhaleb F., Attili A., Cirio R., Cirrone P., Marchetto F. and Donetti M. et al (2008). Monte Carlo simulations of ripple filters designed for proton and carbon ion beams in hadrontherapy with active scanning technique. *J Phys Conf Ser* 2.

Böhlen, T. T., Cerutti, F., Chin, M. P. W., Fasso, A. amd Ferrari, A., Ortega, P. G., Mairani,

REFERENCES

A., Sala, P. R., Smirnov, G. & Vlachoudis, V. (2014). The Fluka code: Developments and challenges for high energy and medical applications. *Nuclear Data Sheets.*

Bragg, W. (1905). On the a-particles of radium and their loss of range in passing through various atoms and molecules. *Philos. Mag.* 10:318–340.

Castro J., Saunders W. and Tobias C (1982). Treatment of cancer with heavy charged particles. *Int J Radiat Oncol* 8:2191–8.

Courneyea, L., Beltran, C., Tseung, H. S. W. C., Yu, J. & Herman, M. G. (2014). Optimizing mini-ridge filter thickness to reduce proton treatment times in a spot-scanning synchrotron system. *Med. Phys.* 41.

Chu, W. T., B. A. Ludewigt, and T. R. Renner (1993). Instrumentation for treatment of cancer using proton and light-ion beams. *Rev. Sci. Instrum.* 64:2055–2122.

Dementyev, A. V. and Sobolevsky, N. M (1999). SHIELD - universal Monte Carlo hadron transport code: scope and applications. *Radiat. Meas.* 30:553–557.

Dilmanian, F. A., Eley, J. G. and Krishnan, S. (2015). Minibeam therapy with protons and light ions: Physical feasibility and the potential to reduce radiation side effects and to facilitate hypofractionation . *Int J Radiat Oncol Biol Phys.* 1;92(2): 469–474.

Enghardt W., Debus J., Haberer T., Hasch B.G., Hinz R., Jäkel O. et al (1999). The application of PET to quality assurance of heavy-ion tumor therapy. *Strahlenther Onkol.* 175, Suppl 2:33–6.

Eyges, I. (1948). Multiple scattering with energy loss. *Phys. Rev. Lett.* 74(1-4):1534-1535.

Fassò, A.; Ferrari, A.; Ranft, J., and Sala, P. R (2005). FLUKA: a multi-particle transport code. *CERN-2005-10,* 49:1933–1958.

REFERENCES

Furukawa T., Inaniwa T., Sato S., Tomitani T., Minohara S., Noda K. and Kanai T. (2007). Design study of a raster scanning system for moving target irradiation in heavy-ion radiotherapy. *Med. Phys.* 34:1085–1097 .

Furukawa T., Inaniwa T., Sato S., Shirai T., Takei Y., Takeshita E. et al (2010). Performance of the NIRS fast scanning system for heavy-ion radiotherapy. *Med Phys.* 37:5672–82.

Gammex (2004). Tissue Characterization Phantom Model 467: User Guide.

Graeff, C., Lüchtenborg, R., Eley, J.R., Durante, M. and Bert, C. (2013). A 4D-optimization concept for scanned ion beam therapy . *Radiotherapy and Oncology.* 109:419-424

Graeff, C (2014). Motion mitigation in scanned ion beam therapy through 4D-optimization. Physica Medica. 30:570-577.

Gevillot, L., Stock, M. & Vatnitsky, S. (2015). Evaluation of beam delivery and ripple filter design for non-isocentric proton and carbon ion therapy. *Phys. Med. Biol.* 60:7985-8005.

Goitein, M (1983). Beam scanning for heavy charged particle radiotherapy *Med. Phys.* 10:831–840 .

Gottschalk, B. (2006). Neutron dose in scattered and scanned proton beams: In regard to Eric J. Hall. *Int J Radiat Oncol Biol Phys* 65:1-7.

Girst, S., Marx, C., Brauer-Krisch, E., Bravin, A., Bartzsch, S., Oelfke, U., Greubel, C., Reindl, J., Siebenwirth, C., Zlobinskaya, O., Multhoff, G., Dollinger, G., Schmid, T.E. and Wilkens, J.J. (2015). Improved normal tissue protection by proton and X-ray microchannels compared to homogeneous field irradiation . *Physica Medica.* 31: 615-620.

Haberer, T., Becher, W., Schardt, D. & Kraft, G. (1993). Magnetic scanning system for heavy ion therapy. *Nucl. Instr. and Meth.* A330, 296.

REFERENCES

Hanley J., Debois, M.M. Mah, D., Mageras, G.S., Raben, A., Rosenzweig, K. Mychalczak, B., Schwartz, L.H., Gloeggler, P.J., Lutz, W., Ling C.C. Leibel, S.A. Fuks, Z. and Kutcher G.J. (1999). Deep inspiration breath-hold technique for lung tumors: the potential value of target immobilization and reduced lung density in dose escalation. *Int. J. Rad. Oncol. Biol. Phys.* 45:603–11

Hansen, D. C., Lühr, A., Herrman, R., Sobolevsky, N. M. and Bassler, N (2012a). Recent improvements in the SHIELD-HIT code. *Int. J. Radiat. Biol.* 88:195–199.

Hansen, D. C., Lühr, A., Sobolevsky, N. M. and Bassler, N (2012b). Optimizing SHIELD-HIT for carbon ion treatment. *Phys. Med. Biol.* 57:2393–2409.

Highland, V. L (1975). Some practical remarks on multiple scattering. *Nucl. Instrum. Methods* 129.

Highland, V. L (1979). Erratum. *Nucl. Instrum. Methods,* 161.

History of Stereolithography (2011). Book published by Springer.

Hollmark, M., Uhrdin, J., Belkic, D., Gudowska, I. & Brahme, A. (2004). Influence of multiple scattering and energy loss straggling on the absorbed dose distributions of therapeutic light ion beams: I. analytical pencil beam model. *Phys. Med. Biol.* 49:3247–3265.

IAEA (2008). Relative biological effectiveness in ion beam therapy, *Technical reports series no. 461,* Technical Report 46 (Vienna: International Atomic Energy Agency)

Iancu, G., Krämer, M., Zink, K., Durante, M. and Weber, U. (2015). Implementation of an efficient Monte Carlo algorithm in TRiP: Physical Dose Calculation. *International journal of particle therapy* 2(2):415-425.

REFERENCES

Iwata, Y., Furukawa, T., Mizushima, K., Noda, K., Shirai, T., Takeshita,E. and Takada, E (2010). Multiple-energy operation with quasi-DC extension of FLATTOPS at HIMAC. *Proceedings of IPAC10, Kyoto, MOPEA008.*

Jelen, U., Bubula, M.E., Ammazzalors, F., Engenhart-Cabillic, R., Weber, U. and Witting, A (2013). Dosimetric impact of reduzed nozzle-to-isocenter distance in intensity-modulated proton therapy of intracranial tumors in combined proton-carbon fixed-nozzle treatment facilities. *Radiat. Oncol.* 8: 218.

Jia, X., Schümann, J., Paganetti, H. and Jiang, S.B (2012). GPU-based fast Monte Carlo dose calculation for proton therapy. Phys Med Biol. 7;57(23)7783-7797.

Jongen, Y., Abs, M., Blondin, A., Kleeven, W., Zaremba, S., Vandeplassche, D., Aleksandrov, V., Gursky, S., Karamyshev, O., Karamysheva, G., Kazarinov, N., Kostromin, S., Morozov, N., Samsonov, E., Shirkov, G., Shevtsov, V., Syresin, E. and Tuzikov, A. (2010). Compact superconducting cyclotron C400 for hadron therapy . Nuclear Instruments and Methods in Physics Research A 624:47–53 .

Jongen, Y., et al (2013). Cyclotrons from protons to Carbon for Hadron Therapy [PowerPoint Slides]. PAC2013 at Pasadena.
Retrieved from : http://accelconf.web.cern.ch/AccelConf/pac2013/talks/thybb1_talk.pdf

Kanai, T., Kawachi, K., Kumamoto, Y., Ogawa, H., Yamada, T., Matsuzawa, H. and Inada, T (1980). Spot scanning system for proton radiotherapy. *Med Phys.* 7;365

Kraft, G. (2000). Tumor therapy with heavy charged particles. *Prog. Part. Nucl. Phys*. 45:473-544.

Krämer, M., Jäkel, O., Haberer, T., Kraft, G., Schardt, D. & Weber, U. (2000). Treatment planning for heavy-ion radiotherapy: physical beam model and dose optimization. *Phys. Med. Biol.* 45:3299-3317.

REFERENCES

Krämer, M. & Scholz, M. (2000). Treatment planning for heavy-ion radiotherapy: calculation and optimization of biologically effective dose. *Phys. Med. Biol.* 45:3319-3330.

Krämer, M. & Durante, M. (2010). Ion beam transport calculations and treatment plans in particle therapy. *Eur. Phys. J. D.* 60:195-202.

Lindhard, J. and Scharff, M (1961). Energy dissipation by ions in the keV region. *Phys. Rev.* 124: 128–1301.

Loeffler J.S. and Durante M (2013). Charged particle therapy-optimization, challenges and future directions. *Nat Rev Clin Oncol* 10:411–24.

Lomax, A. J., Bortfeld, T., Goitein, G., Debus, J., Dykstra, C. and Tercier, P. A (1999). A treatment
planning inter-comparison of proton and intensity modulated photon radiotherapy. *Radiother. Oncol.* 51:257–271.

Lomax, A. J., Böhringer, T., Bolsi, A., Coray, D., Emert, F., Goitein, G., Jermann, M., Lin, S., Pedroni, E., Rutz, H., Stadelmann, O., Timmermann, B., Verwey, J. and Weber, D. C (2004). Treatment planning and verification of proton therapy using spot scanning: Initial experiences. *Med Phys.* 31:3150.

Lomax, A.J (2008). Intensity modulated proton therapy and its sensitivity to treatment uncertainties 1: The potential effects of calculational uncertainties. *Phys Med Biol* 53:1027–1042.

Liu, W., Schild, S., Chang, J., Liao, Z., Ding, X., Hu, Y., Shen, J., Korte, S., Sahoo, N., Wong, W., Herman, M. and Bues, M. (2016). TH-CD-209-05: Impact of Spot Size and Spacing On the Quality of Robustly-Optimized Intensity-Modulated Proton Therapy Plans for Lung Cancer. Med. Phys. 43:3886.

REFERENCES

Lui, W., Zhang, X., Li, Y. and Mohan, R (2012). Robust optimization of intensity modulated proton therapy. *Med Phys.* 39(2):1079-91.

Lühr, A., Hansen, D. C., Jäkel, O., Sobolevsky, N. and Bassler, N (2011a). Analytical expressions for water-to-air stopping-power ratios relevant for accurate dosimetry in particle therapy. *Phys. Med. Biol.* 56:2515–2533.

Lühr, A., Toftegaard, J., Kantemiris, I., Hansen, D. C. and Bassler, N (2012). Stopping power for particle therapy: the generic library libdEdx and clinically relevant stopping-power ratios for light ions. *Int. J. Radiat. Biol.* 88:209–212.

Ma, N. Y., Tinganelli, W., Maier, A., Durante, M. & Kraft-Weyrather, W (2013). Influence of chronic hypoxia and radiation quality on cell survival. *J. Radiat. Res.* 54(Suppl. 1):i13–i22.

Mason, D. (2011), Su-e-t-33: Pydicom: An open source dicom library. *Med Phys.* 38:3493.

Matsuura, T., Fujii, Y., Takao, S., Yamada, T., Matsuzaki, Y., Miyamoto, N., Takayanagi, T., Fujitaka, S., Shimizu, S., Shirato, H. & Umegaki, K. (2016). Development and evaluation of a short-range applicator for treating superficial moving tumors with respiratory-gated spot-scanning proton therapy using real-time image guidance. *Phys. Med. Biol.* 61.

McGowan, S.E., Albertini, F., Thomas, S.J. and Lomax, A.J. (2015). Defining robustness protocols: a method to include and evaluate robustness in clinical plans. *Phys. Med. Biol.* 60: 2671–2684

Metropolis, N. and Ulam, S (1949). The Monte Carlo method. *Journal of the American Statistical Association* 44:335–341.

Moliére, G (1948). Theorie der Streuung schneller geladener Teilchen ii. Mehrfach- und Vielfachstreuung. *Z. Naturforsch.* 3a:78.

REFERENCES

Nikoghosyan, A., Schulz-Ertner, D., Herfarth, K., Didinger, B., Münter, M. W., Jensen, A., Jäkel, O., Hoess, A., Haberer, T. & Debus, J. (2011). Acute toxicity of combined photon imrt and carbon ion boost for intermediate-risk prostate cancer - acute toxicity of 12c for pc. *Acta Oncol.* 50:784-790.

Nill, S., T. Bortfeld, and U. Oelfke (2004). Inverse planning of intensity modulated proton therapy. *Z. Med. Phys.* 14:35-40.

Ohara K., Okumura T., Akisada M., Inada T., Mori T., Yokota H. and Calaguas M.J. (1989). Irradiation synchronized with respiration gate. *Int. J. Rad. Oncol. Biol. Phys.* 17:853–7

Parodi, K., Mairani, A. and Sommerer, F (2013). Monte Carlo-based parametrization of the lateral dose spread for clinical treatment planning of scanned proton and carbon ion beams. *Journal of Radiation Research* 54;i91-i96

Particle Therapy Co-Operative Group (2016), Anual Patient and Facility Statistics at http://www.ptcog.ch. Accessed October 2016.

Pedroni, E., Meer, D., Bula, C., Safai, S. and Zenklusen, S (2011). Pencil beam characteristics of the next-generation proton scanning gantry of PSI: design issues and initial commissioning results. *Eur. Phys. J. Plus* 126:66.

Phillips M.H., Pedroni E., Blattman H., Böhringer T., Coray A. and Scheib S (1992). Effects of respiratory motion on dose uniformity with a charged particle scanning method. Med. Phys. Biol. 37:223–34.

Richter, D., Graeff, C., Jäkel, O. and Bert, C (2014). Residual motion mitigation in scanned carbon ion beam therapy of liver tumors using enlarged pencil beam overlap. Radiotherapy and Oncology 113(2).

REFERENCES

Ringbæk, T.P., Brons, S., Naumann, J., Ackermann, B., Thomsen, B., Bassler, N., Zink, K. and Weber, U. (2014). 059: Evaluation of New 2D Ripple Filters for Particle Therapy Facilities. *International Journal of Particle Therapy,* 1(2):472-473.

Ringbæk, T.P., Weber, U., Bassler, N. and Zink, K (2014). Evaluation of New 2D Ripple Filters for Particle Therapy Facilities [PowerPoint Slides]. *PTCOG 53 Shanghai*.
Retrieved from:
http://ptcog.ch/archive/conference_p&t&v/PTCOG53/PresentationsSM/59_Ringbaek.pdf

Ringbæk, T. P., Weber, U., Thomsen, B., Petersen, J. B. B. & Bassler, N. (2014). Monte carlo simulations of new 2d ripple filters for particle therapy facilities. *Acta Oncol.* 53:40-49.

Ringbæk, T. P., Weber, U., Santiago, A., Simeonov, Y., Iancu, G., Wittig, A., Grzanka, L., Bassler, N., Engenhart-Cabillic, R. and Zink, K. (*yet unpublished!*). Validation of new 2D ripple filters in proton treatments of spherical geometries and non-small celled lung carcinomas. *Will be submitted to PMB in 2018.*

Safai, S., Bula, C., Meer, D. and Pedroni, E. (2012). Review Article: Improving the precision and performance of proton pencil beam scanning. *Translational Cancer Research.* 1(3).

Sakae, T., Nohtomi, A., Maruhashi, A., Sato, M., Toshiyuki, T., Kohno, R., Akine, Y. Aoba-ku, C. and Koike, Y (2000). Multi-layer energy filter for realizing conformal irradiation in charged particle therapy . *Med. Phys.* 27:2.

Santiago, A., Jelen, U., Ammazzalorso, F., Engenhart-Cabilic, R., Fritz, P., Mühlnickel, W. & Wittig, A. (2013). Reproducibility of target coverage in stereotactic spot scanning proton lung irradiation under high frequency jet ventilation. *Radiother. Oncol.* 109:45-50.

Santiago, A., Fritz, P., Mühlnickel, W., Engenhart-Cabilic, R. & Wittig, A. (2015). Changes in the radiological depth correlate with dosimetric deterioration in particle therapy for stage 1 NSCLC patients under high frequency jet ventilation. *Acta Oncol.* 54(9):1631-7.

Sawakuchi, G. O., Titt, U., Mirkovic, D. & Mohan, R. (2008). Density heterogeneities and the influence of multiple coulomb and nuclear scatterings on the Bragg-peak distal edge of proton therapy beams. *Phys. Med. Biol.* 53:4605-4619.

Schardt D, Elsässer T and Schulz-Ertner D (2010). Heavy-ion tumor therapy: Physical and radiobiological benefits. *Rev Mod Phys* 82:383–425.

Schippers, J. M. and Lomax, A. J (2011). Emerging technologies in proton therapy. Acta Oncol. 50: 838–850.

Schömers, C., Cee, R., Feldmeier, E., Galonska, M., Peters, A., Scheloske, S. and Haberer, T (2014). Reacceleration of ion beams for particle therapy. *Proceedings of IPAC2014, Dresden. WEPRO062* .

Schulz-Ertner, D., Haberer, T., Jäkel, O., Thilmann, C., Krämer, M., Enghardt, W., Kraft, G., Wannenmacher, M. & Debus, J. (2002). Radiotherapy for chordomas and low-grade chondrosarcomas of the skull base with carbon ions. *Int. J. Radiat. Oncol. Biol. Phys.* 53(1):36-42.

Schulz-Ertner, D., Karger, C. P., Feuerhake, A., Nikoghosyan, A., Combs, S. E., Jäkel, O., Edler, L., Scholz, M., Thilmann, C. & Debus, J. (2007). Effectiveness of carbon ion radiotherapy in the treatment of skull-base chordomas. *Int. J. Radiat. Oncol. Biol. Phys.* 68(2):449-457.

Shiomi, M., Mori, S., Shinoto, M., Nakayama, Y., Kamada, T. and Yamada, S (2016). Comparison of carbon-ion passive and scanning irradiation for pancreatic cancer . *Radiotherapy and Oncology* 119:326–330 .

REFERENCES

Simeonov, Y., Penchev, P., Ringbæk, T.P., Brons, S., Weber, U. and Zink, K (2016). SU-F-T-184: 3D Range-Modulator for Scanned Particle Therapy: Development, Monte Carlo Simulations and Measurements. *Med. Phys.* 43:3504.

Simeonov, Y., Weber, U., Penchev, P., Ringbæk, T.P., Schuy, S., Brons, S., Engenhart-Cabillic, R., Bliedtner, J. and Zink, K (2017). 3D Range-modulator for scanned particle therapy: Development, Monte Carlo simulations and experimental measurements. *Phys. Med. Biol.* 62(17):7075-7096.

Titt, U., Mirkovic, D., Sawakuchi, G., Perles, L., Newhauser, W. D., Taddei, P. & Mohan, R. (2010). Adjustment of the lateral and longitudinal size of scanned proton beam spots using a pre-absorber to optimize penumbrae and delivery efficiency. *Phys. Med. Biol.* 55(23):7097–7106.

Titt, U., Sell, M., Unkelbach, J., Bangert, M., Mirkovic, D., Oelfke, U. & Mohan, R. (2015). Degradation of proton depth dose distributions attributable to microstructures in lung-equivalent material. *Med. Phys.* 42:6425.

Toftegaard, J., Lühr, A., Sobolevsky, N. & Bassler, N. (2014). Improvements in the stopping power library libdedx and release of the web gui dedx.au.dk. *J. Phys.: Conf. Ser.* 489. (1).

Toftegaard, J., Petersen, J. P. & Bassler, N. (2014). PyTRiP - a toolbox and gui for the proton/ion therapy planning system trip. *J. Phys.: Conf. Ser.* 489.

Van de Water, S., Kooy, H. M., Heijmen, B. J. M. and Hoogeman, M. S (2015). Shortening Delivery Times of Intensity Modulated Proton Therapy by Reducing Proton Energy Layers During Treatment Plan Optimization. *Int J Radiation Oncol Biol Phys*, 92(2);460-468.

REFERENCES

Van de Water, T. A., Lomax, A.J., Bijl, H.P., Schilstra, C., Hug, E.B. And Langendijk, J.A. (2012).Using a reduced spot size for intensity-modulated proton therapy potentially improves salivary gland-sparing in oropharyngeal cancer. Int. J. Radiation Oncology Biol. Phys. 82(2):313–319.

Vavilov, P. V. (1957). Ionization losses of high energy heavy particles. *Soviet Physics JETP* 5:749.

Weber, U. & Kraft, G. (1999). Design and construction of a ripple filter for a smoothed depth dose distribution in conformal particle therapy. *Phys. Med. Biol.* 44:2765-2775.

Weber, U., Becher W. and Kraft, G (2000). Depth scanning for a conformal ion beam treatment of deep seated tumours . *Phys. Med. Biol.* 45:3627–3641.

Weber, U. and Kraft, G (2009). Comparisons of carbon ions vs protons. *Cancer J.* 15:325–332.

Weber, U., Kraft, G. and Zink, K (2014). Benefit of Reducing the Distance between Patient and Nozzle and Usage of a Range Shifter. *Internation Journal of Particle Therapy,* 1(2):462-463.

Weber, U., Bliedtner, J., Brick, U., Bauch, U., Möhwald, M., Schilling, M., Ringbæk, T.P., Simeonov, Y., Trautmann, C. and Zink, K. (2015). Design und 3D-Druck von Ripple-Filtern für die Rasterscan-Bestrahlung in der Partikeltherapie [PowerPoint Slides]. *3D-Druck in der Anwendung Konferenz-Targungsband.*
Retrieved from http://edoc2.bibliothek.uni-halle.de/lssaoamb/content/titleinfo/43440

Weber, U., Bliedtner, J., Schilling, M., Iancu, G., Brick, U., Trautmann, C., Seidl, T., Ringbæk, T.P., Bassler, N. and Zink, K (unpublished). A New Design and Manufacturing Method for the Ripple Filter in Particle Therapy. *Will be submitted to PMB in 2018.*

Withers, H. R., Taylor, J.M.G., Maciejewski, B. (1998). Treatment volume and tissue tolerance. *Int J Rad Oncol Biol Phys.* 14:751–759.

World Cancer Report 2014 (2014), Edited by Stewart and Wild, *International Agency for Reseach on Cancer under World Health Organization (WHO).*

Wilson RR (1946). Radiological use of fast protons. Radiology 47:487–91.

Witt, M. (2014). *Master Thesis:* Modulationseffekte von Kohlenstofionen bei der Bestrahlung von Lungen . *Technische Hochschule Mittelhessen (University of Applied Sciences).*

Witt, M., Weber, U., Simeonov, Y. & Zink, K. (2015). U-e-t-671: Range-modulation effects of carbon ion beams in lung tissue. *Med. Phys.* 42:3491.

Wu, Q., Mohan, R., Morris, M., Lauve, A. & Schmidt-Ullrich, R. (2003). Simulations integrated boost intensity-modulated radiotherapy for locally advanced head-and- neck squamos cell carcinomas 1: Dosimetric results. *Int. J. Radiat. Oncol., Biol.* 56:573-585.

Yan, X., Titt, U., Koehler, A. M. and Newhauser, W. D. (2002). Measurement of neutron dose equivalent to proton therapy patients outside of the proton radiation field. *Nucl. Instrum. Methods Phys. Res. A* 476:429–434.

Zenklusen, S.M., Pedroni, E. and Meer, D. (2010). A study on repainting strategies for treating moderately moving targets with proton pencil beam scanning at the new Gantry 2 at PSI. *Phys. Med. Biol.* 55:5103–5121

Ziegler, J. F (1999). The stopping of energetic light ions in elemental matter. *J. Appl. Phys / Rev. Appl. Phys.* 85:1249–1272.

6. Articles

6.1 Publication 1

Fluence inhomogeneities due to a ripple filter induced Moiré effect.

6.2 Publication 2

Dosimetric comparisons of carbon ion treatment plans for 1D and 2D ripple filters with variable thicknesses.

6.2.1 Supplementary Material for Publication 2

6.3 Publication 3

Modulation power of porous materials and usage as ripple filter in particle therapy.

6.3.1 Supplementary Material for Publication 3

IOP Publishing | Institute of Physics and Engineering in Medicine Physics in Medicine & Biology

Phys. Med. Biol. **60** (2015) N59–N69 doi:10.1088/0031-9155/60/3/N59

Note

Fluence inhomogeneities due to a ripple filter induced Moiré effect

Toke Printz Ringbæk[1,2], Stephan Brons[3], Jakob Naumann[3], Benjamin Ackermann[3], Julian Horn[3], Harald Latzel[3], Stefan Scheloske[3], Michael Galonska[3], Niels Bassler[1,4], Klemens Zink[2,5] and Uli Weber[2,5]

[1] Department of Physics and Astronomy, Aarhus University, Nordre Ringgade 1, 8000 Aarhus C, Denmark
[2] Technische Hochschule Mittelhessen (THM), Wiesenstraße 14, 35390 Gießen, Germany
[3] Heidelberger Ionenstrahl-Therapiezentrum (HIT), Universitätsklinikum Heidelberg, Im Neuenheimer Feld 672, 69120 Heidelberg, Germany
[4] Department of Experimental Clinical Oncology, Aarhus University Hospital, Nørrebrogade 44, 8000 Aarhus, Denmark
[5] Universitätsklinikum Gießen und Marburg, Klinikstraße 33, 35352 Gießen, Germany

E-mail: tpr@phys.au.dk

Received 10 July 2014, revised 2 November 2014
Accepted for publication 26 November 2014
Published 15 January 2015

Abstract

At particle therapy facilities with pencil beam scanning, the implementation of a ripple filter (RiFi) broadens the Bragg peak, so fewer energy steps from the accelerator are required for a homogeneous dose coverage of the planning target volume (PTV). However, sharply focusing the scanned pencil beams at the RiFi plane by ion optical settings can lead to a Moiré effect, causing fluence inhomogeneities at the isocenter. This has been experimentally proven at the Heidelberg Ionenstrahl–Therapiezentrum (HIT), Universitätsklinikum Heidelberg, Germany.

150 MeV u^{-1} carbon-12 ions are used for irradiation with a 3 mm thick RiFi. The beam is focused in front of and as close to the RiFi plane as possible. The pencil beam width is estimated to be 0.78 mm at a 93 mm distance from the RiFi. Radiographic films are used to obtain the fluence profile 30 mm in front of the isocenter, 930 mm from the RiFi. The Monte Carlo (MC) code SHIELD-HIT12A is used to determine the RiFi-induced inhomogeneities in the fluence distribution at the isocenter for a similar setup, pencil beam widths at the RiFi plane ranging from $\sigma_x^{\mathrm{RiFi}} = 0.56$ to 1.2 mm and for scanning step sizes ranging from 1.5 to 3.7 mm. The beam application and monitoring system (BAMS) used at HIT is modelled and simulated.

When the width of the pencil beams at the RiFi plane is much smaller than the scanning step size, the resulting inhomogeneous fluence distribution at the RiFi plane interfers with the inhomogeneous RiFi mass distribution and fluence inhomogeneity can be observed at the isocenter as large as an 8% deviation from the mean fluence. The inverse of the fluence ripple period at the isocenter is found to be the difference between the inverse of the RiFi period and the inverse of the scanning step size.

We have been able to use MC simulations to reproduce the spacing of the ripple stripes seen in films irradiated at HIT. Our findings clearly indicate that pencil beams sharply focused near the RiFi plane result in fluence inhomogeneity at the isocenter. In the normal clinical application, such a setting should generally be avoided.

Keywords: ripple filter, ion beam therapy, pencil beam scanning, mini ridge filter, raster scanning, inhomogeneities, ion optical beam focusing

(Some figures may appear in colour only in the online journal)

1. Introduction

The homogeneous coverage of the planning target volume (PTV) with pristine beam of mono-energetic carbon ions would require an increased number of energy steps, resulting in unreasonable time for dose delivery, especially at low penetration depths due to the corresponding low energy straggling (Vavilov 1957). The ripple filter (RiFi) is a thin absorber with a typical thickness of 3 mm and a fine periodic rill structure with a typical period of 1.6 mm. It works as a passive energy modulator that enlarges the width of the Bragg peak (BP) so larger energy steps can be applied and a significant shortening of the treatment time can be achieved. To date, first generation RiFis (Weber and Kraft 1999) have been applied for patient therapy at the GSI Helmholtzzentrum für Schwerionenforschung, Darmstadt, Germany and at the Heidelberg Ionenstrahl–Therapiezentrum (HIT), Universitätsklinikum Heidelberg, Germany. This RiFi design is investigated in this paper.

In previous work by Ringbæk *et al* (2014), dose inhomogeneities induced by RiFis have been examined using Monte Carlo (MC) simulations with pencil beams focused at the isocenter. The placement of a RiFi in the beam path induces fine structures in the fluence distribution at target surface for targets positioned at small distances from the RiFi. These fine structures originate because of an edge scattering effect due to an inhomogeneous scattering strength caused by the alternating thickness of the RiFi. The inhomogeneities are blurred out by scattering and thus estimated to be without any clinical importance.

However, it has been seen at HIT that when focusing the scanned pencil beams sharply at the RiFi plane, lateral periodic fine structures in the fluence distribution are observed at the isocenter, 960 mm from the RiFi. These fluence ripples have a variable ripple period always larger than the RiFi period of 1.6 mm. Figure 1(*a*) shows the scan of a radiographic film irradiated at the HIT gantry. The corresponding dose profiles of the film are shown in figure 1(*b*) in the direction of the RiFi-grooves as well as orthogonal to that direction, illustrating that the structures are indeed caused by the RiFi. Measuring from bottom to peak a dose inhomogeneity of approximately 16% can be estimated and a spacing between each peak, henceforth coined λ_{ripple}, of 8.6 mm can be measured. It is found in this paper that the phenomenon can be described as a Moiré effect: a pattern that occurs when a set of lines is superimposed on another set of lines, where the sets differ in relative size, angle or spacing.

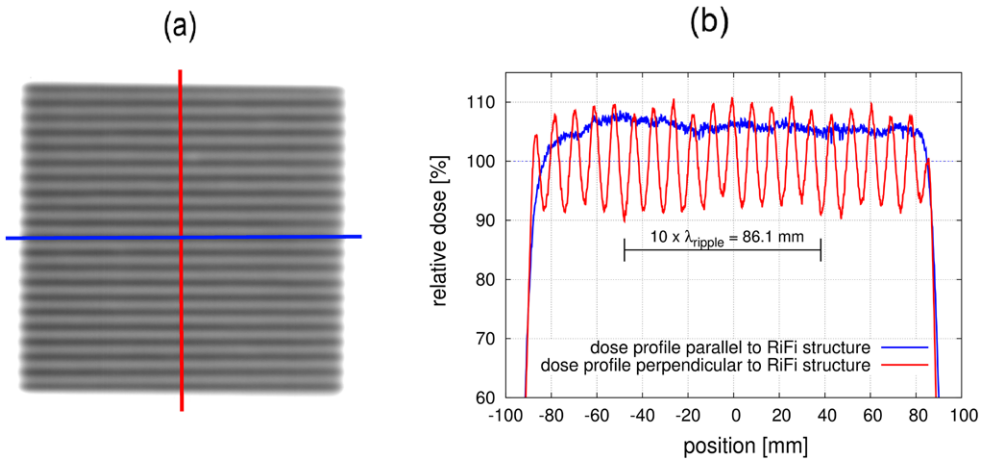

Figure 1. (*a*) Radiographic KODAK EDR2 film irradiated with carbon-12 ions (150 MeV u^{-1}) at the ion gantry (0°) displaying a pronounced stripe pattern. Contrast enhanced to show stripes. A 3 mm thick RiFi, field size 180 × 180 mm^2, spot size 6.5 mm FWHM and raster point spacing at the isocenter of 2.0 mm is used; (*b*) dose profiles of the film shown in (*a*) from which λ_{ripple} = 8.6 mm of the stripes can be deduced.

It is found that when the scan step size is not equal to the spacing of the RiFi structures and the beam is focused at or near the RiFi plane, the ripple period λ_{ripple} is given by the Moiré effect as:

$$\frac{1}{\lambda_{ripple}} = \left| \frac{1}{\lambda_{RiFi}} - \frac{1}{\lambda_{scan}} \right|, \tag{1}$$

where λ_{RiFi} is the RiFi period of 1.6 mm, λ_{scan} is the scanning step size at the focus plane and λ_{ripple} is the period of the Moiré fluence ripples. In this work this is experimentally shown at HIT as well as by MC simulations based on the experimental setup, using the MC particle transport code SHIELD-HIT12A (Hansen *et al* 2012a 2012b).

We present an analytical model for beam divergence and beam focusing similar to the Fermi-Eyges formalism, with the term 'focused beam' referring to a beam that converges to some minimum width at a certain distance from its originating point after which it diverges. Our investigation will be relevant only in one lateral dimension.

At particle facilities, the ion beams are usually focused and it is the opinion of the authors that the effect described in this paper has relevance for all existing and future facilities using active scanning techniques with ions heavier than protons.

2. Materials and methods

2.1. The Monte Carlo code SHIELD-HIT12A and the beam model

SHIELD(-HIT) is a MC code specialized for ion therapy that strains from the SHIELD code (Dementyev and Sobolevsky 1999) (changelog at https://svn.nfit.au.dk/trac/shieldhit), validated in works concerning particle therapy (Bassler *et al* 2008, Lühr *et al* 2012, Hansen *et al* 2012a, Bassler *et al* 2014). In SHIELD-HIT12A, the RiFi is implemented in a similar way as

described by Bassler *et al* (2010) with a given periodic form perpendicular to the beam axis. External ICRU49 and 73 stopping power tables are used from the open-source stopping power library libdEdx (Toftegaard *et al* 2012, Toftegaard *et al* 2014, Lühr *et al* 2012).

The BAMS by Siemens based on the original design from GSI (Haberer *et al* 1993, Kraft and Weber 2011), currently in use at HIT, is modelled as illustrated in figure 2(*a*) for use in SHIELD-HIT12A. The scattering and the energy straggling effects induced by the BAMS have been the included in the simulations. In front of the BAMS, 320 mm from the RiFi, a vacuum exit window is modelled. The BAMS then consists of 3 identical ionization chambers (IC1–IC3), 2 multiwire proportional counting chambers (MWPC-1 and MWPC-2) with multiwire grids and the RiFi. The RiFi is set to start at $z = 320$ mm, the vacuum exit window at $z = 0$ mm and the five chambers spans a range 257 mm from $z = 22$ mm to $z = 286$ mm. The simulated pencil beams originate just in front of the BAMS. Each tungsten wire in the multiwire grid has a diameter of 50 μm and an intermediate distance of 1 mm. The inhomogeneous mass distribution in the MWPCs leads to fluence inhomogeneities seen in simulations as well as in experiments to disappear a few centimeters behind the RiFi.

2.2. Ion optics and phase space distribution

For the distribution of the ion beam we present an analytical description of a (de-)focused beam with a Gaussian distribution that has been implemented in SHIELD-HIT12A. The description is a simplified form of the Fermi-Eyges formalism (Eyges *et al* 1948, Hollmark *et al* 2004), and is a model for the ion optical phase space distribution (lateral position versus angle for one dimension). At the inititalization position of the beam $z = 0$, e.g. at the vacuum window, see figure 2, the phase space distribution is given as:

$$F_{z=0}(x,\alpha) = C \exp\left[\frac{-1}{2}\left(\frac{(x-k\alpha)^2}{\hat{\sigma}_x^2} + \frac{\alpha^2}{\sigma_\alpha^2}\right)\right] \tag{2}$$

Here k is the distance in the z-direction to the beam waist, henceforth coined the focus parameter, α the angle of the particle trajectory relative to the z-axis, $\hat{\sigma}_x$ the beam width for the undisturbed beam in the focus plane at $z = -k$ as shown in figure 2(*b*) and σ_α the width of the angular distribution. A negative value of k desribes a convergent (focused) beam while a positive value of k describes a divergent (de-focused) beam (see figure 2). This ion distribution caused by optical settings will be assumed for either x or y coordinates just in front of the vacuum window.

An equation for the lateral beam profile at any position z can then be found by applying a replacement for drifting $x \rightarrow x + z{\cdot}\alpha$ in equation (2) and integrating over the angle α:

$$f_z(x) = C \exp\left(-\frac{x^2}{2\tilde{\sigma}_x^2(z)}\right) \; ; \; \tilde{\sigma}_x^2(z) = \hat{\sigma}_x^2 + (z+k)^2\,\sigma_\alpha^2 \tag{3}$$

Equation (3) clarifies that the unpertubed beam would reach its lowest value $\hat{\sigma}_x$ at the focus plane $z = -k$.

However the beam propagation simulated by MC with scattering included yields a lateral beam distribution that increases with z along the BAMS and air as shown in figure 2(*b*).

2.3. Simulations of RiFi-induced inhomogeneities

A series of parallel pencil beams are focused on the RiFi-plane via the phase space distribution given in section 2.2 with $k = -320$ mm. They are afterwards superpositioned. Data sets

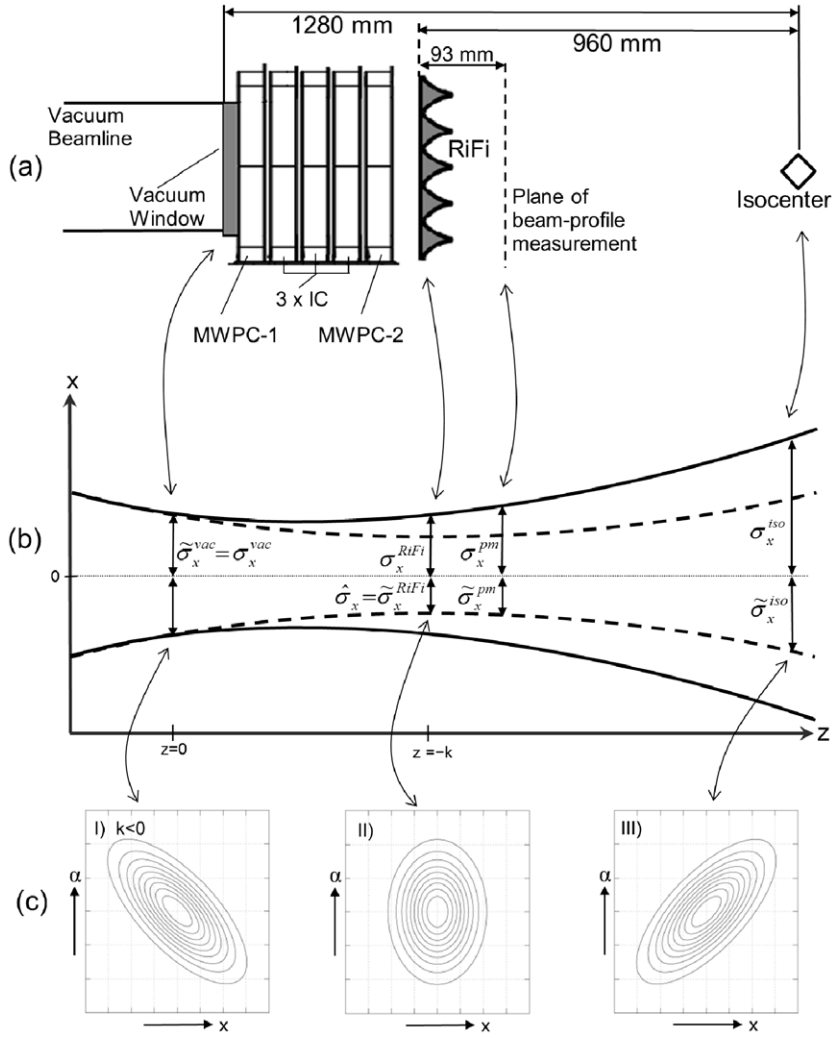

Figure 2. (*a*) The modelled BAMS is illustrated. The figure is not to scale. (*b*) The envelope ($\pm\sigma$) of pencil beams under a given influence of ion optics in vacuum (inner beam, dashed lines) and with scattering in BAMS and air (outer beam, full lines) are schematically drawn. The various beam width parameters in x-direction are shown for the theoretical vacuum case using $\tilde{\sigma}_x$ and $\hat{\sigma}_x$ for the beam waist without scattering (compare equation (3)). σ_x is the real beam width including the multiple scattering given by MC calculations. Thin arrows indicate the positions of the pencil beam drawing in terms of the BAMS shown in (*a*). The plane of measurement where the beam width σ_x^{pm} has been measured is shown. (*c*) The particle phase space shows the three cases for the focused beam at 'initializing point' $z = 0$, the beam at the focus plane $z = -k$ and for the de-focused beam at the isocenter. The connection to (*b*) is for illustrative purposes only.

are generated for a 3 mm thick RiFi and a 150 MeV u^{-1} carbon-12 ion beam, matching the experimental setup. The beam width at the focus position $\hat{\sigma}_x$ of each pristine pencil beam and the scanning step size λ_{scan} are adjustable parameters in SHIELD-HIT12A. Values of $\hat{\sigma}_x$ ranging from 0.3 mm to 1.0 mm were assigned as MC input parameters and correspond to values

of σ_x^{RiFi} (scattering included) from 0.56 mm to 1.2 mm and values of σ_x^{pm} from 0.78 mm to 1.31 mm respectively. The values σ_x^{RiFi} and σ_x^{pm} have been found by Gaussian fits to the MC data. Due to an uncertainty in the beam divergency σ_α, data sets are obtained for $\sigma_\alpha = 0.5$ mrad and $\sigma_\alpha = 1.0$ mrad.

When scoring fluence distributions, 60 mm are scored in the x-direction, in which the RiFi mass distribution is inhomogeneous, with a 0.05 mm/bin resolution, corresponding to the diameter of a MWPC wire. In the y-direction a single 60 nm bin is used, leading to an integration along the y-direction which improves the quality of the results by reducing the statistical noise. In the z-direction, the direction of the primary beam, the bin size is 1 mm/bin.

In order to obtain the fluence inhomogeneity $\Delta I / I = \dfrac{I_{\max} - I_{\mathrm{mean}}}{I_{\max}}$ from the fluence profiles, with I being the intensity, the oscillating fitting procedure described in Ringbæk *et al* (2014) has been used.

2.4. Measurements of RiFi-induced fluence inhomogeneities

At the ion gantry at HIT, KODAK EDR2 radiographic films placed 30 mm in front of the isocenter, 930 mm from a 3 mm RiFi, are irradiated with 150 MeV u^{-1} carbon-12 ions with a lateral field size of 180 × 180 mm^2. Data are obtained with raster point spacings at the isocenter $\lambda_{\mathrm{scan,iso}}$ of 1.5, 1.6, 1.7, 1.8 and 2.0 mm. The films have been scanned with the VIDAR scanner and a calibration for the relation between fluence and gray values of the films have been applied. Fluence profiles have thus been obtained and fitted with the above mentioned fitting procedure. A beam width of $\sigma_x^{\mathrm{pm}} = 0.78$ mm at a 93 mm distance from the RiFi was assumed for simulations; this value was measured in a previous experimental setup.

The initial angular distribution σ_α could not be precisely estimated by experiments. From beam spot widths measured at various distances from the vacuum exit window the value of σ_α is found to be in between 0.5 mrad and 1.0 mrad. Therefore a corresponding uncertainty arises when comparing σ_x^{RiFi} and σ_x^{pm}. This issue will be discussed in section 4.

3. Results

In figure 3 simulated 2D fluence distributions are shown from the originating point of the pencil beams to the isocenter (black lines at $z = 1280$ mm) and beyond. A RiFi is located at $z = 320$ mm in the top and bottom figures. For $\sigma_x^{\mathrm{RiFi}} = 0.63$ mm in middle and bottom figures the low ratio of $\sigma_x/\lambda_{\mathrm{scan}}$ leads to the inhomogeneities observed in the BAMS at z-values below 320 mm. An interference from this inhomogeneity with the RiFi-period λ_{RiFi} then results in the Moiré effect observed at the isocenter with period $\lambda_{\mathrm{ripple}}$ larger than λ_{RiFi}, as seen in the bottom figure. To show this in more detail, the region of the RiFi has been enlarged.

Examples of measured fluence distributions obtained from radiographic films are shown in figure 4 for various values of $\lambda_{\mathrm{scan,iso}}$. For each figure the inhomogeneity values $\Delta I/I$ and the periods of the fluence ripples $\lambda_{\mathrm{ripple}}$ are shown. Figure 4(a) illustrates that even for $\lambda_{\mathrm{scan,iso}}$ close to λ_{RiFi} small inhomogeneities are observed in the measurements.

In figure 5 simulated fluence distributions at the isocenter for 150 MeV u^{-1} carbon-12 ions with $\sigma_\alpha = 1.0$ mrad are shown for 2 different values of λ_{scan} and σ_x^{RiFi} given in the RiFi-plane with scattering included. It can be seen by comparing figures 5(a) and (b) that $\Delta I/I$ for a sharply focused beam with $\sigma_x^{\mathrm{RiFi}} = 0.56$ mm is as high as 5.9%, while a higher value of $\sigma_x^{\mathrm{RiFi}} = 0.7$ mm yields a $\Delta I/I$-value of 2.6% . In figure 5(c) it is shown how λ_{scan} closer to λ_{RiFi}

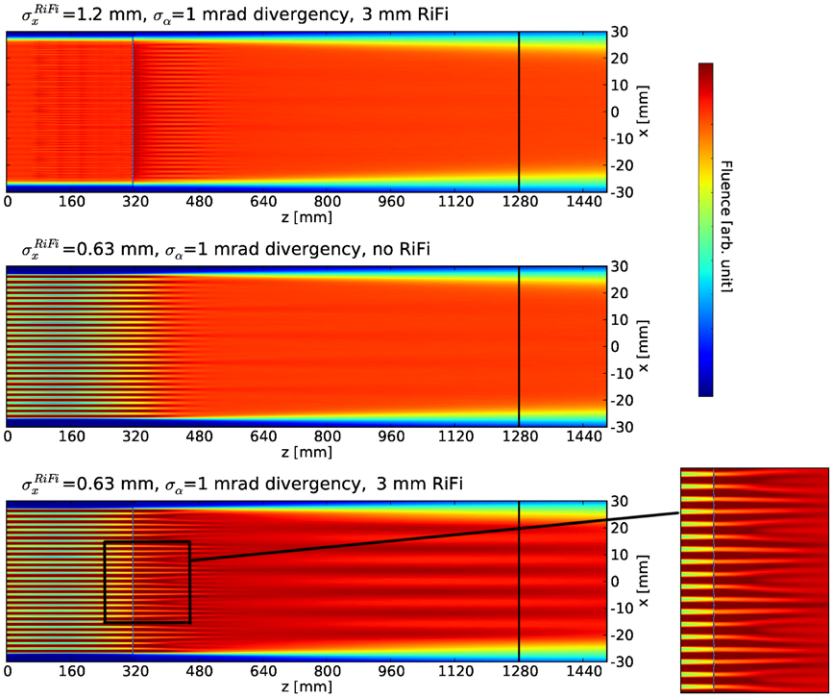

Figure 3. 2D fluence distributions for a 150 MeV u^{-1} carbon-12 ion beam with various parameters as described in the figure subtitles. The scan step size is $\lambda_{\text{scan}} = 2.0$ mm. At $z = 1280$ mm the black lines mark the isocenter. The z-axis is as shown schematically in figure 2. The enlargement in the bottom right shows the development of the Moiré effect in the fluence distribution. Small inhomogeneities in the BAMS region visible in the top figure are attributed to the inhomogeneous mass distribution in the MWPCs.

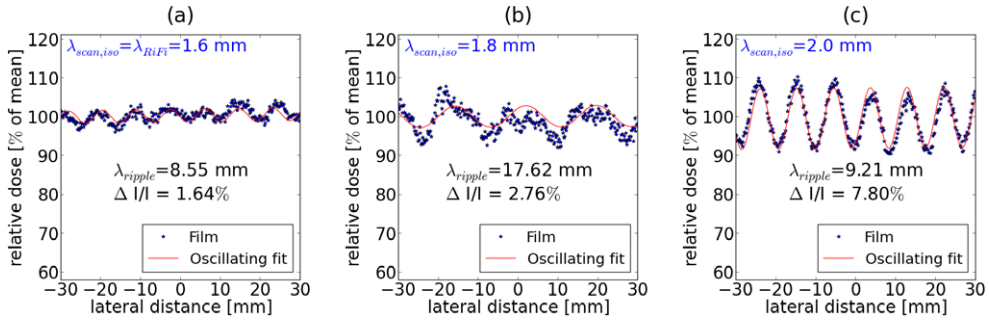

Figure 4. Measured fluence distributions for 150 MeV u^{-1} carbon-12 beams with $\sigma_x^{\text{pm}} = 0.78$ mm are shown (blue data points). The fluence distributions have been obtained from irradiated KODAK EDR2 radiographic films at $z = 1250$ mm. Various values of scanning step sizes $\lambda_{\text{scan,iso}}$ are used. The fluence inhomogeneity $\Delta I/I$ and ripple spacing λ_{ripple} calculated by fits are shown (red curves).

leads to a smaller amount of inhomogeneity. Due to the previously mentioned differences in σ_x^{RiFi} and σ_x^{pm} related to beam divergency and scattering effects, the results of the measurements shown in figures 1(*b*) and 4 are not directly comparable to the simulated data shown in figure 5. This will be adressed further below.

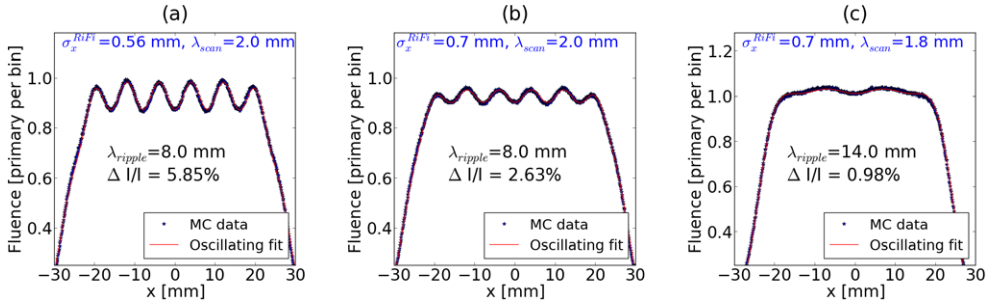

Figure 5. Simulated fluence distributions (blue data points) for 150 MeV u^{-1} carbon-12 beams obtained at z = 1280 mm for the modelled BAMS, λ_{RiFi} = 1.6 mm and beam divergency σ_α = 1.0 mrad. Various values of σ_x^{RiFi} and scanning step sizes are used. The fluence inhomogeneity $\Delta I/I$ and ripple spacing $\lambda_{\mathrm{ripple}}$ calculated by fits are shown (red curves).

The uncertainty in σ_x^{RiFi} and σ_α is found to only influence the magnitude of the inhomogeneitity $\Delta I/I$ and not the period. However, comparing figures 1(*b*) and 5(*a*), a difference in $\lambda_{\mathrm{ripple}}$ from 8.6 mm in the experimental setting to 8.0 mm from the simulated data is seen. This is attributed to a small scanning divergency, which causes a small increase of $\lambda_{\mathrm{scan,iso}}$ compared to the value in the RiFi plane λ_{scan}. The scanning divergency at the HIT gantry is very small (2%) due to special non-linear ion optics of the last gantry bending magnet. Assuming a 2% change from λ_{scan} to $\lambda_{\mathrm{scan,iso}}$ for all radiographic films, the experimental values of $\lambda_{\mathrm{ripple}}$ are found to match equation (1) as well as the simulated values of $\lambda_{\mathrm{ripple}}$.

In figure 6(*a*) it is illustrated that a lower value of σ_x^{RiFi} yields a higher value of $\Delta I/I$. All values have been obtained with λ_{scan} = 2.0 mm and σ_α = 1.0 mrad.

In figure 6(*b*) the experimental data are plotted together with simulated data. All simulated values of $\Delta I/I$ are found 30 mm in front of the isocenter in order to compare with experimental data. To obtain the values λ_{scan} at the RiFi plane, the values of $\lambda_{\mathrm{scan,iso}}$ assigned at the isocenter are enlarged by the 2% mentioned above. By plotting curves for σ_α = 0.5 mrad (stipled line curves) and σ_α = 1.0 mrad (dashed curves) as well as for σ_x^{RiFi} = 0.56 mm (dot point blue curves) and σ_x^{RiFi} = 0.63 mm (square point red curves) the uncertainties of the beam divergency and beam widths are shown. The experimental data (green curve) best match the simulated data set with the parameters σ_x^{RiFi} = 0.56 mm and σ_α = 1.0 mrad. The value of σ_x^{RiFi} = 0.56 mm corresponds to $\sigma_x^{\mathrm{pm}} \approx 0.78$ mm, matching the experimental conditions (see section 2.3).

The change in $\Delta I/I$ for different alignments of the MWPC wire grid and the beam spot positions relative to the RiFi as well as for different incident beam angles relative to the z-direction have been investigated. In addition, small changes in the value of k have been investigated. We conclude that focusing parallel pencil beams at the RiFi-plane and positioning the central MWPC wire on the central RiFi peak is a good approximation, resulting in a total uncertainty for $\Delta I/I$ of 0.3% for the worst case.

4. Discussion

It is found that, if pencil beams are sharply focused on the RiFi plane by the ion optics, the resulting inhomogeneous periodic fluence distribution at the RiFi plane interferes with the inhomogeneous periodic RiFi structure (see figure 3). When the scanning step size is not equal to the period of the RiFi, some beam spots hit the rills of the RiFi at their peaks, others

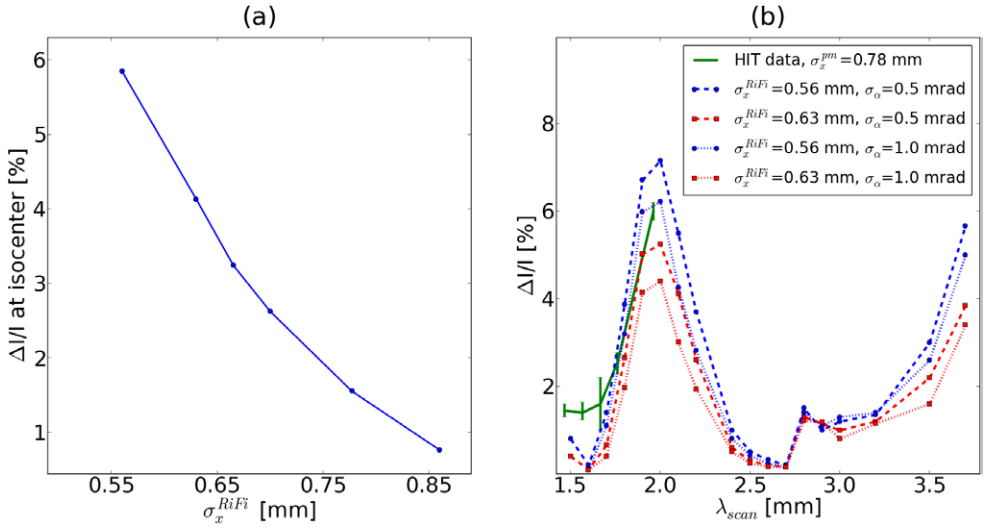

Figure 6. Measured and simulated fluence inhomogeneity *ΔI/I* for a 150 Mev u^{-1} carbon-12 ion beam. (*a*) *ΔI/I* is found at the isocenter as a function of σ_x^{RiFi} with a scanning step size λ_{scan} of 2.0 mm and $\sigma_\alpha = 1.0$ mrad. (*b*) *ΔI/I* is found at 30 mm in front of the isocenter as a function of the scanning step size λ_{scan} with various values of σ_x^{RiFi} and beam divergency σ_α. Estimated uncertainties in *ΔI/I* for the experimental data are also plotted.

at their valleys and others still in-between causing Moiré inhomogeneities to appear at the isocenter. The sharper the spots are focused in the RiFi plane, the higher the inhomogeneity values. These inhomogeneities disappear when either the RiFi is removed or the focus in the RiFi plane is enlarged by shifting the longitudinal position of the ion optical focus closer to the isocenter: no fluence inhomogeneities are seen when the beam is focused at the isocenter with $k = -1280$.

From sets of simulated data like the ones presented in section 3 it is found that the ripple period is given by the Moiré effect as in equation (1) when $\lambda_{\mathrm{scan}} \neq \lambda_{\mathrm{RiFi}}$ and the beam is focused on or near the RiFi plane. Equation (1) is indepedent of σ_α and σ_x^{RiFi} and it is seen by simulations that these two parameters only influence the fluence inhomogeneity amplitudes *ΔI/I*. For $\sigma_x > 0.5 \times \lambda_{\mathrm{RiFi}} = 0.8$ mm, as seen in figure 6(*a*), no inhomogeneity is observed and equation (1) is no longer usable. More importantly, if σ_x^{RiFi} is not much smaller than λ_{scan} no fluence inhomogeneity will hit the RiFi and no Moiré effect will be seen, as shown in figure 3 for $\sigma_x^{\mathrm{RiFi}} = 1.2$ mm. The experimental *ΔI/I* value of ≈8% (see figures 1 and 4) fits approximately with the value of 7.1% found in simulations for $\sigma_x^{\mathrm{RiFi}} = 0.56$ mm and $\sigma_\alpha = 0.5$ mrad, taking the 0.3% uncertainty described above into account.

Figure 6(*b*) shows for the simulated cases local maxima and minima of *ΔI/I* as a function of λ_{scan}. For $\lambda_{\mathrm{scan}} = n\,\lambda_{\mathrm{RiFi}}$, n being an integer, every pencil beam surpasses an identical amount of RiFi material, resulting theoretically in a total supressing of the Moiré effect. But for $\lambda_{\mathrm{scan}} \geqslant 3.2$ mm *ΔI/I* values rapidly increase due to an inhomogeneous coverage of the PTV. Since this effect is independent of the Moiré effect, $\lambda_{\mathrm{ripple}}$ values found for $\lambda_{\mathrm{scan}} \geqslant 3.2$ mm do not fit equation (1) and a non-zero value of *ΔI/I* is found at $\lambda_{\mathrm{scan}} = 3.2$ mm. At $\lambda_{\mathrm{scan}} = 2.4$ mm, the pencil beams hit every second RiFi peak location as well as every second RiFi valley location in between, which partly supresses the Moiré effect. The local minima lead to local maxima at λ_{scan} approximately equal to 2.0 and 2.8 mm.

Oscillations with $\Delta I/I \leqslant 2\%$ and $\lambda_{\text{ripple}} \approx 8$ mm are observed in experimental data for $\lambda_{\text{scan,iso}}$ equal to 1.5 mm and 1.6 mm, as seen in figures 4(*a*) and 6(*b*). This can be explained by the MWPC stripe effect. For a pencil beam at the MWPC that is sharp compared to the intermediate wire spacing of 1.0 mm, a decreased measurement precision results in systematic fluence ripples similar to those caused by inhomogenous scattering. At HIT the MWPC has a read-out resolution of $2 \cdot 1.0$ mm since two adjacent wires are connected and using $\lambda_{\text{MWPC}} = 2.0$ mm instead of λ_{RiFi} in equation (1) yields $\lambda_{\text{ripple}} = 8.0$ mm for $\lambda_{\text{scan}} = 1.6$ mm, which fits the experimental data. It is the general experience at HIT that with typical scanning step sizes of 2.0 mm or 3.0 mm, or with larger beam spot sizes than the ones investigated here, the effect is not seen at the isocenter plane.

5. Conclusion

Our findings clearly indicate that pencil beams sharply focused at the RiFi plane result in fluence inhomogeneity at the isocenter induced by the RiFi as high as 8%. The smaller the value of the initial Gaussian σ_x^{RiFi}, the bigger the value of said inhomogeneity. The effect can be explained by the interference from the modulated scanning step size to the different period of the RiFi, which causes a Moiré effect. Using MC simulations we have been able to reproduce the period and inhomogeneity amplitude of the ripple stripes seen in experiments and furthermore we present an equation for calculating this spacing using the scanning step size.

When using scanned pencil beams in conjunction with a RiFi in clinical treatments, an ion optical setting that sharply focuses pencil beams at the RiFi plane with fluence inhomogeneities at the isocenter as a result should generally be avoided by choosing different ion beam optics, if possible.

The phenomenon has relevance for all existing and future facilities utilizing active scanning treatments with ions heavier than protons where RiFis are needed to obtain a convenient irradiation time. The effect should be considered when designing or commissioning the ion optics of the beam line.

Acknowledgments

The author T P Ringbæk acknowledges the financial support of Zentrales Innovationsprogramm Mittelstand (ZIM) from the German Ministry of Economics, grant number KF2829804AK2.

References

Bassler N, Hansen D C, Lühr A, Thomsen B, Petersen J P and Sobolevsky N 2014 SHIELD-HIT12A: a Monte Carlo particle transport program for ion therapy research *J. Phys.: Conf. Ser.* **489** 012004

Bassler N, Holzscheiter M H, Jäkel O, Kovacevic S K, Knudsen H V and The AD-4/ACE Collaboration 2008 The antiproton depth-dose curve in water *Phys. Med. Biol.* **53** 793–805

Bassler N, Kantemiris I, Engelke J, Holzscheiter M and Petersen J B 2010 Comparison of optimized single and multifield irradiation plans of antiproton, proton and carbon ion beams *Radiother. Oncol.* **95** 87–93

Dementyev A V and Sobolevsky N M 1999 SHIELD: universal Monte Carlo hadron transport code: scope and applications *Radiat. Meas.* **30** 553–7

Eyges I 1948 Multiple scattering with energy loss *Phys. Rev. Lett.* **74** 1534–5

Haberer T, Becher W, Schardt D and Kraft G 1993 Magnetic scanning system for heavy ion therapy *Nucl. Instrum. Methods* A **330** 296

Hansen D C, Lühr A, Herrmann R, Sobolevsky N and Bassler N 2012a Recent improvements in the shield-hit code *Int. J. Radiat. Biol.* **88** 195–9

Hansen D C, Lühr A, Sobolevsky N and Bassler N 2012b Optimizing shield-hit for carbon ion treatment *Phys. Med. Biol.* **57** 2393–409

Hollmark M, Uhrdin J, Belkic D, Gudowska I and Brahme A 2004 Influence of multiple scattering and energy loss straggling on the absorbed dose distributions of therapeutic light ion beams: I. analytical pencil beam model *Phys. Med. Biol.* **49** 3247–65

Kraft G and Weber U 2011 Tumor therapy with ion beams *Handbook of particle detection, imaging* vol 1 ed C Grupen and I Buvat (Berlin: Springer) p 1179 chapter 47

Lühr A, Toftegaard J, Kantemiris I, Hansen D C and Bassler N 2012 Stopping power for particle therapy: the generic library libdedx and clinically relevant stopping-power ratios for light ions *Int. J. Radiat. Biol.* **88** 209–12

Ringbæk T P , Weber U, Thomsen B, Petersen J B B and Bassler N 2014 Monte carlo simulations of new 2d ripple filters for particle therapy facilities *Acta Oncol.* **53** 40–9

Toftegaard J, Lühr A and Bassler N 2012 libdedx Online available: http://libdedx.sf.net

Toftegaard J, Lühr A, Sobolevsky N and Bassler N 2014 Improvements in the stopping power library libdEdx and release of the web GUI dedx.au.dk *J. Phys.: Conf. Ser.* **489** 012003

Vavilov P V 1957 Ionisation losses of high energy heavy particles *Sov. Phys. JETP* **5** 749

Weber U and Kraft G 1999 Design and construction of a ripple filter for a smoothed depth dose distribution in conformal particle therapy *Phys. Med. Biol.* **44** 2765–75

IOP Publishing | Institute of Physics and Engineering in Medicine Physics in Medicine & Biology

Phys. Med. Biol. **61** (2016) 4327–4341 doi:10.1088/0031-9155/61/11/4327

Dosimetric comparisons of carbon ion treatment plans for 1D and 2D ripple filters with variable thicknesses

Toke Printz Ringbæk[1,2,3], Uli Weber[1,4,8], Alina Santiago[2,5], Yuri Simeonov[1], Peter Fritz[6], Michael Krämer[4], Andrea Wittig[2,5], Niels Bassler[3,7], Rita Engenhart-Cabillic[2,5] and Klemens Zink[1,5]

[1] Technische Hochschule Mittelhessen (THM), Gießen-Friedberg, Germany
[2] Department of Radiotherapy and Radiation Oncology, Philipps-University, Marburg, Germany
[3] Department of Experimental Clinical Oncology, Aarhus University Hospital, Denmark
[4] GSI Helmholtzzentrum für Schwerionenforschung, Darmstadt, Germany
[5] Department of Radiotherapy and Radiation Oncology, University Medical Center Gießen and Marburg, Germany
[6] Department of Radiotherapy, St Marien-Krankenhaus, Siegen, Germany
[7] Department of Physics and Astronomy, Aarhus University, Denmark

E-mail: printzri@med.uni-marburg.de

Received 28 January 2016, revised 23 March 2016
Accepted for publication 5 April 2016
Published 20 May 2016

Abstract

A ripple filter (RiFi)—also called mini-ridge filter—is a passive energy modulator used in particle beam treatments that broadens the Bragg peak (BP) as a function of its maximum thickness. The number of different energies requested from the accelerator can thus be reduced, which significantly reduces the treatment time. A new second generation RiFi with 2D groove shapes was developed using rapid prototyping, which optimizes the beam-modulating material and enables RiFi thicknesses of up to 6 mm. Carbon ion treatment plans were calculated using the standard 1D 3 mm thick RiFi and the new 4 and 6 mm 2D RiFis for spherical planning target volumes (PTVs) in water, eight stage I non-small cell lung cancer cases, four skull base chordoma cases and three prostate cancer cases. TRiP98 was used for treatment planning with facility-specific base data calculated with the Monte Carlo code SHIELD-HIT12A. Dose-volume-histograms, spatial dose distributions and dosimetric indexes were used for plan evaluation. Plan homogeneity and conformity of

[8] Present address: GSI Helmholtzzentrum für Schwerionenforschung, Darmstadt, Germany.

thinner RiFis were slightly superior to thicker RiFis but satisfactory results were obtained for all RiFis investigated. For the 6 mm RiFi, fine structures in the dose distribution caused by the larger energy steps were observed at the PTV edges, in particular for superficial and/or very small PTVs but performances for all RiFis increased with penetration depth due to straggling and scattering effects. Plans with the new RiFi design yielded for the studied cases comparable dosimetric results to the standard RiFi while the 4 and 6 mm RiFis lowered the irradiation time by 25–30% and 45–49%, respectively.

Keywords: ripple filter, ion beam therapy, pencil beam scanning, irradiation time reduction, non-small cell lung cancer, prostate cancer, skull base chordoma

S Online supplementary data available from stacks.iop.org/PMB/61/4327/mmedia

(Some figures may appear in colour only in the online journal)

1. Introduction

For a beam delivery system based on pencil beam scanning, the homogeneous coverage of the planning target volume (PTV) with pristine Bragg peaks (BP) of mono-energetic carbon ions requires a large number of energy steps, resulting in many energy shifts from the synchrotron and consequently long dose delivery times. Such energy shifts are in the range of 3–7 s but depends heavily on the facility in question. A ripple filter (RiFi) is a stationary mini ridge filter; a thin absorber with a fine periodic structure, which works as a passive energy modulator that enlarges the BP width as a function of the maximum RiFi thickness. In turn, larger energy steps can be applied and a significant shortening of the irradiation time can be achieved at the expense of longitudinal conformation to the PTV. First generation 1D RiFis (Weber and Kraft 1999) with a 3 mm thickness have been employed for patient treatments with carbon ion beams at the Helmholtzzentrum für Schwerionenforschung (GSI), Darmstadt, the Heidelberg Ionenstrahl-Therapiezentrum (HIT), Heidelberg, Germany, the Marburg Ionenstrahl-Therapiezentrum (MIT), Marburg, Germany and at the Centro Nazionale de Adroterapia Oncologica (CNAO), Pavia, Italy. See additionally Chu *et al* (1993) for a synopsis of modulating devices of older designs like stationary ridge filters.

Disadvantages of the first generation RiFi are its one-dimensional groove shape, which requires a non-modulating base layer causing unnecessary scattering as well as a maximum thickness restricted to 3 mm (base layer included). A new second generation RiFi was developed with two-dimensional groove structures using rapid prototyping, also called stereo lithography (Bártolo 2011), which allows thicknesses of up to 6 mm with no base layer. The 2D design makes it possible to attach groove structures in the *x*- and *y*-direction—or more precisely, a fine array of pins—with holes between them, thus supporting the entire modulating structure without any base layer. The 3 mm limit of the standard RiFi is the maximum thickness possible with the CNC cutting 1D technology described in Weber and Kraft (1999). The 6 mm thickness chosen for our new design is an estimated limit with the rapid prototyping technique for producing well defined smooth peaks with a Gaussian core for very low carbon energies

The new developments of the 2D RiFi lead to a number of questions such as dose inhomogeneities induced by the alternating RiFi thickness, which we addressed in previous works (Ringbæk *et al* 2015, Ringbæk *et al* 2014). We found beam settings which reduce such inhomogeneities to an extent where the clinical performance of the RiFis is not impaired.

This work is a methodological presentation of planning with the new 2D RiFi design and the related benefits. The aim was to investigate whether or not the new thicker 2D RiFis can reduce irradiation time of treatments using scanned carbon ion beams with an equivalent dosimetric performance as compared to the standard 1D 3 mm RiFi. We investigated the performance for two thicknesses (4 and 6 mm) of the new 2D RiFi design and for the standard 1D 3 mm RiFi, henceforth coined 2D-4 mm, 2D-6 mm and 1D-3 mm respectively, on simulated spherical geometries in water as well as on selected clinical cases. We compared dosimetric indexes, dose-volume-histograms (DVHs) and dose distributions as well as estimated irradiation times. A 2D 3 mm RiFi was used for a quick comparison between a 1D and 2D RiFi of the same thickness but has not been included in the main study.

2. Materials and methods

2.1. Monte Carlo code and treatment planning system

Treatment planning was performed with the ion treatment planning system (TPS) TRiP98 (Krämer *et al* 2000, Krämer and Scholz 2000, Krämer and Durante 2010). Facility-specific physical dose kernels (base data) were generated with the Monte Carlo code SHIELD-HIT12A (Hansen *et al* 2012a, 2012b, Bassler *et al* 2014). The beam broadening in the beam application and monitoring system (BAMS) and the accelerator energy selection at MIT were also included in the planning calculations. External ICRU49 and 73 stopping power tables in SHIELD-HIT12A were used from the open-source stopping power library libdEdx (Lühr *et al* 2012, Toftegaard *et al* 2014). The TRiP98-tool rstview was applied for evaluation of the fluence dose spots and the planning visualization tool PyTRiP (Toftegaard, Petersen and Bassler 2014) was used to display CT scans, planning contours and planned dose distributions.

The generated base data for a 1D-3 mm was benchmarked against the 1D-3 mm base data already available in TRiP98 for plans with cubic and spherical PTVs. Depth-dose distributions were carefully compared visually with a close-to-perfect agreement. Base data generated by SHIELD-HIT12A as well as PyTRiP have both been used in other works (Bassler *et al* 2010).

2.1.1. Contour extensions in the treatment planning system. In order to account for the dose fall-off at the lateral PTV edges due to the finite beam width, a lateral 'virtual contour extension' is implemented into TRiP98. This contour extension is a lateral margin, in which additional dose spots are allowed around the PTV during the optimization phase and is defined as an adjustable fraction of the beam's full-width-half-maximum (FWHM) at the isocenter. Using RiFis for 3 mm energy steps or smaller, the dose fall-off in the longitudinal direction of the beam is much steeper than in the lateral direction, so that no contour extension in the longitudinal direction is necessary. However, the new RiFis enlarge the longitudinal dose fall-off to an extent, which necessitates adopting a longitudinal contour extension in the treatment planning. By comparing depth-dose profiles along the beam axis, we found a 40% and 58% increase in the 20%–80% longitudinal dose fall-off for the 2D-6 mm compared to the 1D-3 mm for 70 and 430 MeV/u carbon ions respectively, the lowest and the highest energy available for treatment. Therefore, a longitudinal contour extension was included in a slightly modified version of TRiP98 and evaluated in this study.

2.2. Patient selection and treatment planning

For systematic analysis, a series of 1- and 3-field treatment plans on spherical PTVs in a water phantom were made with PTV radii ranging from 20 to 36 mm in steps of 4 mm at

isocenter depths ranging from 75 to 175 mm in steps of 25 mm for a 1D-3 mm, a 2D-4 mm and a 2D-6 mm. Plans for spherical PTVs with radii of 20 mm and 36 mm with an isocenter depth of 60 mm were used to investigate the RiFi performance at very superficial depths as well as to compare the 1D-3 mm to the 2D-3 mm. A Hounsfield value of 50 HU was set for the PTVs, which matches average values for soft tissue tumours (Witt *et al* 2015).

The patient series were composed by eight patients with peripheral stage I non-small cell lung cancer (NSCLC), four patients with skull base chordoma and three prostate cancer patients. All NSCLC cases were previously treated with photon stereotactic body radiation therapy (SBRT) under high-frequency jet ventilation (HFJV) (Santiago *et al* 2013, 2015). The HFJV technique is a modality of mechanical ventilative support with respiratory rates far greater than the normal value and very small tidal volumes, therefore preventing any movement and deformation of the tumour with respiration. HFJV could potentially allow for hypofractionated radiotherapy with particles using scanned beams and a margin-based target contour approach (Santiago *et al* 2013). The NSCLC PTV volumes range between 14.9 and 78.3 cm^3. No dose constraints were deemed necessary due to the size and peripheral location of the tumours, while the lung should be spared as far as possible. Two beams at a horizontal angle of 0 degree and an oblique-vertical of 45 degree were used according to two fixed beam lines at MIT. In order to investigate plan quality as a function of the number of fields for each RiFi, 3-field plans were calculated by adding a vertical beam of 90 degrees to the previous beam configuration, assuming additional vertical beam lines or a rotating gantry. The effect of mini-ridge filters with thicknesses of 6.15–24.6 mm on breath-hold treatment of lung tumours has previously been studied with Monte Carlo simulations (Courneyea *et al* 2014), showing that such configurations are viable options for motion mitigation in lung tumours.

The chordoma and the prostate cancer cases have previously been treated with carbon ions at the GSI pilot project using a 1D-3 mm (Schulz-Ertner *et al* 2002, 2007, Nikoghosyan *et al* 2011). For the prostate cancer cases the PTVs range from 54.5 cm^3 to 75.9 cm^3 covering only the prostate itself, assuming a carbon ion boost planning scheme. The bladder and the rectal wall were defined to be OARs, to which no high dose was allowed. For one patient additional constraints had to be placed on the hip bones. Two opposed lateral fields were used for planning as per the clinical convention from the GSI pilot project. For the skull base chordoma cases, PTV sizes from 72.4 cm^3 to 203.4 cm^3 were selected. Constraints of 50% of the prescribed dose were given to selected organs-at-risk (OARs) of the chiasma, the eyes, the lenses and the optical nerves. Best possible overall sparing of the brainstem and the spinal cord was attempted with no high-dose being allowed to these two OARs (e.g. $V_{90} = 0\%$). Two coplanar fields were used from both sides of the head with angles matching the original setup used for treatments at the GSI.

For all patient plans, the planning objective was to deliver at least 95% of the prescribed dose to 98% of the PTV (ICRU 2007) within the given constraints.

A raster scan grid with a lateral spot-to-spot distance of 2×2 mm^2 was used for all plans. The energy step size was set equal to the maximum thickness of the RiFi in question since we found in previous work that a good rule of thumb is to use energy step sizes equal to the thickness of the corresponding RiFi in order to obtain an acceptable plan with a short irradiation time (Ringbæk *et al* 2014). Intensity-modulated optimization was used with the 'all-point' dose calculation algorithm, which is considering all neighboring raster beam spots that may contribute to a given voxel (Krämer and Durante 2010). This dose algorithm is established for carbon ion plans in terms of the beam broadening with depth (Gemmel *et al* 2008, Krämer and Durante 2010). The lateral contour extensions ranged from 0.7 to 0.9 times the FWHM of the beam in the isocenter (without target) and the longitudinal from 0.9 to 2.8. For all plans pencil

beams were focused at the isocenter with a RiFi-to-isocenter distance of 108 cm, following the setup at MIT.

All plans used for dosimetric comparisons were calculated using physically optimized dose distributions, since we found that the RiFi-induced dose ripples and dose spikes as well as the difference in dose coverage when comparing different RiFis change only marginally when comparing biologically and physically optimized dose. To prove this assumption, biologically optimized plans were compared to the physically optimized plans for selected simulated spheres and cubes in water as well as for selected skull base chordoma cases. For these treatment plans adopted for the biologically weighted dose, the local effect model LEM I (Scholz and Kraft 1996, Scholz *et al* 1997) was used with a set of RBE-data developed at the GSI (Battermann *et al* 1981, van der Kogel 1986, Krämer and Scholz 2000) as input data. The results are shown and discussed in the supplementary material (stacks.iop.org/PMB/61/4327/mmedia).

2.3. Plan evaluation and data analysis

Dose distributions and DVHs as well as the total number of energy slices n_S and the total number of beam spots n_P were obtained for each plan using TRiP98. For evaluation of the target coverage, we analyzed $V_{95\%}$, which is the volume receiving at least 95% of the prescribed dose. The dose given to 2% of the volume ($D_{2\%}$), and to 98% of the volume ($D_{98\%}$) were used as near-maximum doses and near-minimum doses respectively. To address the homogeneity of the dose coverage within the investigated volume and the planning conformity, the homogeneity index HI and the conformity index CI were defined as (Wu *et al* 2003):

$$\mathrm{HI} = \frac{D_{2\%} - D_{98\%}}{D_{\mathrm{prescribed}}} \tag{1}$$

$$\mathrm{CI} = \frac{V_{95\%}}{\mathrm{PTV}}. \tag{2}$$

The prioritized order for planning was first coverage (given as $V_{95\%}$), second HI (as low as possible) and third CI (as close to 1.0 as possible). We aimed at obtaining for each RiFi for a given treatment case similar values of $V_{95\%}$ and HI. All plans with HI > 0.080 were rejected. Since we used $V_{95\%}$ for evaluation of the coverage, we chose as a result a more conservative upper CI limit than the 2.0 from the RTOG conformity index protocol (Feuvret *et al* 2006), in which $V_{100\%}$ is used. In this work we set CI > 1.5 as a minor violation of the plan and CI > 2.0 as a major violation.

In order to estimate the irradiation time T we used the obtained n_S and n_P values and the rough estimation:

$$T = n_S \cdot t_{nS} + n_P \cdot t_{nP} \tag{3}$$

where t_{nS} is the time for a synchrotron cycle with the time for extraction subtracted and t_{nP} the time required per scanned beam spot for a given energy slice n_S. Using as an example the setup for a fast intensity controlled scanning with a synchrotron, one can assume t_{nS} to be in the range of 4–6 s and t_{nP} to be in the range of 3–8 ms. The values of n_S typically ranges from 10 to 100 while the values of n_P are in thousands or tens of thousands. T comprises the pure irradiation time from the accelerator beam request for the first slice of a field up to the last beam spot of the last slice. The time period between the fields (movement of treatment table, repositioning, eventually imaging) and the preparation time were excluded.

3. Results

3.1. Treatment plan comparisons

Figure 1 shows the physical dose distributions for 1- and 3- field treatment plans for a spherical PTV with radius 36 mm at an isocenter depth of 60 mm using 1D-3 mm and 2D-6 mm. Fine structures in the dose distribution near and around the distal edge of the PTV—henceforth called 'dose spikes'—can be seen, in particular for the 1-field 2D-6 mm case. Using more fields reduces the dose spike effect.

Table 1 shows averaged dosimetric indexes for 1-field spherical plans for different RiFis, averaging the results over all different PTV radii, isocenter depths and contour extension settings, giving the overall performance of each RiFi with standard deviations. HI and CI are found in general for all plans to increase for thicker filters. The 2D-6 mm yields nearly the same dosimetric quality as the 1D-3 mm while the 2D-4 mm even slightly increased coverage homogeneity as compared to the 1D-3 mm. To address the effect of the lateral and longitudinal contour extensions on the plans, standard deviations from the range of the contour extensions for each plan were investigated for the spherical PTVs. Standard deviations from the variations of the contour extensions and the averaging of the plans are given for $V_{95\%}$, $D_{2\%}$ and $D_{98\%}$ in table 1. CI and HI deviations were 7% and 4% respectively.

Table 2 shows averaged dosimetric indexes for 1- and 3-field spherical plans comparing the 1D-3 mm and the 2D-3 mm. The results have been averaged over a set composed by 20 and 36 mm PTV radii at isocenter depths 60 and 150 mm with variable contour extensions. Standard deviations are given. It can be seen that the 1D-3 mm and 2D-3 mm yield identical RiFi performances withing the standard deviations.

Figure 2 shows the dosimetric indexes for selected spherical PTVs with variable radius and isocenter depth as well as for all the investigated patient cases. The PTV coverage was comparable between RiFis for plans with the same number of fields with a difference of 0.1–0.7 percentage points. The lowest HI was typically reached with the thinnest RiFi, being the plans with the smallest in-depth spacing between BPs. However, CI and HI values were in general comparable for the 1D-3 mm and the 2D-4 mm, while the 2D-6 mm provided worse conformity and less sparing of surrounding normal tissue, typically with CI values enhanced by 4%–14% for the same number of fields. This reduced conformity of the 2D-6 mm is attributed to the dose spikes. The well-known tendency that PTV conformity improves as the number of field increases can be seen, independently of RiFis. The difference in the volumetric indexes for the various RiFis decreases with increasing PTV volume. The 2D-6 mm in particular performs better as the PTV volumes increase and for the two biggest NSCLC PTVs, P7 and P8, lower HI values were seen for the 2D-4 mm and 2D-6 mm compared to the in-use 1D-3 mm.

The spherical case with 20 mm radius PTV and isocenter at 60 mm water depth was selected to give an insight into the worst case scenario in terms of RiFi performances—a small, superficial PTV. All investigated RiFis perform worse for that particular planning case as compared to larger and/or deeper-seated PTVs. With the 20 mm radius PTV centred instead at a 150 mm water depth, $V_{95\%}$ and HI improved for all RiFis since for deeper penetration depths straggling and scattering effects blurred out the inhomogeneities and further broadened the BPs. For the 36 mm radius PTV centred at 60 mm depth, all RiFis performed better than for the small PTV, with the differences between the 2D-6 mm and the others being smaller than for the 20 mm radius PTV. Moving the 36 mm radius PTV to a 150 mm isocenter depth did not improve coverage and homogeneity significantly. A 3-field configuration marginally improved the indexes for the 1D-3 mm and 2D-4 mm compared to a 1-field configuration, while largely improving

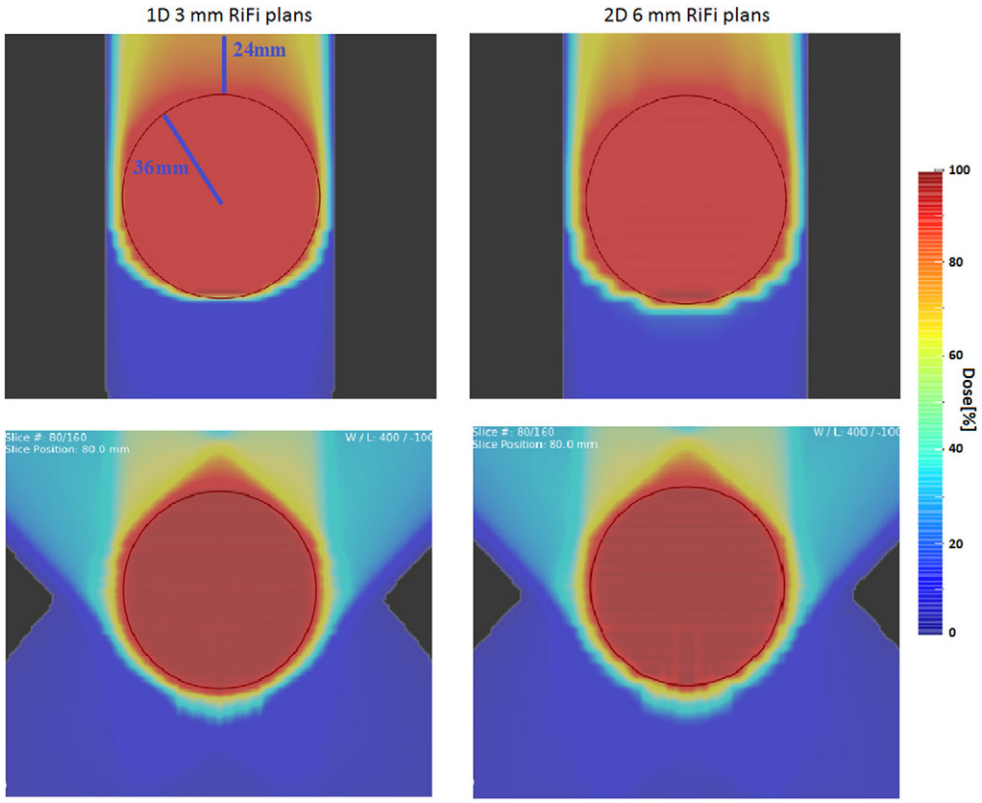

Figure 1. Physical dose distributions for selected treatment plans for a spherical PTV with radius 36 mm at a depth of 60 mm within a water phantom. Left to right show 1D-3 mm and 2D-6 mm plans while top to bottom show 1 and 3 field plans. For 1 field plans, differences can be clearly seen and might even be clinically relevant in case a critical OAR is directly adjacent to the PTV. The effect is less pronounced if multiple fields are used.

Table 1. Averaged dosimetric PTV indexes for one-field plans for spherical geometries with variable radii, isocenter depths and contour extensions for three different RiFis.

RiFi	V_{95} [%]	D_2 [%]	D_{98} [%]	CI	HI
1D-3 mm	99.9 ± 0.2	101.2 ± 0.5	97.9 ± 0.6	1.244	0.034
2D-4 mm	99.9 ± 0.2	101.1 ± 0.3	98.3 ± 0.5	1.251	0.028
2D-6 mm	99.8 ± 0.2	101.6 ± 0.3	97.6 ± 0.7	1.273	0.041

Note. Standard deviations are given for $V_{95\%}$, $D_{2\%}$ and $D_{98\%}$. CI and HI deviations are 7% and 4% respectively. All plans were calculated for physical dose.

the conformity for the 2D-6 mm. The benefits of the higher number of fields were slightly reduced although still present when going from superficial to deep-seated PTVs.

Figure 3 shows DVHs for coplanar 2-field plans for the eight NSCLC cases for the 1D-3 mm as well as for the 2D-6 mm. Figures 4 and 5 show DVHs for the four skull base chordoma cancer cases and the three prostate cancer cases respectively. For all DVHs, the 2D-4 mm plans were indistinguishable from the 1D-3 mm plans and are not displayed. As in figure 2 all patient cases are listed in order of PTV size.

Table 2. Dosimetric indexes for one-field and three-field plans with variable contour extensions for a 1D-3 mm and 2D-3 mm averaged over spherical geometries with radii 20 and 36 mm at isocenter depths 60 and 150 mm.

RiFi	Fields	V_{95} [%]	D_2 [%]	D_{98} [%]	CI	HI
1D-3 mm	1	99.8 ± 0.3	101.1 ± 0.4	97.4 ± 0.7	1.218	0.036
1D-3 mm	3	99.9 ± 0.3	100.9 ± 0.4	97.6 ± 0.6	1.162	0.033
2D-3 mm	1	99.8 ± 0.3	101.1 ± 0.5	97.4 ± 0.6	1.223	0.037
2D-3 mm	3	99.9 ± 0.3	100.7 ± 0.4	97.3 ± 0.6	1.166	0.033

Note. Standard deviations are given for $V_{95\%}$, $D_{2\%}$ and $D_{98\%}$. CI and HI deviations are 5% and 4% respectively. All plans were calculated for physical dose. The individual non-averaged data can be seen in the supplementary material.

The PTVs in the NSCLC cases were not located in proximity to critical organs-at-risk and a suitable choice of beam angles could completely spare all OARs apart from the ribs in the pathway of the beam in selected cases. For the NSCLC cases P1, P2 and P4—small and superficial PTVs where the overall performance of the thicker filter was worse than for larger PTVs—a slight increase of dose to affected ribs was observed when comparing the 1D-3 mm and the 2D-6 mm. This slight increase in dose to the ribs was deemed to have little actual impact on the quality of the plans. For the larger PTVs of the series, P5 to P8, only a very minor dose difference of less than one percent was seen for all VOIs. Even for P7—a patient case where the PTV is right next to the chest wall and a bolus had to be used to obtain a satisfactory planning result—no additional dose were seen to the chest wall when comparing 2D-4 mm and 2D-6 mm to the standard 1D-3 mm.

For the three prostate cancer cases, no differences in the dose given to the OARs were observed (see figure 4).

For the skull base chordoma cases, only very marginal differences in dose to selected OARs were observed for P1, P2 and P4 when comparing 2D-6 mm plans to the 1D-3 mm plans (see figure 5). For P3 a small increase in the dose, in particular to the brainstem and the spinal cord, can be seen but with no more than an overall integral dose increase of 5.8% to the brainstem and 7.2% for the spinal cord. No increase in maximum dose to the OARs are seen in any of the DVHs. P3 and P4 are both large tumours located next to the chiasma and the region of the eyes and as such these two cases were selected to evaluate the performance of the RiFis for PTVs in the close vicinity of radiation-sensitive OARs.

3.2. Irradiation time comparisons

Figure 6 shows the estimated irradiation times T for selected cases of spherical PTVs in water and the eight NSCLC patient cases. Similar figures for the chordoma and the prostate cancer patients are showing the same tendencies and can be found in the supplementary material. It can be seen that the use of 2D-4 mm and 2D-6 mm lead to an overall reduction of the irradiation time of 26–30% and 45–49% respectively. We found that $n_P \propto n_S$ since decreasing the number of energy slices naturally decreases the total number of beam spots. This makes n_S the most important parameter in T. A rule of thumb can be established:

$$\frac{d_2}{d_1} \propto \frac{n_{S1} + 1}{n_{S2} + 1}. \tag{4}$$

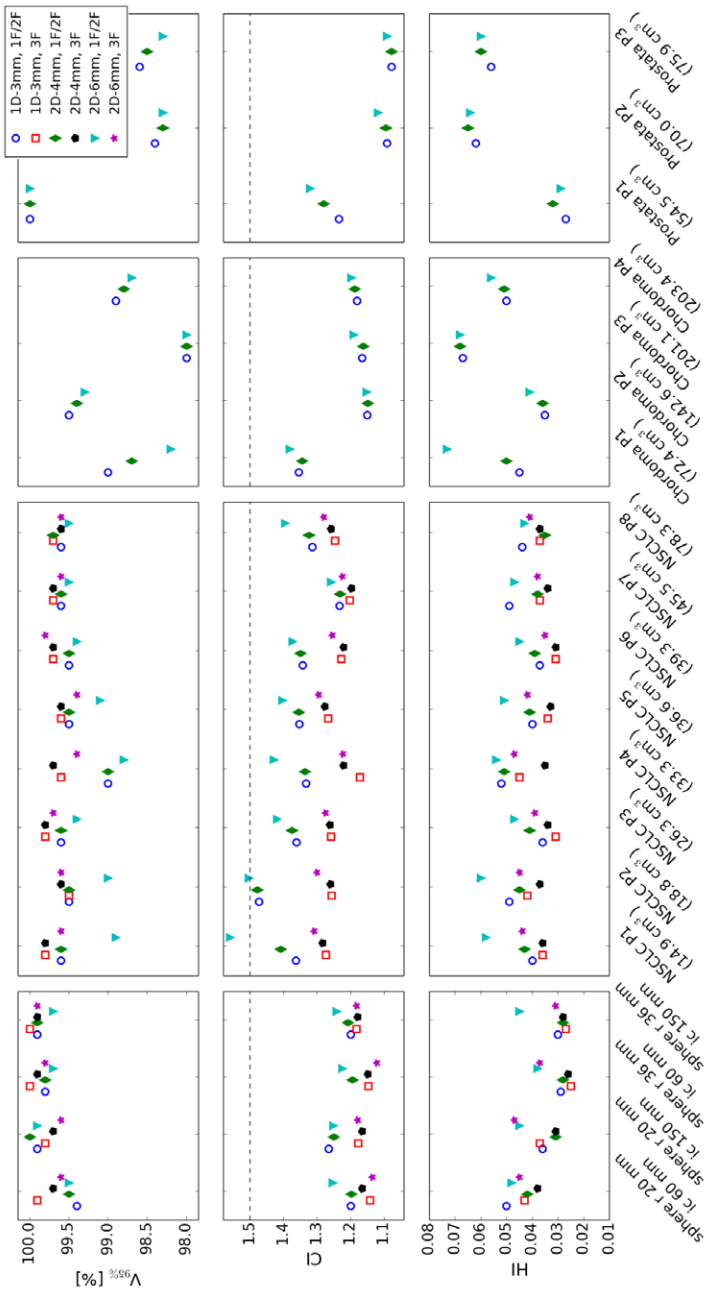

Figure 2. Dosimetric indexes for selected cases of spherical PTVs in water phantoms with different radii and isocenter depths *ic* as well as for the patient cases. Indexes are shown for 1D-3 mm, 2D-4 mm and 2D-6 mm and a variable number of fields—1F/2F refers to 1-field plans for the spheres and 2-field plans for patient cases, while 3F refers to 3-field plans for all. The dashed line at CI = 1.5 marks the afore-mentioned CI threshold that we aimed to be below. The *y*-axis for all plots are identical. Hollow data points are for the in-use 1D-3 mm while full data points are for the new 2D-4 mm and 2D-6 mm. Data tables can be found in the supplementary material.

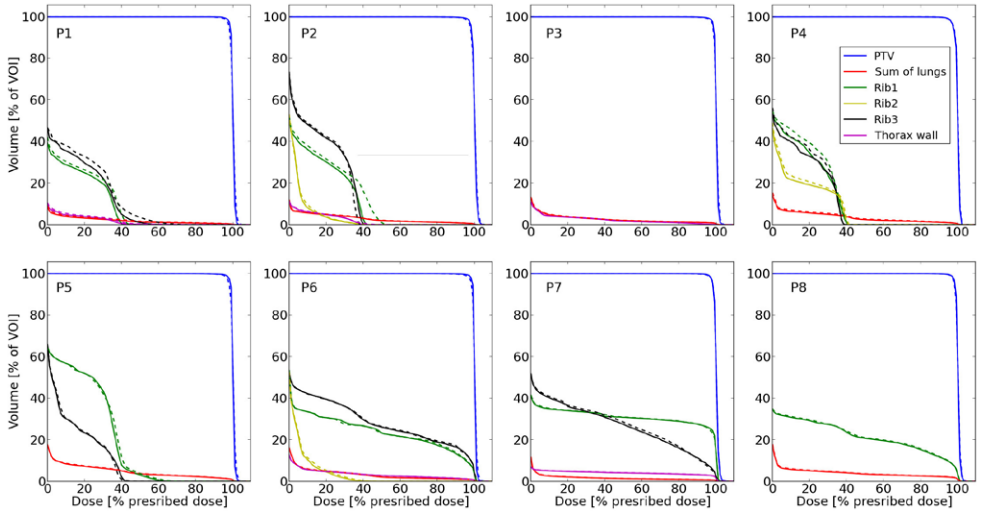

Figure 3. DVHs showing selected VOIs for the eight NSCLC cases using 2-field plans with a horizontal beam plus a tilted beam at 45 degrees to horizontal. DVHs are displayed for 1D-3 mm (full lines) and 2D-6 mm (dashed lines). 'Rib1', 'rib2' and 'rib3' corresponds to three individual ribs. All plans were calculated for physical dose. VOIs with a non-visual differences between RiFis are not displayed.

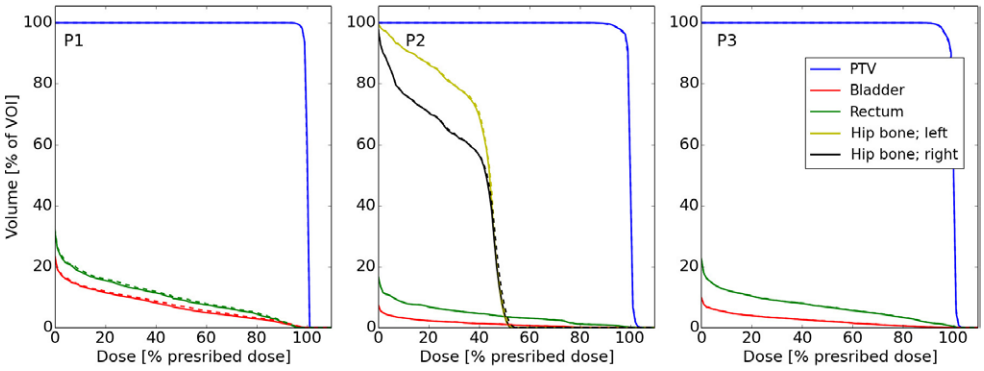

Figure 4. DVHs showing selected VOIs for the three prostate cancer patient cases using two opposive fields for plans with 1D-3 mm (full lines) or 2D-6 mm (dashed lines). All plans were calculated for physical dose. VOIs with non-visual differences between RiFis are not displayed.

Here n_{S1} and n_{S2} are values of n_S for a RiFi with thickness d_1 and d_2 respectively. The '$+1$' term arises from the fact that either the first or the last energy slice at either the proximal or distal PTV edge remains unchanged for different energy step sizes.

4. Discussion

Thicker 2D RiFis can reduce irradiation time in treatments using scanned carbon ion beams with a close-to-equivalent dosimetric performance as compared to the standard 1D 3 mm thick RiFi. However some specific exceptions exist for the 2D-6 mm due to dose spikes in the

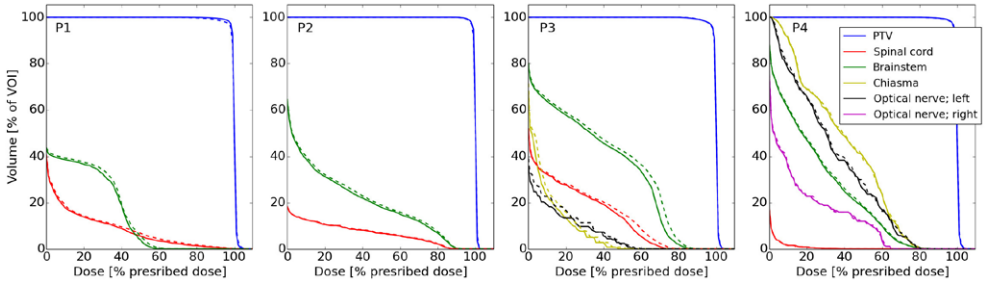

Figure 5. DVHs showing selected VOIs for the four skull base chordoma cancer patient cases using two coplanar fields at various angles for 1D-3 mm plans (full lines) or 2D-6 mm plans (dashed lines). All plans were calculated for physical dose. VOIs with a non-visual differences between RiFis are not displayed.

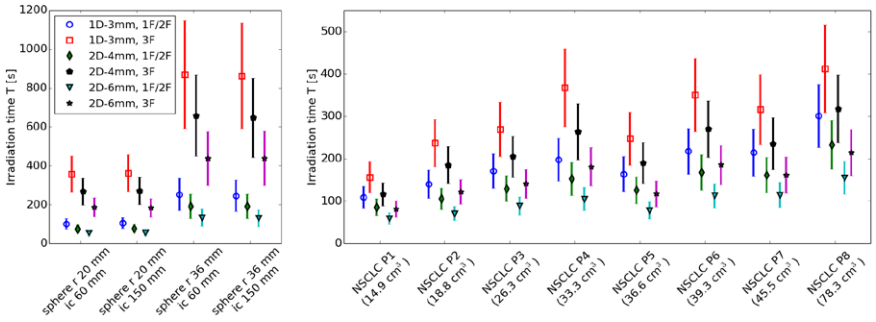

Figure 6. The total (sum over all fields) estimated field irradiation time T for selected cases of spherical PTVs in water phantoms (left side) and the NSCLC patient cases (right side). Data are shown for 1D-3 mm, 2D-4 mm and 2D-6 mm and a variable number of fields with the legend following the same syntax as in figure 2. The vertical bars are calculated using the estimated ranges for the times t_{nS} and t_{nP} as described in section 2.3. The extracted n_S and n_P values as well as similar figures for the chordoma and prostate cancer patients can be found in the supplementary material.

planned dose distributions near and around the proximal and distal edges of the PTV, which lead to slightly larger HI and CI values with occasionally marginally worse PTV coverage. The dose spikes are caused by the consequently larger spacing between the energy layers and are present for all RiFis. While they are always too small to influence clinical assessment of the dose distribution for the 1D-3 mm and 2D-4 mm, this is no longer true for the 2D-6 mm when used for superficial and very small PTVs (see figure 1). For larger PTVs, the dose spike effect was less pronounced and the location of the tumour relative to the surface influenced the RiFi performance less than for smaller PTVs. The dose spikes and the related worse conformity could hamper the performance of thicker RiFis for certain very small and irregular tumour shapes, in particular if these tumours are embedded in or located next to critical normal tissues. The use of multiple fields can reduce the dose spike effect but in a clinical setting, using thinner filters for possible specific problematic cases would typically be a better choice than adding further fields solely to compensate for deterioration of the dose distributions caused by a sub-optimal RiFi.

For the spherical PTVs, we found a dependence of the lateral and longitudinal contour extensions on the CI index. Larger contour extensions (e.g. allowing more dose around and outside the PTV edges) can lower the relative dose ripple sizes and shift the dose spikes

outside of the PTV, which in turn leads instead to a larger amount of high dose to the surrounding normal tissue. The dependency marginally increased for thicker RiFis for the lateral contour extension and strongly increased for the longitudinal contour extension. It is the opinion of the authors that a longitudinal virtual contour extension should be implemented in treatment plans with thicker RiFis than the standard 1D-3 mm.

The 1D-3 mm and 2D-3 mm performed identical on average. The difference between the 1D-3 mm and the 2D-3 mm is that the 2D-3 mm has no base layer and therefore the full 3 mm thickness of the RiFi material is used for the beam modulation effect. This gives the 2D-3 mm a stronger modulation effect than for the 1D-3 mm with a slightly decreased lateral scattering of the beam as well. The effect of the stronger modulation can be seen by comparing the n_S values for the 1D-3 mm and 2D-3 mm plans (given in the supplementary material). The lateral distributions were not investigated in detail in this work since for carbon ion plans only a small difference in the lateral scattering would be seen when comparing a 1D-3 mm to a 2D-3 mm.

The stage I NSCLC cases were selected on purpose as 'worst case scenarios' in terms of RiFi performances due to the PTVs being rather superficially located and (in most cases) small. The difference in the volumetric indexes for the various RiFis decreases with increasing PTV volume. The 2D-6 mm performed best for larger PTV volumes. For the particular case of NSCLC P8, the PTV is much larger in the longitudinal direction of the incoming beams than in the lateral directions. This indicates that—irradiation time reduction aside—while certain (small superficial) NSCLC cases might benefit most from treatments with thin RiFis, other cases (large in the longitudinal beam direction) might benefit from treatments with thicker RiFis. Since for the NSCLC cases all VOIs could be largely spared, apart from ribs in the pathway of the beam, the higher CI value and the dose spike phenomenon of the 2D-6 mm, which yields slightly increased doses to certain ribs, are not critical for those plans. For the prostate cancer cases, the slightly worse conformity for the thicker filters did not result in a higher dose to the rectal wall or the bladder. This is because of the opposing field configuration where the distal and proximal edges of one field are overlapped by the other field's proximal and distal edges, respectively. In addition, the longitudinal dose excess at the distal and proximal edges are orthogonal to the rectum wall and the bladder and do not yield any excess dose to these organs. The lateral width of the beam influences the rectum and bladder dose and is in fact marginally increased for thicker filters. However, due to the reduction in non-modulating material from the 1D to the 2D design, the new 2D-4 mm yields a widening of the lateral beam width similar to the one found for the 1D-3 mm (Ringbæk *et al* 2014). For the skull base chordoma cases however, a higher CI value could mean a larger overall dose given to structures like the brainstem or the spinal cord; OARs which for certain PTVs cannot be avoided no matter the choice of beam angle. Good examples presented in this work are the chordoma cases P3 and P4 which are large tumours (PTV volume $>200\,\mathrm{cm}^3$) located next to the chiasma and the region of the eyes. The overall dose increase to VOIs for different RiFis were however found to be in general very small and in the worst case (P3) the integral dose to the brainstem was seen to be just a few percent larger. For these specific cases mentioned—small and superficial PTVs and/or tumours close to or embedded in OARs or dose-sensitive normal tissue—a clinical evaluation would be needed in order to conclude if the reduction in treatment time is worth the slightly enlarged overall dose increase to selected VOIs. Such an evaluation would also have to take into account additional factors not addressed in this work such as the fractionation scheme and the prescribed biological weighted dose as well as the individual patient cases (e.g. reproducibility of daily positioning, overall treatment time).

In terms of irradiation time T it is important to note that the most critical aspect is n_S, the accelerator energy changes from slice to slice. Using a RiFi with twice the thickness reduces n_S by 45–49%. For irradiation of lung tumours with scanned particle beams, where organ

motion needs to be considered (Bert *et al* 2008, Bert and Durante 2011), a faster beam scanning as made possible with the new RiFi design together with techniques like gating and rescanning could help to reduce technical challenges associated with motion (Furukawa *et al* 2010). Organ motion represents a challenge in prostate cancer treatments as well, which could therefore also benefit from a shorter irradiation time for the same reasons. Apart from the possible benefit in terms of reducing the interplay effect for treatments with organ motion as stated above, a faster irradiation also increases patient comfort and counteracts spontaneous patient movements during irradiation.

For our isocentric setup with a RiFi-to-isocenter distance of 108 cm, neither lateral inhomogeneities nor range inhomogeneities were seen in the dose distribution as shown in our previous studies (Ringbæk *et al* 2014, Ringbæk *et al* 2015). We did not opt for a very small distance between the RiFi and the patient such as the 10 cm air gap in the non-isocentric setup described in the work by Gevillot *et al* (2015). Our RiFi-to-patient-distances were never less than around 70 cm of air. Very small RiFi-to-isocenter distances for a non-isocentric patient setup could reduce the enlargement of the lateral beam profile after the RiFi, thus decreasing the higher lateral scattering seen in f.ex. a configuration of two crossed RiFis of a simpler 1D design. On the other hand non-isocentric setups would greatly enlarge the daily QA and potentially add further complications to patient positioning and monitoring. Even though a crossed RiFi configuration yields a maximum thickness larger than the one for a single individual RiFi, satisfactory patient plans with a BP spacing of 6 mm (as presented in this paper) can only be obtained by introducing a newly designed RiFi with a thickness of 6 mm (like the 2D-6 mm) rather than the crossing of conventional RiFis currently in clinical use.

While TRiP98 was the TPS used in this work, the thicker 2D RiFis would also be implementable in other commercial TPSs. The only other commercial TPS for scanned ion beams, Syngo (Siemens, Erlangen, Germany), also has lateral and longitudinal virtual contour extensions implemented and is able to handle external base data files like new depth-dose distributions. Using the Syngo TPS, the implementation of and treatment planning with the new 2D RiFi design is thought to be similar to that shown in this work. It is the opinion of the authors that the 2D-4 mm, having not more than a 1/3 increase in thickness compared to the 1D-3 mm, can be easily implemented in all beam delivery systems and TPSs, which already incorporate the 1D-3 mm.

5. Conclusion

The new 2D ripple filter design with maximum thicknesses of 4 and 6 mm was used for selected carbon ion planning cases—for simulated spherical geometries in water, peripheral stage I NSCLC cases, skull base chordoma cases and prostate cancer cases—with comparable results in terms of target coverage, OAR sparing and dose homogeneity when compared with the in-use 3 mm thick RiFi of the 1D design. The 2D-4 mm can be easily implemented in beam delivery systems and treatment planning systems which already incorporate the 1D-3 mm. The 4–14% higher CI values for the 2D-6 mm compared to the 1D-3 mm require for small superficial tumours embedded in or next to irradiation sensitive normal tissue and/or OARs a careful evaluation to determine whether or not the gain in treatment time is worth the slightly increased dose to the tissue surrounding the tumour before a thicker RiFi should be opted for.

The 2D-4 mm and 2D-6 mm lowered the irradiation time by 25–30% and 45–49% compared to the 3 mm RiFi. For synchrotron based facilities with fast intensity controlled scanning, we expect when changing to 6 mm RiFis a reduction of the irradiation time from 2.2–6.4 min to 1.2–3.2 min for NCSLC patient plans.

We expect that the new design could effectively make RiFis usable in proton treatments too. Proton BPs by nature have an increased width due to scattering and energy straggling but a RiFi thickness like the 6 mm described in this paper will lead to an observable additional BP broadening for protons and can reduce the irradiation time. This will be the topic of an up-coming investigation.

Acknowledgments

The author TPR acknowledges the financial support of Zentrales Innovationsprogramm Mittelstand (ZIM) from the German Ministry of Economics, grant number KF2829804AK2. The authors acknowledge Dr G Iancu for providing input files for TRiP98 and Dr B Thomsen at the Institute of Physics and Astronomy, Aarhus, Denmark, for providing computing cluster time.

References

Bártolo P J 2011 *History of Stereolithography* (Berlin: Springer)

Bassler N, Hansen D C, Lühr A, Thomsen B, Petersen J P and Sobolevsky N 2014 SHIELD-HIT12A—a Monte Carlo particle transport program for ion therapy research *J. Phys.: Conf. Ser.* **489** 012004

Bassler N, Jäkel O, Soendergaard C S and Petersen J B 2010 Dose- and let-painting with particle therapy *Acta Oncol.* **49** 1170–6

Battermann J, Breur K, Hart G and van Preperzeel H A 1981 Observations on pulmonary metastases in patients after single doses and multiple fractions of fast neutrons and Co-60 gamma rays *Eur. J. Cancer* **17** 539–48

Bert C and Durante M 2011 Motion in radiotherapy: particle therapy *Phys. Med. Biol.* **56** R113–44

Bert C, Grözinger S O and Rietzel E 2008 Quantification of interplay effects on scanned particle beams and moving targets *Phys. Med. Biol.* **53** 2253–65

Chu W, Ludewigt B and Renner T 1993 Instrumentation for treatment of cancer using proton and light-ion beams *Rev. Sci. Instrum.* **64** 2055–122

Courneyea L, Beltran C, Tseung H S W C, Yu J and Herman M G 2014 Optimizing mini-ridge filter thickness to reduce proton treatment times in a spot-scanning synchrotron system *Med. Phys.* **41** 061713

Feuvret L, Noël G and Mazeron J 2006 Conformity index: a review *Int. J. Radiat. Oncol. Biol. Phys.* **64** 333–42

Furukawa T, Inaniwa T, Sato S, Shirai T, Mori S, Takeshita E, Mizushima K, Himukai T and Noda K 2010 Moving target irradiation with fast rescanning and gating in particle therapy *Med. Phys.* **37** 4874–9

Gemmel A, Hasch B, Ellerbrock M, Weyrather W K and Krämer M 2008 Biological dose optimization with multiple ion fields *Phys. Med. Biol.* **53** 6991–7012

Gevillot L, Stock M and Vatnitsky S 2015 Evaluation of beam delivery and ripple filter design for non-isocentric proton and carbon ion therapy *Phys. Med. Biol.* **60** 7985–8005

Hansen D C, Lühr A, Herrmann R, Sobolevsky N and Bassler N 2012a Recent improvements in the shield-hit code *Int. J. Radiat. Biol.* **88** 195–9

Hansen D C, Lühr A, Sobolevsky N and Bassler N 2012b Optimizing shield-hit for carbon ion treatment *Phys. Med. Biol.* **57** 2393–409

ICRU 2007 Prescribing, recording and reporting proton-beam therapy *ICRU Report* 78 (Bethesda, MD: International Comission on Radiation Units and Measurements)

Krämer M and Durante M 2010 Ion beam transport calculations and treatment plans in particle therapy *Eur. Phys. J.* D **60** 195–202

Krämer M, Jäkel O, Haberer T, Kraft G, Schardt D and Weber U 2000 Treatment planning for heavy-ion radiotherapy: physical beam model and dose optimization *Phys. Med. Biol.* **45** 3299–317

Krämer M and Scholz M 2000 Treatment planning for heavy-ion radiotherapy: calculation and optimization of biologically effective dose *Phys. Med. Biol.* **45** 3319–30

Lühr A, Toftegaard J, Kantemiris I, Hansen D C and Bassler N 2012 Stopping power for particle therapy: the generic library libdedx and clinically relevant stopping-power ratios for light ions *Int. J. Radiat. Biol.* **88** 209–12

Nikoghosyan A, Schulz-Ertner D, Herfarth K, Didinger B, Münter M W, Jensen A, Jäkel O, Hoess A, Haberer T and Debus J 2011 Acute toxicity of combined photon imrt and carbon ion boost for intermediate-risk prostate cancer—acute toxicity of 12c for pc *Acta Oncol.* **50** 784–90

Ringbæk T P *et al* 2015 Fluence inhomogeneities due to a ripple filter induced Moiré effect *Phys. Med. Biol.* **60** N59–69

Ringbæk T P, Weber U, Thomsen B, Petersen J B B and Bassler N 2014 Monte carlo simulations of new 2d ripple filters for particle therapy facilities *Acta Oncol.* **53** 40–9

Santiago A, Fritz P, Mühlnickel W, Engenhart-Cabilic R and Wittig A 2015 Changes in the radiological depth correlate with dosimetric deterioration in particle therapy for stage I NSCLC patients under high frequency jet ventilation *Acta Oncol.* **54** 1631–7

Santiago A, Jelen U, Ammazzalorso F, Engenhart-Cabilic R, Fritz P, Mühlnickel W and Wittig A 2013 Reproducibility of target coverage in stereotactic spot scanning proton lung irradiation under high frequency jet ventilation *Radiother. Oncol.* **109** 45–50

Scholz M, Kellerer A M, Kraft-Weyrather W and Kraft G 1997 Computation of cell survival in heavy ion beams for therapy: the model and its approximation *Radiat. Environ. Biophys.* **36** 59–66

Scholz M and Kraft G 1996 Track structure and the calculation of biological effects of heavy charged particles *Adv. Space. Res.* **18** 5–14

Schulz-Ertner D, Haberer T, Jäkel O, Thilmann C, Krämer M, Enghardt W, Kraft G, Wannenmacher M and Debus J 2002 Radiotherapy for chordomas and low-grade chondrosarcomas of the skull base with carbon ions *Int. J. Radiat. Oncol. Biol. Phys.* **53** 36–42

Schulz-Ertner D, Karger C P, Feuerhake A, Nikoghosyan A, Combs S E, Jäkel O, Edler L, Scholz M, Thilmann C and Debus J 2007 Effectiveness of carbon ion radiotherapy in the treatment of skull-base chordomas *Int. J. Radiat. Oncol. Biol. Phys.* **68** 449–57

Toftegaard J, Lühr A, Sobolevsky N and Bassler N 2014 Improvements in the stopping power library libdedx and release of the web GUI dedx.au.dk *J. Phys.: Conf. Ser.* **489** 012003

Toftegaard J, Petersen J P and Bassler N 2014 PyTRiP—a toolbox and GUI for the proton/ion therapy planning system trip *J. Phys.: Conf. Ser.* **489** 012045

van der Kogel A J 1986 Radiation-induced damage in the central nervous system: an interpretation of target cell responses *Br. J. Cancer Suppl.* **7** 207–17

Weber U and Kraft G 1999 Design and construction of a ripple filter for a smoothed depth dose distribution in conformal particle therapy *Phys. Med. Biol.* **44** 2765–75

Witt M, Weber U, Kellner D, Engenhart-Cabilic R and Zink K 2015 Optimization of the stopping-power-ratio to hounsfield-value calibration curve in proton and heavy ion therapy *Z. Med. Phys.* **25** 251–63

Wu Q, Mohan R, Morris M, Lauve A and Schmidt-Ullrich R 2003 Simulations integrated boost intensity-modulated radiotherapy for locally advanced head-and-neck squamos cell carcinomas 1: Dosimetric results *Int. J. Radiat. Oncol. Biol. Phys.* **56** 573–85

Supplementary Material

Appendix A. Biologically weighted dose and the effect on RiFi-induced dose ripples

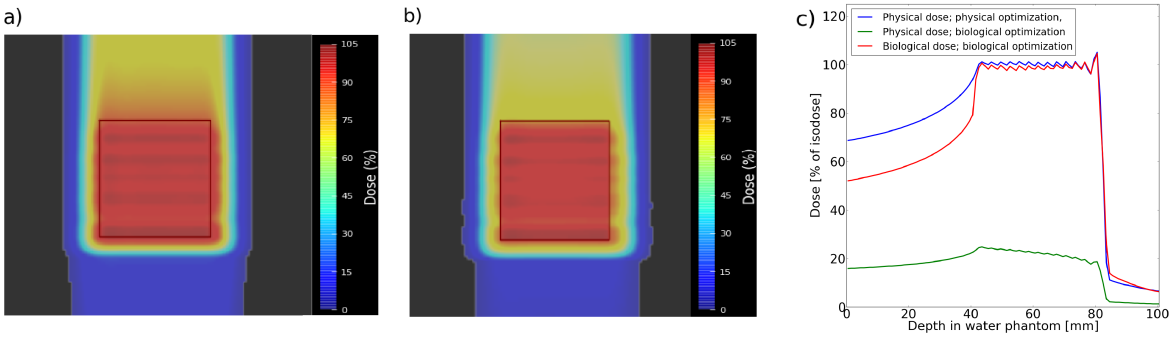

Figure A1. 2D physical (a) and biologically weighted dose distributions (b) and 1D physical and biologically weighted dose distribution along beams-eye-view (c) for a 40x40x40 mm^3 cubic planning target volume for physical and biological dose respectively. In (c) the blue line corresponds to the 2D dose distribution on a centre line on the left and the red line to the one on the right. Both plans have been calculated with a 1D-3mm.

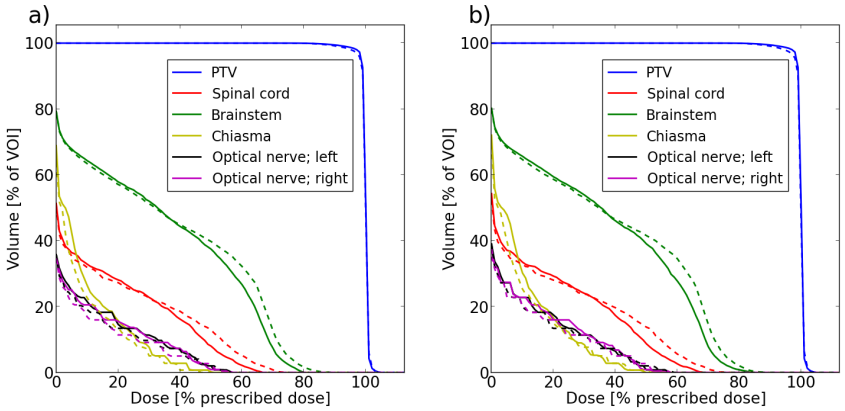

Figure A2. DVHs of a selected skull base chordoma case for plans with the 1D-3mm (a) and 2D-6mm (b) for biologically optimized dose (full lines) and physically optimized dose (dashed lines).

The difference in RiFi performance differs marginally between biologically and physically optimized planning, making it possible to use physically optimization to save computing time. This has been validated for spherical and cubic targets in water as well

as for a selected skull base chordoma patient. For the spheres and cubes superficially located targets were used for the study since this yields the largest relative dose ripple sizes for comparison. For the treatment plans adopted for the biologically weighted dose, the local effect model LEM I were used to calculate the biologically weighted dose. A set of RBE-data developed at the GSI were used as input data within this model. In our calculations, the same input data were used, namely the target tissue was set to the RBE-values developed for chordoma, whereas for the surrounding residual tissue the RBE-values developed for brain tissue were used used, both with RBE values obtained from the so-called RBE look-up tables in TRiP98. All citations and references are found in the main text of the paper.

Figure A1 shows the dose distributions for the physically and biologically optimized dose for a 40x40x40 mm^3 cube centred within a water phantom for a 1D-3mm plan. The relative size of the dose ripples change less than a few percent when comparing physical and biological dose. Similar results were found for the other two RiFi designs. Figure A2 shows the DVHs for the selected chordoma cancer case for physically optimized dose and biologically optimized dose respectively for a 1D-3mm as well as for a 2D-6mm. The plans were identical apart from the inclusion of biological optimization and parameters were tuned to the physically optimized dose situation. They do not add any information on biological dose compared to absorbed dose and only shows the similarities in terms of DVH difference between the two RiFis.

Appendix B. Dosimetric indexes

In table 1, dosimetric indexes, number of fields, energy slices nS and beam spots nP are shown for selected cases for spherical PTVs in a water phantom. Standard deviations from the variations of the contour extensions are given. CI deviations range from 2% to 8% and HI deviations range from 1% to 4%. In table 2, table 3 and table 4 dosimetric indexes, number of fields, energy slices nS and beam spots nP are shown for all RiFis for the eight NSCLS patient cases for 2- and 3-field coplanar configurations, for the skull base chordoma cancer patients for 2-field coplanar configurations and for the prostate cancer plans for 2-field opposite field configurations.

All data presented here are for plans calculated with physical dose optimization.

All values in the tables are plotted in the main text and are discussed in detail in the respective section.

Table B1. Averaged dosimetric indexes for one-field and three-field plans for four different RiFis for spherical geometries with radii of 20 and 36 mm centered in a water phantom at 60 and 150 mm depth. Total number of fields, energy slices nS and beam spots nP for each case are given as well. Standard deviations from the variations of the contour extensions are given. CI deviations range from 2% to 8% and HI deviations range from 1% to 4%. All plans were calculated for physical dose.

RiFi	Fields / nS / nP	V_{95} [%]	D_2 [%]	D_{98} [%]	CI	HI
20 mm radius,	centered at 60 mm					
1D-3mm	1 / 15 / 4724	99.4±0.2	101.8±0.2	96.9±0.8	1.200	0.050
1D-3mm	3 / 55 / 14888	99.9±0.1	101.4±0.2	97.1±0.2	1.141	0.043
2D-3mm	1 / 15 / 4823	99.7±0.1	101.3±0.3	97.0±0.5	1.199	0.043
2D-3mm	3 / 51 / 15481	99.9±0.1	101.4±0.1	97.1±0.4	1.164	0.043
2D-4mm	1 / 11 / 3603	99.5±0.1	101.5±0.1	97.3±0.4	1.198	0.042
2D-4mm	3 / 41 / 11308	99.7±0.1	101.0±0.2	97.2±0.4	1.166	0.038
2D-6mm	1 / 8 / 2619	99.5±0.2	101.8±0.3	97.3±0.2	1.253	0.048
2D-6mm	3 / 28 / 8355	99.6±0.1	101.4±0.3	96.5±0.3	1.134	0.045
20 mm radius,	centered at 150 mm					
1D-3mm	1 / 15 / 5260	99.9±0.1	101.1±0.3	97.4±0.5	1.266	0.036
1D-3mm	3 / 55 / 15835	99.8±0.1	100.9±0.3	97.2±0.6	1.177	0.037
2D-3mm	1 / 15 / 5404	100.0±0.0	101.1±0.3	97.5±0.4	1.279	0.035
2D-3mm	3 / 55 / 16444	99.8±0.1	100.4±0.2	96.9±0.7	1.172	0.035
2D-4mm	1 / 11 / 3976	100.0±0.0	101.1±0.2	97.9±0.4	1.250	0.031
2D-4mm	3 / 41 / 11731	99.7±0.1	101.4±0.3	97.0±0.5	1.165	0.044
2D-6mm	1 / 8 / 2830	99.6±0.1	101.6±0.2	97.1±0.4	1.251	0.045
2D-6mm	3 / 28 / 7914	99.6±0.4	101.7±0.3	97.0±0.9	1.179	0.047
36 mm radius,	centered at 60 mm					
1D-3mm	1 / 25 / 32140	99.8±0.2	100.7±0.1	97.7±0.3	1.204	0.029
1D-3mm	3 / 93 / 73361	100.0±0.1	100.3±0.2	97.9±0.3	1.146	0.025
2D-3mm	1 / 25 / 23200	99.8±0.2	101.0±0.4	97.4±0.4	1.209	0.036
2D-3mm	3 / 85 / 80468	100.0±0.1	100.6±0.1	97.6±0.2	1.144	0.030
2D-4mm	1 / 18 / 17369	99.9±0.1	101.1±0.1	98.2±0.6	1.194	0.028
2D-4mm	3 / 71 / 55062	99.9±0.1	100.6±0.0	98.1±1.0	1.148	0.026
2D-6mm	1 / 13 / 12377	99.7±0.2	101.6±0.4	97.7±0.4	1.225	0.038
2D-6mm	3 / 47 / 36677	99.8±0.1	100.8±0.1	97.1±0.2	1.122	0.037
36 mm radius,	centered at 150 mm					
1D-3mm	1 / 25 / 23140	99.9±0.1	100.9±0.1	97.8±0.4	1.200	0.030
1D-3mm	3 / 95 / 70428	100.0±0.2	100.9±0.1	98.2±0.4	1.182	0.027
2D-3mm	1 / 26 / 23467	99.8±0.2	100.8±0.2	97.5±0.3	1.206	0.033
2D-3mm	3 / 97 / 75796	100.0±0.1	100.3±0.1	97.7±0.3	1.183	0.024
2D-4mm	1 / 19 / 17458	99.9±0.1	100.8±0.1	98.1±0.3	1.208	0.028
2D-4mm	3 / 71 / 53030	99.9±0.1	100.9±0.1	98.1±0.6	1.179	0.028
2D-6mm	1 / 13 / 11716	99.7±0.2	101.8±0.0	97.3±0.3	1.242	0.045
2D-6mm	3 / 47 / 37006	99.9±0.1	100.9±0.1	97.7±0.3	1.183	0.031

Table B2: Averaged dosimetric indexes for two-field and three-field plans for the three different RiFis for the eight NSCLC patient cases. Total number of fields, energy slices nS and beam spots nP for each case is given as well. All plans were calculated for physical dose.

RiFi	Fields / nS / nP	V_{95} [%]	D_2 [%]	D_{98} [%]	CI	HI
NSCLC P1						
1D-3mm	2 / 19 / 2563	99.6	101.6	97.6	1.364	0.040
1D-3mm	3 / 27 / 3854	99.8	101.5	97.9	1.273	0.036
2D-4mm	2 / 15 / 1950	99.6	101.7	97.4	1.410	0.043
2D-4mm	3 / 20 / 2919	99.8	101.6	98.0	1.284	0.036
2D-6mm	2 / 10 / 1620	98.9	102.3	96.5	1.560	0.058
2D-6mm	3 / 14 / 1980	99.6	101.9	97.5	1.310	0.044
NSCLC P2						
1D-3mm	2 / 24 / 3578	99.5	102.2	97.3	1.474	0.049
1D-3mm	3 / 41 / 5831	99.5	101.9	97.7	1.256	0.042
2D-4mm	2 / 18 / 2749	99.5	102.0	97.5	1.478	0.045
2D-4mm	3 / 32 / 4505	99.6	101.7	98.0	1.260	0.037
2D-6mm	2 / 12 / 1985	99.0	102.6	96.6	1.504	0.060
2D-6mm	3 / 21 / 3042	99.6	102.0	97.5	1.300	0.045
NSCLC P3						
1D-3mm	2 / 29 / 4647	99.6	101.7	98.1	1.361	0.036
1D-3mm	3 / 46 / 7102	99.8	101.5	98.4	1.258	0.031
2D-4mm	2 / 22 / 3572	99.6	101.8	97.7	1.375	0.041
2D-4mm	3 / 35 / 5427	99.8	101.6	98.2	1.261	0.034
2D-6mm	2 / 15 / 2444	99.4	102.1	97.4	1.419	0.047
2D-6mm	3 / 24 / 3728	99.7	101.8	97.9	1.275	0.039
NSCLC P4						
1D-3mm	2 / 31 / 7654	99.0	101.4	96.2	1.333	0.052
1D-3mm	3 / 59 / 13106	99.6	101.3	96.8	1.172	0.045
2D-4mm	2 / 24 / 5848	99.0	101.3	96.2	1.337	0.051
2D-4mm	3 / 42 / 9677	99.7	101.4	97.9	1.222	0.035
2D-6mm	2 / 16 / 4490	98.8	101.6	96.2	1.429	0.054
2D-6mm	3 / 29 / 6513	99.4	102.0	97.3	1.223	0.047
NSCLC P5						
1D-3mm	2 / 26 / 6142	99.5	101.6	97.6	1.353	0.040
1D-3mm	3 / 39 / 9495	99.6	101.5	98.1	1.267	0.034
2D-4mm	2 / 20 / 4645	99.5	101.5	97.4	1.355	0.041
2D-4mm	3 / 30 / 7197	99.6	101.4	98.1	1.277	0.033
2D-6mm	2 / 12 / 3234	99.1	102.0	96.9	1.404	0.051
2D-6mm	3 / 18 / 4963	99.4	101.8	97.6	1.295	0.042

NSCLC P6						
1D-3mm	2 / 35 / 7704	99.5	101.7	98.0	1.343	0.037
1D-3mm	3 / 57 / 11834	99.7	101.3	98.2	1.228	0.031
2D-4mm	2 / 27 / 5955	99.5	101.7	97.8	1.350	0.039
2D-4mm	3 / 44 / 9078	99.7	101.3	98.2	1.222	0.031
2D-6mm	2 / 18 / 4155	99.4	101.9	97.4	1.374	0.045
2D-6mm	3 / 30 / 6413	99.8	101.5	98.0	1.255	0.035
NSCLC P7						
1D-3mm	2 / 33 / 9011	99.6	102.3	97.4	1.233	0.049
1D-3mm	3 / 48 / 13756	99.7	101.8	98.1	1.202	0.037
2D-4mm	2 / 25 / 6639	99.6	101.9	98.1	1.231	0.038
2D-4mm	3 / 36 / 10067	99.7	101.7	98.3	1.198	0.034
2D-6mm	2 / 18 / 4475	99.5	102.2	97.5	1.258	0.047
2D-6mm	3 / 24 / 7426	99.6	101.8	98.0	1.224	0.038
NSCLC P8						
1D-3mm	2 / 49 / 10143	99.6	102.0	97.6	1.314	0.044
1D-3mm	3 / 66 / 14932	99.7	101.7	98.0	1.246	0.037
2D-4mm	2 / 38 / 7738	99.7	101.6	98.1	1.324	0.035
2D-4mm	3 / 51 / 11359	99.6	101.7	98.0	1.259	0.037
2D-6mm	2 / 25 / 5489	99.5	102.1	97.8	1.395	0.043
2D-6mm	3 / 34 / 8155	99.6	101.9	97.8	1.280	0.041

Figure B1 shows the estimated scanning times T for the skull base chordoma and the prostate cancer patient cases, supplementing figure 6 in the main material and showing the same tendencies where the use of 2D-4mm and 2D-6mm lead to an overall reduction of the irradiation time of 26-30% and 45-49% respectively.

Table B3. Averaged dosimetric indexes for two-field plans for the three different RiFis for the four skull base chordoma patient cases. Total number of fields, energy slices nS and beam spots nP for each case is given as well. All plans were calculated for physical dose.

RiFi	Fields / nS / nP	V_{95} [%]	D_2 [%]	D_{98} [%]	CI	HI
Chor P1						
1D-3mm	2 / 73 / 21586	99.0	101.8	97.3	1.355	0.045
2D-4mm	2 / 57 / 16221	98.7	102.0	97.0	1.345	0.050
2D-6mm	2 / 39 / 11674	98.2	102.6	95.3	1.382	0.073
Chor P2						
1D-3mm	2 / 83 / 36182	99.5	101.1	97.6	1.150	0.035
2D-4mm	2 / 64 / 27659	99.4	101.1	97.5	1.148	0.036
2D-6mm	2 / 40 / 20673	99.3	101.3	97.2	1.152	0.041
Chor P3						
1D-3mm	2 / 105 / 51445	98.0	101.7	95.0	1.166	0.067
2D-4mm	2 / 79 / 38408	98.0	101.8	95.0	1.162	0.068
2D-6mm	2 / 49 / 25946	98.0	101.8	95.0	1.190	0.068
Chor P4						
1D-3mm	2 / 108 / 49673	98.9	102.0	97.0	1.180	0.050
2D-4mm	2 / 86 / 39970	98.8	101.9	96.8	1.187	0.051
2D-6mm	2 / 58 / 26055	98.7	102.0	96.4	1.198	0.056

Table B4. Averaged dosimetric indexes for plans using two opposed fields with three different RiFis for the three prostate cancer cases. Total number of fields, energy slices n_S and beam spots n_P for each case are given as well. All plans were calculated for physical dose.

RiFi	Fields / nS / nP	V_{95} [%]	D_2 [%]	D_{98} [%]	CI	HI
Prost. P1						
1D-3mm	2 / 45 / 17467	100.0	100.9	98.2	1.234	0.027
2D-4mm	2 / 34 / 13033	100.0	101.2	98.0	1.281	0.032
2D-6mm	2 / 24 / 9332	100.0	100.8	97.9	1.321	0.029
Prost. P2						
1D-3mm	2 / 47 / 16733	98.4	101.8	95.6	1.091	0.062
2D-4mm	2 / 38 / 12669	98.3	102.0	95.5	1.094	0.065
2D-6mm	2 / 25 / 8889	98.3	101.9	95.5	1.118	0.064
Prost. P3						
1D-3mm	2 / 57 / 18433	98.6	101.3	95.7	1.078	0.056
2D-4mm	2 / 43 / 14161	98.5	101.6	95.6	1.078	0.060
2D-6mm	2 / 30 / 9632	98.3	101.3	95.3	1.091	0.060

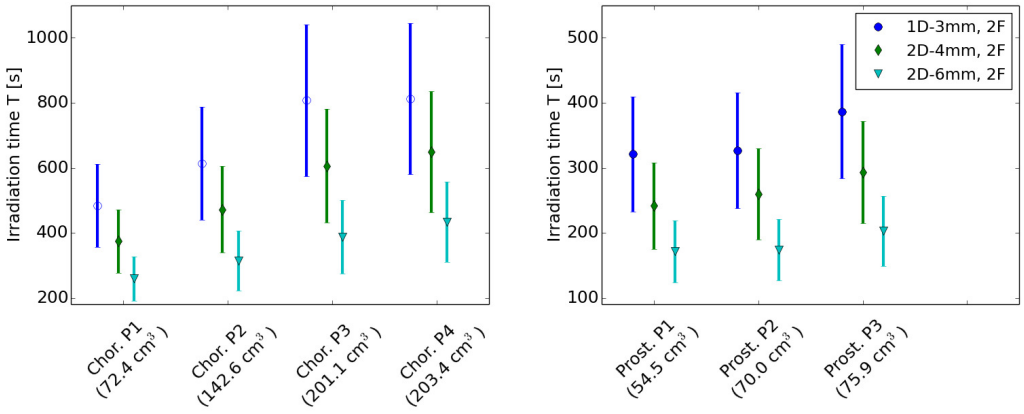

Figure B1. The total (sum over all fields) estimated field irradiation time T for the skull base chordoma cancer cases (left side) and the prostate cancer patient cases (right side). Data are shown for 1D-3mm, 2D-4mm and 2D-6mm plans using two coplanar fields from both sides of the patient. The vertical bars are calculated using the estimated ranges for the times t_{nS} and t_{nP} as described in detail in the main text in section 2.3.

IOP Publishing | Institute of Physics and Engineering in Medicine Physics in Medicine & Biology

Phys. Med. Biol. **62** (2017) 2892–2909 https://doi.org/10.1088/1361-6560/aa5c28

Modulation power of porous materials and usage as ripple filter in particle therapy

Toke Printz Ringbæk[1,2,3], Yuri Simeonov[1], Matthias Witt[4], Rita Engenhart-Cabillic[2,5], Gerhard Kraft[6], Klemens Zink[1,5] and Uli Weber[1,6,7]

[1] Technische Hochschule Mittelhessen (THM), Gießen-Friedberg, Germany
[2] Department of Radiotherapy and Radiation Oncology, Philipps-University, Marburg, Germany
[3] Department of Experimental Clinical Oncology, Aarhus University Hospital, Denmark
[4] Marburg Ion-Beam Therapy Center (MIT), Marburg, Germany
[5] Department of Radiotherapy and Radiation Oncology, University Medical Center Gießen and Marburg, Germany
[6] GSI Helmholtzzentrum für Schwerionenforschung, Darmstadt, Germany

E-mail: printzri@med.uni-marburg.de

Received 6 September 2016, revised 17 January 2017
Accepted for publication 25 January 2017
Published 14 March 2017

Abstract

Porous materials with microscopic structures like foam, sponges, lung tissues and lung substitute materials have particular characteristics, which differ from those of solid materials. Ion beams passing through porous materials show much stronger energy straggling than expected for non-porous solid materials of the same thickness. This effect depends on the microscopic fine structure, the density and the thickness of the porous material. The beam-modulating effect from a porous plate enlarges the Bragg peak, yielding similar benefits in irradiation time reduction as a ripple filter. A porous plate can additionally function as a range shifter, which since a higher energy can be selected for the same penetration depth in the body reduces the scattering at the beam line and therefore improves the lateral fall-off. Bragg curve measurements of ion beams passing through different porous materials have been performed in order to determine the beam modulation effect of each. A mathematical model describing the correlation between the mean material density, the porous pore structure size and the strength of the modulation has been developed and a new material parameter called 'modulation power' is defined as the square of the Gaussian sigma divided by the mean water-equivalent thickness of the porous absorber. Monte Carlo simulations have been performed in order to validate

[7] Present address: GSI Helmholtzzentrum für Schwerionenforschung, Darmstadt, Germany.

the model and to investigate the Bragg peak enlargement, the scattering effects of porosity and the lateral beam width at the end of the beam range. The porosity is found to only influence the lateral scattering in a negligible way. As an example of a practical application, it is found that a 20 mm and 50 mm plate of Gammex LN300 performs similar to a 3 mm and 6 mm ripple filter, respectively, and at the same time can improve the sharpness of the lateral beam due to its multifunctionality as a ripple filter and a range shifter.

Keywords: ripple filter, particle therapy, pencil beam scanning, irradiation time reduction, range modulator, range shifter, porous materials

S Supplementary material for this article is available online

(Some figures may appear in colour only in the online journal)

1. Introduction

Porous materials with microscopic structures like foam, spongy materials, lung tissue and lung substitute materials have been found to show particular properties in ion beam dosimetry, which differs from those of solid materials (Titt *et al* 2015, Witt *et al* 2015b). Ion beams passing through porous materials show a much stronger energy straggling than for solid materials (Sawakuchi *et al* 2008). In quality assurance measurements with macroscopically homogeneous but microscopically porous lung substitutes, or in treatments of real lung tissue, a strong broadening of the Bragg peak (BP) shape have been found. For materials with a fine ($<500\ \mu$m) and homogeneous pore structure size the BP enlargement can be well described by a convolution of the unperturbed reference Bragg curve for water with a normal distribution (Witt 2014, Witt *et al* 2015b). The Gaussian sigma of the normal distribution is then a parameter for the strength of the modulation effect. The beam-modulating effect of porous materials is thought to have a strong clinical relevance in lung cancer treatments because the treatment planning systems (TPS) normally assume a non-broadened BP, where in reality the modulated broader BP should be used. However, the inclusion of a porous plate in the beam path could open up for beneficial applications in particle therapy treatment planning.

In particle therapy a particularly conformal dose distribution can be achieved with the raster scanning method (Haberer *et al* 1993, Kraft and Weber 2011), which is progressively replacing the passive beam delivery technique using compensators and collimators. But because pristine BPs of heavy ion beams have small half-widths of less than 1 millimeter for small energies (<160 MeV u^{-1} for carbon-12), homogeneous coverage of the planning target volume (PTV) using the raster scanning technique can only be obtained by using a large number of accelerator energy steps. Passive energy modulators with an inhomogeneous mass distribution can be implemented in the beam path in order to widen the BP to a larger Gaussian width, thus reducing the number of required energy steps. An example of such a device is the ripple filter (RiFi); a plastic plate with a pin structure of typically 1.5 mm laterally and a 3 mm thickness (Weber and Kraft 1999). It has been found as a rule of thumb that the geometrical thickness of a RiFi with $\rho = 1.2$ g cm^{-3} corresponds to the energy step size in water made possible in treatments for this specific RiFi (Ringbæk *et al* 2014). RiFis with one-dimensional pin structures have been applied for carbon ion beam treatments for years. RiFis are commonly not used in treatments with proton beams due to the more pronounced straggling and scattering effects, meaning that their pristine BPs are already as broad as for carbon ions with a 3 mm RiFi thick and that the RiFi enlarges the lateral proton beam width as much as some millimeter. A new

improved design with two-dimensional pin structures (so-called 2D RiFis) and thicknesses of up to 6 mm, recently shown to be applicable in treatment planning, are currently being investigated (Ringbæk *et al* 2014, Ringbæk *et al* 2016), which would not only be an improvement in carbon ion therapy but could potentially be used in proton treatments as well.

Due to their beam modulating effect, plates of porous materials would broaden the BP in a similar manner to a RiFi if they are positioned in the beam path. Additionally, a porous plate can act as a range shifter, which reduces the lateral beam profile of the pencil beam since a higher initial beam energy can be chosen for the same penetration depth (Titt *et al* 2010, Weber *et al* 2014).

1.1. Aims of the study

This work contains a number of connected research goals, which together cover the aspects needed to show that plates of porous materials in raster scanning treatments with ion beams can fulfil the role of a RiFi in addition to function as a range shifter to improve the lateral beam penumbra. This includes investigations of the longitudinal energy straggling as well as the lateral scattering in porous materials, giving a complete package of the effects relevant when using porous materials with ion beams. Experiments and Monte Carlo (MC) simulations as well as a newly defined mathematical model are used to this end.

First we show that the effect of porous materials on the energy straggling can be theoretically described with a simple binary voxel model and verify this model with experimental data as well as with MC simulations. From the binary voxel model a new material parameter called 'modulation power' is defined; shown in this work to be a good parameter to represent the BP enlargement for porous materials. The modulation power parameter makes it possible to calculate the energy straggling effect of an arbitrary thickness of a porous plate for which the modulation power has been established for one thickness by Bragg curve measurements.

The RiFi role of porous plates are shown with carbon ion Bragg curve measurements for different porous materials using a water column setup as well as with MC simulations. Using this it will be investigated as an example relevant for the clinical setting if a RiFi can be replaced by plates of porous material. Filtered SOBPs obtained by using porous plates and unfiltered SOBPs obtained without any plates are calculated. By aiming for a flat SOBP in the plateau region with less than 1% dose inhomogeneity, two examples of porous plate thicknesses are found as a proof-of-concept. The effect of the range shifter is shown by MC simulations. This is done by comparing full width at half maximum (FWHM) values for a setup with a porous plate to a setup without a plate for particle beams with the same range in water.

Lastly, it will be shown by calculations and MC simulations that the difference in the lateral scattering of a beam passing through a porous material compared to a non-porous material with the same mean areal mass is negligible and that porous materials can be simulated as solid blocks when investigating the lateral scattering of an ion beam. This in turn also justifies why only simulations and not experiments are needed to illustrate the porous plates' role as range shifters.

2. Materials and methods

2.1. Mathematical model for calculation of the modulation effect of porous materials

A mathematical model describing the correlation between the mean density and pore size of a block of porous materials and the strength of its corresponding beam modulation has been developed.

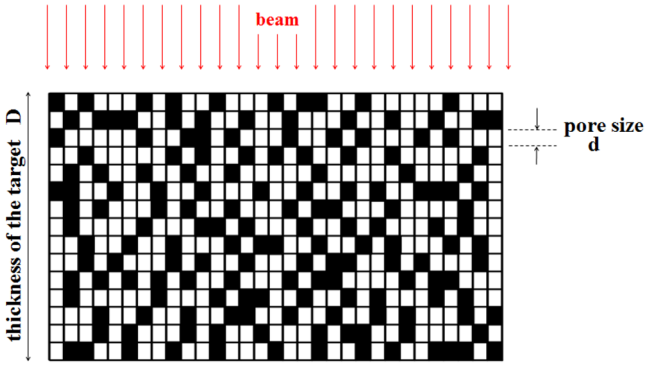

Figure 1. A geometrical model of a plate of porous material with a microscopical fine structure. The plate has the thickness D in the direction of the beam indicated by the arrows. The plate is composed of cubic voxels of length d where the dark voxels are high density material (simplified to water) and the white ones are low density material (simplified to vacuum concerning the beam-modulating effect).

The porous target is described by a simplified geometrical binary voxel model using small cubic voxels of size d. The basic idea of the model is illustrated in figure 1. The voxels with high density occurring with a probability p consist of a solid material with a density of ρ_{mat}, whereas the low density voxels are assumed to be vacuum (probability 1-p). Then

$$\rho_{\text{mean}} = \rho_{\text{mat}} \cdot p \tag{1}$$

For the example shown in figure 1 the target has $p = 0.3$ and $\rho_{\text{mean}} = 0.3\,\rho_{\text{mat}}$.

When introducing a sample of rigid material in the beam path, the BP is shifted by the water-equivalent thickness of the sample. In the case of porous or inhomogeneous samples, the shift does not match a fixed value. The particles are subjected to a different energy loss and scattering effect when passing through the different voxels in a material represented by the binary voxel model depending on their position, leading to a net range modulation. This range modulation can be described by a probability density function of the sample as described below.

The probability for hitting k voxels with high density is given by the binominal distribution:

$$P(k) = \binom{n}{k} p^k (1-p)^{n-k} \tag{2}$$

In this simplified geometrical model the number of all voxels in the beam direction (in a row in figure 1) is given by $n = D/d$. For a high value of n, the binominal distribution can be replaced by a normal distribution:

$$P(t'|\sigma, t) = \frac{1}{\sqrt{2\pi}\,\sigma} \exp\left(-\frac{(t'-t)^2}{2\sigma^2}\right) \tag{3}$$

which describes the probability for the occurrence of a path length with a water equivalent thickness of t', where t is the mean water-equivalent thickness $t = \rho_{\text{mean}} \cdot D$ of the target in the beam direction. A binominal distribution can be replaced by a Gaussian function with a width of $\sigma^2 = np(1-p)$, which gives the standard deviation of the number of hit voxels. By multiplying the number of hit voxels by a scaling factor for the voxel thickness $d \cdot \rho_{\text{mat}}$, the width of the probability distribution above can be calculated:

$$\sigma^2 = \frac{D}{d} p(1-p)(d \cdot \rho_{\text{mat}})^2 = t \cdot d \cdot \rho_{\text{mat}}(1-p) \tag{4}$$

The values σ and t are given in mass per area; we opted for g cm^{-2}. A description of σ as a quantity for the modulation is in correspondence with other works (Titt *et al* 2015). Since the most practical application is the calculation of the modulation in water, t can be given as the water-equivalent thickness and ρ_{mat} as the water-equivalent density, which then results in σ having units in water-equivalent scale too. In this work t and σ are measured with a water column (see section 2.2) and are therefore in a water-equivalent scale. In any case, the difference between two values of σ, one calculated with a water-equivalent density and the other with the mass-density, is small for polymers and lung tissue since the difference in the mass-related stopping power ratio between water and polymers is small (e.g. for polystyrene foam the ratio is roughly 0.98 (ICRU 1994)). For a metal foam however, this difference would be relevant.

The normal distribution with its width can then be used to calculate the modulation effect by a convolution of pristine Bragg curve $\text{Br}(x)$ with $P(x|\sigma, t)$:

$$\text{Br}_{\text{mod}}(x) = P(x|\sigma, t) * \text{Br}(x) = \int_{-\infty}^{\infty} P(t'|\sigma, t)\text{Br}(x + t')\, \text{d}t' \tag{5}$$

Thus, the value σ^2 gives the degree of enlargement for the BP width. Accordingly, a material characteristics for porous materials can be introduced, which we call 'modulation power' P_{mod} (by analogy with '(mass) stopping power' and '(mass) scattering power'):

$$P_{\text{mod}} \equiv \frac{\sigma^2}{t} = d(\rho_{\text{mat}} - \rho_{\text{mean}}) \tag{6}$$

P_{mod} is independent of the thickness of the porous absorber. The larger the modulation power the larger the BP enlargement. It is therefore seen that the larger the pores d of the material, the stronger the BP enlargement is (at a fixed given mean thickness t). In a homogeneous target $P_{\text{mod}} = 0$.

As will be shown in this work, the binary voxel model shows good agreement with measurements and simulations for porous materials with constant uniform micro-structures. But for more complex biological structures like lung tissue, a normal distributed modulation will be achieved only for certain paths through the lung while for other paths, the BP degradation at larger macroscopic structures in the lung (e.g. the respiratory tract or larger blood vessels) leads to a deviation from a normal-distributed convolution.

It should be noted that the intrinsic energy loss straggling in the solid part of a given material (meaning either the entirety of a rigid block or the high-density parts of a porous block) has a similar but not as strong modulation effect. The modulation power of the intrinsic energy loss straggling can be estimated, as shown in the supplementary material (stacks.iop.org/PMB/62/2892/mmedia), as a combination of the standard Bohr formula (Bohr 1915) and fitted data of ICRU 49 (ICRU 1994) for the continuous slowing down approximation (CSDA) range of ions in matter. In this context it should be pointed out that for protons, the particle range straggling by the energy loss straggling of the solid part of a given material is comparable to the range straggling induced by very fine porous materials with a small pore structure size (such as polyurethane Sika, see next section).

2.2. Bragg curve measurements

Bragg curve measurements of broad carbon-12 ion beams with initial energies of either 131.6 MeV u^{-1} or 201 MeV u^{-1} have been carried out for a range of porous materials at the Heidelberger Ionenstrahl-Therapie (HIT) using a water column (PTW PeakFinder); a

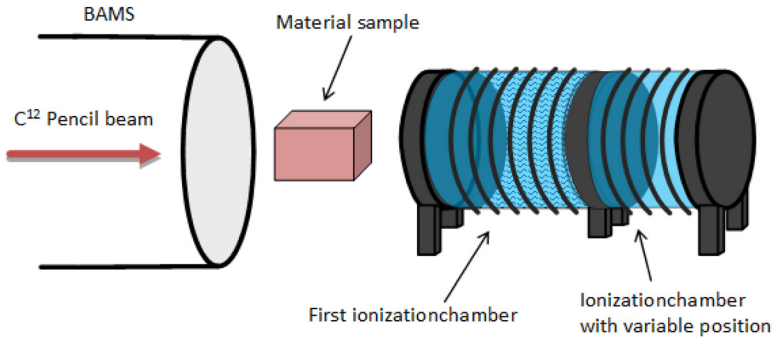

Figure 2. Schematic drawing of the experimental setup for the Bragg curve measurements based on drawing originally from Witt *et al* (2015a) and reproduced with permission from Elsevier.

schematic illustration of the setup is shown in figure 2. The investigated material samples (compare table 1 for their most important parameters) were selected in order to cover a wide range of porosity and pore structure size. The selected materials thus span a range from very homogenous foams (mostly used for model building) with values of d of 5–50 μm up to courser foams (in the forms of commercial foam padding) with pore sizes up to 300 μm. In particular we also used special lung substitute foams of the types LN300 and LN450 from the company Gammex inc. (Tissue Characterization Phantom Model 467: User Guide 2004) with relatively large values of d of 300–500 μm that are used for quality assurance for the calibration of CT Hounsfield units. In addition, one exemplary case from the work of Witt (2014) for porcine lung was selected for measurements as well, because the modulation properties of lung have a high clinical relevance. In order to compare the modulation properties of the porous materials with RiFis, Bragg curves were additionally measured for the built-in 3 mm thick 1D RiFi, which is present in the nozzle at HIT and used for patient treatments and the newer 4 and 6 mm thick 2D RiFis.

The samples of porous materials and the 2D RiFi probes were attached at the nozzle exit window. The sample porcine lung was set up some centimeters from the nozzle exit window and measurements performed *ex vivo* with the lung in an anterior-posterior position. The lung included the trachea and all macroscopic structures and had been removed in such a manner that adequate ventilation within the lung was still possible. A tube inserted into the trachea and an attached calibration syringe with a valve system made it possible to fill the lungs with a variable air volume, simulating the various states of de- and inflation of a lung under respiration. While the porcine lung setup and the obtained data will be presented in detail in other works, in this study only one measured Bragg curve of a beam travelling through the porcine lung in a medium state of inflation is included.

The reference Bragg curve and the porous material Bragg curves were measured with 131.6 MeV u^{-1} carbon-12 beams and the Bragg curves for the lung substitutes, for the porcine lung and for the RiFis were measured with 201 MeV u^{-1} since a higher energy is needed to properly pass through a fully inflated lung. This has been taken into account in the subsequent data analysis.

2.3. Calculations and simulations of Bragg curve modulation

Additionally to our experimental data analytical calculations of the modulation parameters from the measurements, of spread-out Bragg peaks (SOBPs) and of the lateral scattering of porous and non-porous materials have been performed. MC simulations have been performed

as well using FLUKA (Böhlen *et al* 2014) to show the range shifter concept, to validate the binary voxel model and to back up the calculations of the lateral scattering.

The scattering of all materials in the beam application and monitoring system (BAMS) has been taken into account in the simulations, based on the design by Siemens, which is itself based on the original design from GSI (Haberer *et al* 1993, Kraft and Weber 2011); a design currently also in use at HIT. FLUKA has additionally the capability to process DICOM files using the external pydicom module (Mason 2011). Pydicom v. 0.9.9 was used to import the binary CT data and convert it to a 3D voxel grid, thereby implementing in simulations binary voxel cubes like in our mathematical model.

To be used throughout this paper in our calculations and simulations as a working example, we chose the commercially available Gammex LN300 porous lung substitute material. The stoichiometric composition is set to be H:8.5, C:59.4, N:2.0, O:18.1, Mg:11.2, Si:0.8, Cl:0.1 in mass percent after private correspondence with the manufacturer but the precise stoichiometric composition is thought to have very little influence on the results.

2.3.1. Calculations of modulation parameters from Bragg curve measurements. For all measured material samples, the geometrical thickness D and the physical density ρ were measured (by calliper for $D < 20\,\text{cm}$ or by ruler and a scale).

The modulation parameters for the set of different porous targets are calculated from the Bragg curve measurements. There are two methods for the determination of σ. The first method is to iterate (fit) the parameters σ and t of equation (3) in a way that the convolution with the pristine Bragg curve best fits the measured Bragg curve (see equation (5)). In the second method $P(x|\sigma, t)$ is evaluated as an interpolation function of cubic splines between a set of some hundred points P_i with a distance of 50 μm or 100 μm. Then, instead of optimizing σ and t (as described above) all values of P_i are optimized for a best fit of equation (3) and the σ^2 value is calculated as the standard deviation $\int x^2 P(x|\sigma, t)\,\mathrm{d}x / \int P(x|\sigma, t)\,\mathrm{d}x$. Both methods deliver similar values of σ (within a 1–2% deviation) for all the measured artificial porous materials (foams, sponges etc). For the porcine lung sample there are larger deviations of up to 20% due to non-uniform pores in the lung or due to the special shape of the RiFi, which does not return a Gaussian probability distribution. For the same reasons, the values of P_{mod} for all RiFis are only provided to give an estimation of the relative magnitudes but do not have the character of a material parameter. The second calculation method is deemed most robust and all values of σ given in this work are therefore calculated following this method for consistency.

We can derive the mean water-equivalent density ρ_{mean} as t/D and the theoretical pore structure size d from the binary voxel model as $P_{\text{mod}}/(\rho_{\text{mat}} - \rho_{\text{mean}})$ (equation (6)) where ρ_{mat} is assumed to be $1.0\,\text{g cm}^{-3}$ water-equivalent. In particular ρ_{mat} is difficult to estimate with precision and while $1.0\,\text{g cm}^{-3}$ is thought to be a fairly realistic approximation since most samples measured in this work do not have densities deviating too much from that of water, values in the range of up to $1.2\,\text{g cm}^{-3}$ could also have been deemed realistic for certain materials. The estimated pore structure size d depends on ρ_{mat} and also on the probability p, which is even harder to determine, leading to a high uncertainty for d. The pore structure size however only provides a feeling of the porosity with little practical application. What is important to note here is that P_{mod} is a quantity obtained from fitting parameters from experimental data and therefore does not depend on ρ_{mat}.

Once the P_{mod} value of a given porous material is obtained, the BP enlargement for absorbers of any thickness can be predicted by up- or down-scaling the relevant modulation parameters and translate those to values of D.

2.3.2. Calculation of the filter effect on spread-out Bragg peaks. In order to demonstrate the RiFi effect of porous LN300 plates for energy step sizes of 3 and 6 mm, SOBPs for carbon ions are calculated with and without these plates. Unfiltered SOBPs from pristine BPs are compared with filtered SOBPs obtained when applying the LN300 plates. The unfiltered SOBPs are calculated as a superposition of the measured pristine BP at 131.6 MeV u^{-1}, shifted in depth by 3 resp. 6 mm in water. The filtered SOBPs with the modulation effect of the plates are then calculated from the corresponding 'pristine' SOBPs using equation (5) and the modulation parameters found for LN300 (see section 2.3.1). The weights for the superimposed BPs in the calculated SOBPs are the same for the non-filtered and the filtered and are optimized for the latter. The deepest BP used in the construction of the calculated SOBPs is the one that was measured. This measured BP thus fixes the position in water of the final SOBPs (after filtering). As the criteria for whether or not a porous material can fulfil the role of a RiFi, we set that the dose homogeneity in the plateau of the filtered SOBP should be better than 1% for the investigated step sizes. In this work we compared against RiFis which make step sizes of 3 and 6 mm possible. This is a conservative estimate in the sense that the 1% dose homogeneity threshold in our experience yields a slightly better filter effect than for the RiFis that we have designed for the corresponding energy steps (Ringbæk *et al* 2016). By testing different values of D for LN300 against this defined criteria, we found that thicknesses of $D = 20$ mm, respectively $D = 50$ mm, are sufficient to reach the 1% criterion. These values will be applied for further analysis throughout this work.

2.3.3. MC simulation of the modelled beam modulation effect of porous materials. In order to check the mathematical binary voxel model (section 2.1), simulations of setups with either a porous LN300 block or a solid non-porous block are performed.

To simulate the porous block, a randomized voxel cube to mimic a porous material as represented in figure 1) is implemented as a CT cube of $50 \times 50 \times 50$ mm^3 and $101 \times 101 \times 101$ voxels. The voxel positions are randomized and the dense voxels of the cube set to have a density of 1.0 g cm^{-2} with $p = 0.284$ and the remaining voxels set to vacuum. With chosen values matching our measurements of LN300 but with the 50 mm thickness yielding a flat SOBP (see above), the parameters for the CT cube is set to $d = 490$ μm, $D = 50$ mm and $t = 1.42$ g cm^{-2}, which result in $\sigma = 0.224$ g cm^{-2} for $\rho_{\text{mat}} = 1.0$ g cm^{-3}, as calculated theoretically (by equation (4)) from our measurements as described in section 2.3.1. For the non-porous case, the same physical thickness t of the plate is used ($t = p \cdot D \cdot \rho_{\text{mat}}$, section 2).

Proton BPs are scored in a water phantom at the isocenter 108 cm from the BAMS exit window with the block placed 2 cm in front of the phantom surface. A parallel 100 MeV proton beam with a lateral field size of 40×40 mm^2 and a homogeneous fluence of $5 \cdot 10^7$ cm^{-2} is used. In the beam direction 250 bins of 0.4 mm/bin are employed to score the MC dose by a lateral integration. The Bragg curve for the solid target is then convoluted by the theoretical value of $\sigma = 0.224$ g cm^{-2} and compared with the corresponding curve from the randomized voxel cube. A low energy proton beam is chosen for this analysis because of the more pronounced scattering effects compared to high energy protons or heavier ions.

2.4. Simulations and calculations of the lateral scattering

2.4.1. MC simulations of the lateral beam profile with and without a porous plate. A porous plate can be used as a range shifter for beam penumbra reduction. A certain beam energy can be replaced by a higher energy for the same penetration depth in the patient combined with a porous plate positioned in close proximity to the patient. This configuration helps to reduce the scattering in the BAMS, thus leading to a smaller lateral beam profile at the isocenter as

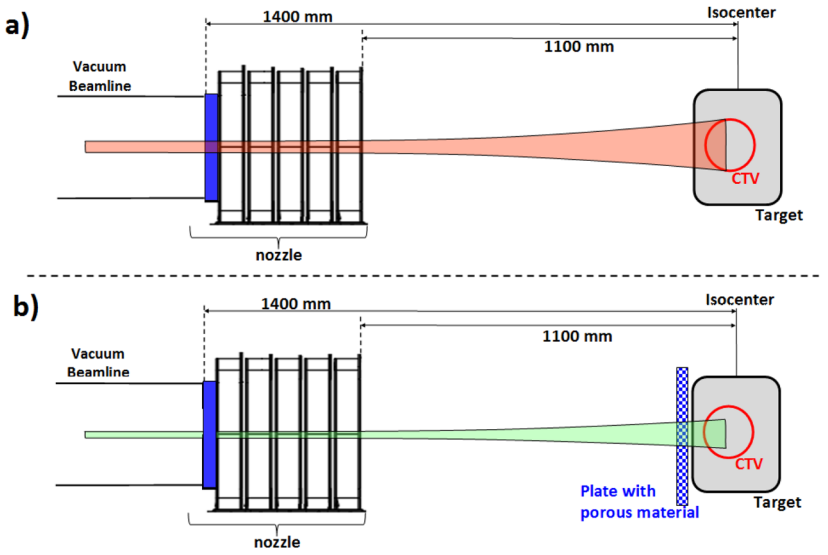

Figure 3. Schematic drawing of the scattering of a proton beam for a no-plate setup with a lower initial energy (a) compared to a setup with a porous plate positioned very close to the patient with a higher initial beam energy (b).

already shown for non-porous range shifter plates (Titt *et al* 2010). The concept is schematically shown in figure 3.

To prove this, MC simulations for proton beams are used to find the lateral FWHM values for a setup with and without a 50 mm LN300 porous plate in the beam path. This thickness is chosen for consistency with section 2.3.3. For the setup with the LN300 block, beam energies of 75 MeV, 100 MeV and 125 MeV are selected and the corresponding beam energies for the setup without the block are then calculated to be 60.5 MeV, 88.5 MeV and 115.6 MeV, yielding the same estimated CSDA ranges in water of 3.1 cm, 6.2 cm and 9.9 cm (ICRU 2005). The FWHM values are obtained from Gaussian fits to dose distributions scored at the BP position in a water phantom representing the patient in a plane perpendicular to the beam axis. The environment is set to air. Multiple simulations are performed with a variable distance between the porous plate and the water phantom. For the sake of simplicity, the block is simulated as having a homogeneous LN300 composition and as will be shown in section 2.4.2, the difference in the multiple scattering between a porous and a solid plate with the same mean areal mass t is negligible.

2.4.2. Multiple scattering of porous versus non-porous materials. Particles passing through a porous material have different path lengths corresponding to the equations in section 2.1 and therefore the lateral scattering is not uniform over the target. This can be calculated in analogy to the BP modulation. We will show in this work that, as stated above, the difference in the scattering effect of a porous versus a non-porous block having the same mean water-equivalent thickness t is negligible.

For a porous and a non-porous material with the same composition and value of t we calculate the modulation effect of the scattering in an analytical way using the Moliére theory (Moliére 1948) as well as by MC simulations. A 100 MeV proton beam was chosen for this analysis for consistency for the longitudinal calculation of section 2.3.3.

The Moliére angular distribution $f(\theta, t)$ of particles having travelled through a target of thickness t is calculated following the methods described in the equations (1)–(23) in

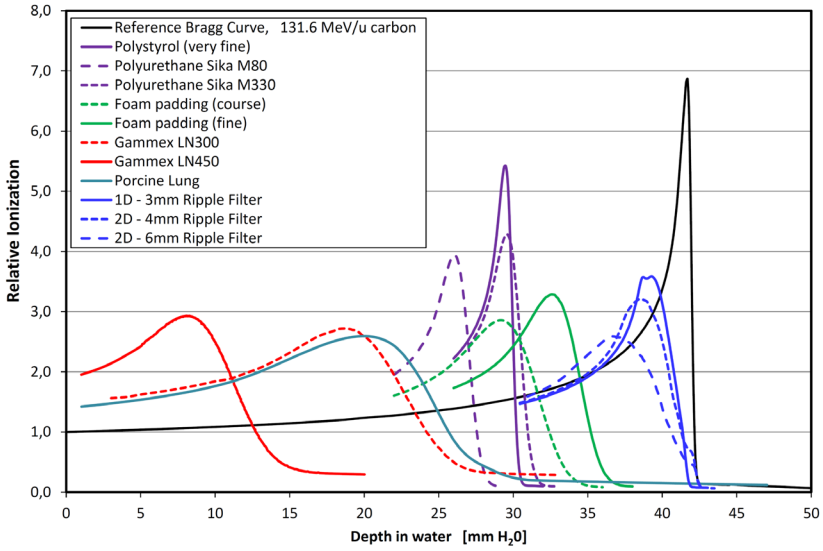

Figure 4. Measured BP enlargement of a carbon-12 beam passing through different porous materials as well as through varios RiFis. See table 1 for the characteristics of the material samples.

Gottschalk *et al* (1993). Thus, the distribution $f(\theta, t)$ can be expressed in dependency of the parameter t, which in our model is the thickness of material the beam passes through. In order to calculate the modulation of scattering by the porous material we perform—in analogy to equation (5)—a numerical convolution of $f(\theta, t)$ with the probability function for the thickness t described in equation (3):

$$f_{\mathrm{mod}}(\theta, t) = \int_{-\infty}^{\infty} f(\theta, t') \frac{1}{\sqrt{2\pi}\,\sigma} \exp\left(\frac{-(t-t')^2}{2\sigma^2}\right) \mathrm{d}t' \tag{7}$$

This formula describes then the superposition of the angular distributions for the various path lengths in the porous material. This superposition was calculated for a porous LN300 plate with $D = 50\,\mathrm{mm}$, $t = 1.42\,\mathrm{g\ cm^{-2}}$ and $\sigma = 0.224\ \mathrm{g\ cm^{-2}}$ (compare section 2.3.3). The obtained distribution is then compared with the non-modulated distribution $f(\theta, t)$ for the non-porous plate with the same value of t.

For the MC simulation of the angular distribution, in analogy to section 2.3.3, the same beam and setup as for the simulation of the Bragg curves are used. For the porous plate a randomized (porous) binary voxel cube of the LN300 composition is again used and for the non-porous plate the simulation is repeated for a 14.2 mm non-porous block of LN300. The angular distribution is scored for all protons passing the plate in question with 400 bins in 0.4 mrad steps. A residual energy $E > 20\,\mathrm{MeV}$ is used, which is assumed to filter out non-relevant low-energy target fragments.

3. Results

3.1. Analysis of Bragg curve measurements

The carbon-12 Bragg curve measurements are shown in figure 4 for all the measured material samples and RiFis. From these curves the modulation parameters of the different materials could be obtained (section 2.3.1), including P_{mod}, the newly defined material parameter which

Table 1. Measured characteristics of different porous materials resp. lung tissue. The modulation parameters for three different RiFis are shown for comparison. Note that the P_{mod} values for the RiFis do not have the character of a material parameter. In the table the acronym np stands for non-porous. The uncertainties of the measured D and ρ are estimated to 1% resp. 2% for all samples apart from the porcine lung where 10% is estimated. The errors of the fits are estimated for t to be 0.02 g cm^{-2} and for σ up to 5%, resulting in a P_{mod} uncertainty of up to 6%. The uncertainties of d are 20%.

Material	D (mm)	ρ (g cm^{-3})	ρ_{mean} H_2O (g cm^{-3})	σ H_2O (g cm^{-2})	t H_2O (g cm^{-2})	d H_2O (μm)	P_{mod} H_2O (mg cm^{-2})
Polystyrol foam (fine)	394	0.034	0.031	0.023	1.22	5	0.44
Polyurethane Sika M80	195	0.081	0.078	0.066	1.52	30	2.80
Polyurethane Sika M330	51	0.232	0.0231	0.059	1.17	40	3.00
Foam padding (coarse)	400	0.029	0.028	0.169	1.12	260	25.5
Foam padding (fine)	270	0.030	0.030	0.128	0.81	210	20.2
Gammex LN300	70	0.300	0.284	0.265	1.99	490	35.3
Gammex LN450	70	0.450	0.442	0.214	3.10	270	14.8
Porcine lung	63	—	0.300	0.317	1.89	760	53.3
1D-3 mm RiFi	3	—	np	0.084	0.20	np	(35.9)
2D-4 mm RiFi	4	—	np	0.120	0.22	np	(65.8)
2D-6 mm RiFi	6	—	np	0.174	0.34	np	(89.6)

gives the modulation effect of the porous targets. The measured material samples are listed in table 1 with the corresponding modulation parameters. The values for the parameters t, σ, ρ_{mean}, d and P_{mod} are all given in a water-equivalent scale. The errors of t and σ are conservatively estimated by the differences between the RMS calculation method and the (applied) Gaussian fitting method with an added 0.01 g cm^{-2} uncertainty of the peakfinder for t. Values of t remain very precise since they are related only to the peakfinder measurements while the relatively high uncertainty for D of the porcine lung measurements is related to the fact that its exact geometry is not known. The errors of d are as high as 20% due to the large uncertainties in the model parameters p and ρ_{mat}.

3.2. Monte Carlo simulations of the Bragg curve modulation

To validate the mathematical binary voxel model described in section 2.1, the MC simulated proton Bragg curve of a beam passing through a porous LN300 block is compared to a modulated Bragg curve obtained by the convolution with $P(x|\sigma, t)$ of a 'pristine' Bragg curve for a beam passing through a non-porous block, the latter representing the modulation effect predicted by the model. The result is given in figure 5. The figure shows two simulated Bragg curves from setups with either a solid or porous LN300 block in the beam path (solid and dashed blue lines respectively) and a third Bragg curve (violet) calculated for comparison by a convolution of the solid material Bragg curve with $P(x|\sigma, t)$, where $\sigma = 0.224$ g cm^{-2} is the parameter value from the binary voxel model in section 2.1. We opted for convoluting a Bragg curve of a beam passing through a solid non-porous block in order to have the corresponding range shift in the depth of the water phantom included in the convoluted Bragg curve as well for a direct comparison. A very good agreement between the simulated (dashed blue) and the calculated (violet) Bragg curve proves the validity of the binary voxel model. A 1D gamma acceptance test (Low *et al* 1998) for a quantitative comparison of both curves yields 100% dose points that fulfil $\gamma < 1$ for an acceptance criterion with a dose deviation ΔD of 0.03 (relative dose units of the figure) and a DTA of 0.2 mm.

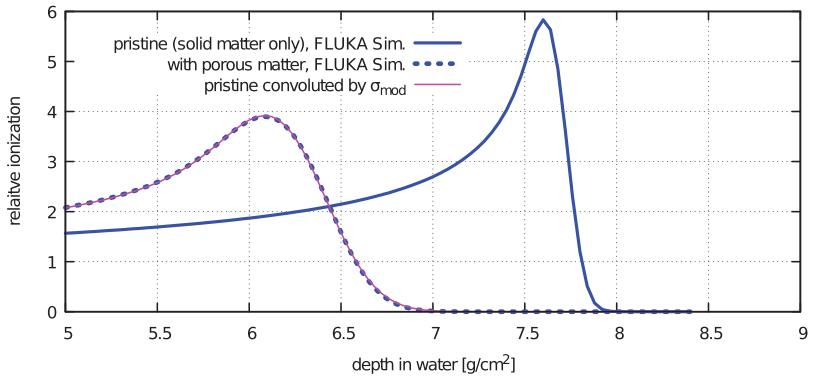

Figure 5. MC Simulated Bragg curves for proton beams with rigid (solid blue) or porous (dashed blue) materials in the beam path as well as a calculated modulated Bragg curve obtained by convolution of the curve with no porous material with a calculated $P(x|\sigma,t)$ (violet).

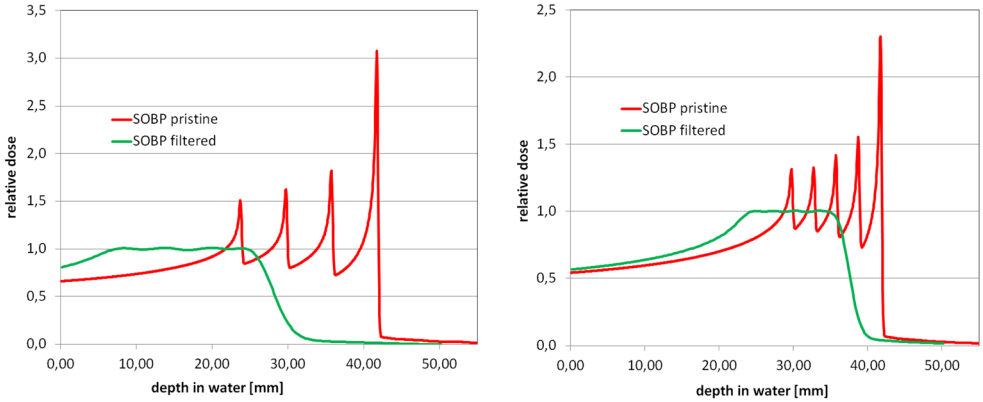

Figure 6. Calculated SOBPs for carbon ions as superpositions of shifted BPs based on the measured 131.6 MeV u^{-1} pristine BP (red curves) and calculated filter effect on the ripple of superimposed BPs modulated with $P(x|\sigma,t)$ functions corresponding to a LN300 plate of 20 mm (left figure) and 50 mm (right figure) thickness (green curves). The left figure shows SOBPs with 6 mm energy step sizes whereas the corresponding figure with 3 mm energy step sizes is displayed on the right.

3.3. The filter effect on spread-out Bragg peaks for porous plates

From the calculated filtered SOBPs made with superimposed BPs we found that D-values of 20 and 50 mm for the LN300 lead to SOBPs with less than 1% dose homogeneity in the plateau region for 3 and 6 mm energy step sizes in water, respectively (see section 2.3.3). This is shown in figure 6. Calculated SOBPs with the same energy step sizes and no plates are additionally shown for comparison, which both show a very strong ripple in the dose distribution not acceptable in a clinical setting. LN300 plates with these two values of thickness would thus lead to the same filter effect as a 1D 3 mm RiFi and a 2D 6 mm RiFi, respectively. For the filtered SOBPs, the depths vary due to the water-equivalent displacement of BPs caused by the additional material in the beam path and in a clinical setting higher energies would be needed for the same in-depth coverage. This can be beneficial as shown in the next section.

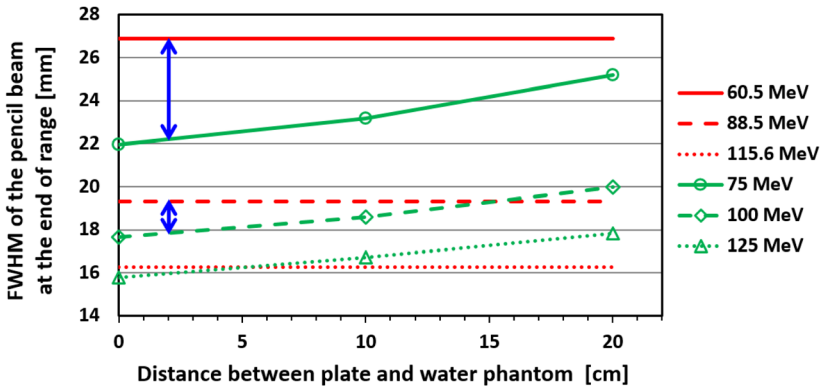

Figure 7. Simulation of the beam FWHM for protons at the BP position as a function of the distance between a 50 mm LN300 plate and the water phantom surface. In red the lines of the cases without plate are shown, whereas the green curves correspond to the data from the simulations with the porous plate. The blue arrows indicate the beam width reduction for a distance of 2 cm (by way of example) between the plate and the phantom surface.

The calculated SOBPs are for proof-of-concept only but since it has been shown that small superficial targets represent worst case scenarios for RiFis in terms of performance, (Ringbæk *et al* 2014), the filter effect of the LN300 plates is assumed to be even better than shown in figure 6 for (more clinically realistic) deeper seated and larger targets.

3.4. Porous plates as range shifters

In figure 7 simulated FWHM values of the lateral beam profile for proton beams are plotted for the two different types of setup illustrated in figure 3. All values are obtained at the BP positions. A 50 mm LN300 plate is used since this specific material and thickness lead to a BP enlargement similar to that of a 2D 6 mm RiFi (see figure 6). The FWHM values for the setup with the plate vary as a function of the separation between the water phantom and the porous plate, in contrast to the FWHM for the setup with no plate. It is seen when comparing the FWHM values of figure 7 at small separations how the porous plate functions as a range shifter, reducing the width of the lateral beam profile compared to a lower energy and no plate. As chosen examples highlighted in the figure, the net beam-width reduction for a distance of 2 cm between the plate and the target surface is 4.7 mm (or a 21.4% reduction) for a 75 MeV beam with the plate and 1.4 mm (or a 7.3% reduction) for a 100 MeV beam. The case for 125 MeV only shows a very limited beam width reduction for distances of less than a few cm from the plate and does in fact lead to larger beam widths for larger distances. This implies that the gain in beam width reduction by using a porous plate of the thickness shown in this example is only noteworthy in treatment cases with penetration depths smaller than $\approx$10 cm.

3.5. Scattering of porous versus non-porous materials

Figure 8 shows angular distributions of a 100 MeV proton beam passing through a porous versus a non-porous target of the LN300 composition both with the same mean thickness of $t = 1.42\,\mathrm{g\ cm^{-2}}$ (section 2.3.3). The angular distributions are calculated with the Moliére

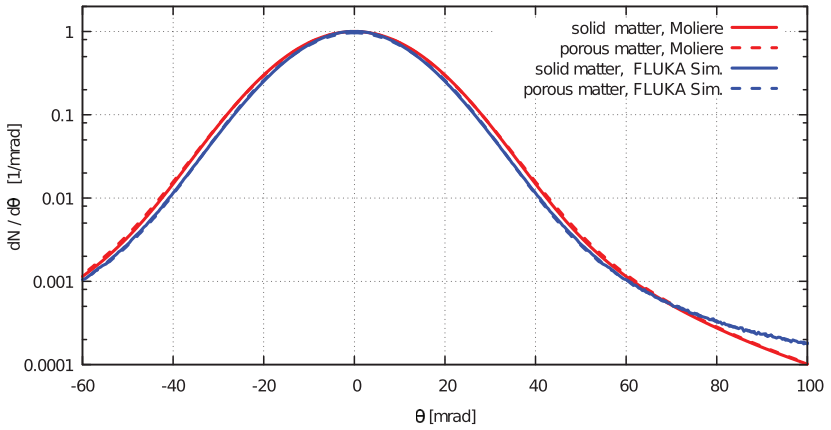

Figure 8. Comparison of the calculated angular distribution of a 100 MeV proton beam passing though a porous versus a non-porous target of the LN300 composition of the same mean density ρ_{mean}. The comparison is performed by an analytical calculation using the Moliére multiple scattering theory (red) compared to angular distributions from FLUKA MC simulations using a porous CT voxel cube (blue), once with binary voxels with two different densities (as in figure 1) and once with uniform voxels with the same density for targets with the same thickness in g cm^{-2}.

multiple scattering law (red curves) in addition to being simulated in FLUKA (blue curves). For the MC data sets the statistical uncertainty is estimated to be $<0.1\%$ for the BPs and between 0.1 and 2% for the angular distribution. It is seen how the angular distributions for the porous versus the non-porous targets are in general in good agreement, which leads to the conclusion that the porosity has only a negligible effect on the total multiple scattering. While there is no relevant difference in the lateral scattering effect between porous and non-porous materials when comparing the angular distributions, a slight difference can be seen at $\theta > 70$ mrad between the blue and the red curve, meaning between the two different multiple scattering models (FLUKAs build-in Moliére scattering algorithm MSC versus theoretical Moliére calculations following Gottschalk). This is assumed to be in particular due to differences in how the algorithms handle large-angle inelastic nuclear scattering events. This however is a side-result with no importance to the overall conclusions of this paper.

4. Discussion

This work confirms by experiments and MC simulations that porous materials with microscopic structures (foam, sponges, lung tissue and lung substitutes) in the beam path result in a much stronger energy straggling than what is expected for non-porous materials of the same geometrical thickness and molecular composition. We have shown that this effect can be theoretically described with a binary voxel model for all porous materials and that it depends on the size of the pore structure d, the density ρ_{mean} and the thickness of the porous material D. The modulation power P_{mod} is established to quantify the modulation effect of a given porous material and can be used to estimate the modulation effect of any thickness of said material. That the low-density voxels in our binary voxel model are simplified to vacuum instead of air or gas has no relevance within the uncertainties of the estimated modulation parameters. While the binary voxel model is in very good agreement with reality for the porous plates, for more complex biological materials macroscopic structures (such as larger blood vessels and

air tubes for the lung) are present at certain pathways, leading to effects that do not return a normal-distributed BP convolution. As shown elsewhere (Witt 2014), P_{mod} varies from 33.0 to 75.0 mg cm^{-2} for various beam paths through the lung due to these macroscopic structures. This does not influence the findings presented here but when looking into the effect of the lung in detail it cannot be ignored.

Measurements and simulations show that porous plates can function as a RiFi in raster scanning beam applications. Using a RiFi, or alternatively a block of porous material, reduces the number of times that the accelerator has to change the energy of the ion bunch. This is the most critical aspect in terms of irradiation time. A plate of 20 mm thickness of the Gammex lung substitute material LN300 would lead to a BP enlargement similar to that of the in-use 3 mm thick RiFi. A 50 mm plate of this material would even allow 6 mm accelerator energy steps, matching the results achieved with the new thicker 2D RiFi design, which has recently been shown to be applicable in treatment planning (Ringbæk *et al* 2016).

Introducing a range shifter in the beam path close to the patient makes it possible to select a higher beam energy for the same penetration depth within the patient as would be obtained without the range shifter and with a lower energy. This in turn decreases the scattering effect in the BAMS and reduces the lateral width of the beam as a result. A porous plate can be positioned directly in front of the patient without inducing a fluence inhomogeneity at the surface of the patient or a dose range inhomogeneity within the patient, where for a normal RiFi a certain distance (of minimum 60–70 cm for high-energetic carbon ion beams or 15–20 cm for high-energetic proton beams) is needed in order for lateral scattering effects to blur out these inhomogeneities (Weber and Kraft 1999, Ringbæk *et al* 2014, Ringbæk *et al* 2015). A porous plate can therefore work as a range shifter additionally to a RiFi. This is of particular interest for proton beam therapy, where the physical nature of the particle leads to a larger scattering effect. Up until now, RiFis have not been used in proton beam treatments for exactly this reason. However, we expect that filter setups which would make 6 mm energy steps possible, such as 2D 6 mm thick RiFis or selected blocks of porous materials, could be beneficial in proton treatments too. Treatment planning with protons and thicker RiFis will be the topic of an up-coming investigation. The range shifter concept was found to be mainly beneficial in treatments of tumours at low penetration depths, which corresponds to the findings of Titt *et al* (2010).

While the RiFi role of porous plates is shown with both measurements and simulations, the range shifter role is shown only by simulations, which is related to the fact that this part of the study was added after the round of experiments had been conducted. However, since MC codes (like FLUKA) present the capability to import and process DICOM files (Mason 2011) and converting them to a 3D binary voxel grid similar to our mathematical model, the binary voxel model could be validated with simulations for the Bragg curves. This in turn is thought to prove that the model is valid also for the lateral scattering effect. Furthermore it was shown with simulations and calculations that the difference in the lateral scattering effect for a porous material compared to a solid one with the same water-equivalent thickness is negligible and that simulations using solid materials are a valid approach in order to investigate the lateral beam profile of porous materials, such as when showing the aptitude of porous plates as range shifters.

Even though porous plates yield the same benefit as an established RiFi in terms of the BP enlargement it is important to note that RiFis are advantageous in some situations over the porous plates and vice versa. The shape of a RiFi is optimized to produce a maximum filter effect on the dose ripple with the minimum possible mass. To reach the desired filter effect, a $P(x|\sigma,t)$ function is used where the x-range of $P(x|\sigma,t)\neq 0$ (representing the thickness of the object) is as small as possible. In other words, the RiFi shape does not use the outer Gaussian

tails of the $P(x|\sigma,t)$ function for the modulation. A porous plate cannot be optimized in this way or designed specifically for the filter effect and therefore more material is required to obtain the same effect. As an example, a 20 mm LN300 plate yields the same filter effect as a 3 mm thick RiFi but has a mass thickness of 0.57 g cm^{-2} whereas the RiFi has only 0.2 g cm^{-2} (see table 1). If the LN300 plate was placed at the end of the BAMS where the RiFi is normally installed, a flat SOBP would indeed be obtained for the same number of energy steps but with much more enlarged beam spots and therefore a much worse conformity. On the other hand, as mentioned above, RiFis cannot be attached close to the patient but porous plates can. This means that one should either use a RiFi at the nozzle or a porous plate close to the patient (with the additional benefit of the range shifter effect for the latter case).

The Gammex LN300 lung substitute material is used in this work as a proof-of-concept example but similar results would have been found for other commercial porous foams. A quality assurance and an accurate characterization of at least P_{mod} and the physical density of the used plates are required before they can be applied in treatment planning. The density can be easily measured or obtained from technical manuals while P_{mod} values can be obtained with Bragg curve measurements following the method described in this work. Such measurements should anyway be performed in relation to the quality assurance and commissioning of any new implementation in a clinical setting together with measurements of the lateral beam profile. To be usable in raster scanning treatments the lateral uniformity of the material must be experimentally confirmed, checking that values of P_{mod} are the same for different pathways within the porous material in question and even though no such checks were carried out in this work, commercial foams should in general fulfil this criteria. The width of the distal fall-off of the SOBPs achieved with the chosen porous plate(s) should also be considered in the commissioning phase. Due to the relatively large thickness of porous material required for a proper filtering effect, the distal fall-off is larger than when a solid range shifter is used. However it is important to remind the reader that the strength of the porous plate solution is that it works combined as a RiFi and as a range shifter at the same time. If the range shifter effect alone is wanted, the authors would opt for an established solid range shifter as proposed by Titt *et al* (2015). The increase of the dose fall-off follows directly from the desired broadening of the BP, which is required when larger and fewer iso-energy steps are wished for. The deterioration in the lateral dose fall-off versus larger iso-energy step sizes (e.g. planning conformity versus treatment time reduction) is by itself an important topic. It might set some limitations on the clinical usage in specific patient cases were radiosensitive normal tissue or organs-at-risk are located right at the end of the SOBP. But this is related not only to porous plates but to RiFis in general and has been covered in detail in our previous work (Ringbæk *et al* 2016).

A detailed study of the lung findings is not presented in this work but measurements show that the distal dose fall-off (90–20%) of the beam modulated by the porous lung structure is increased by up to 5 mm (Witt 2014). This also agrees with the findings of Titt *et al* (2015). The BP enlargement, and especially the enlargement of the distal fall-off, created by the 'porous' effect of the lung therefore plays an important dosimetric role for the clinical treatment planning; an effect that has up to now not been considered in any commercial TPS.

5. Conclusion

A binary voxel model describing the beam modulating effect of porous materials with microscopic structures has been developed and used to obtain the newly defined modulation power P_{mod} for all investigated materials.

Bragg curve measurements show that porous plates of different materials, such as foams or lung substitutes, have a beam modulating effect similar to those seen by RiFis, which enlarges the BP and as a results reduces the accelerator energy shifts necessary to homogeneously cover the PTV. Due to the much higher mass distribution for the same modulation effect for porous plates compared to RiFis however, porous plates should be placed close to the patient. MC simulations have been used to show that the porous plates could in addition be used as range shifters in proton beam treatments, where by allowing the choice of a higher initial beam energy for the same penetration depth a smaller lateral beam profile can be obtained.

As an example of an established block of porous material commercially available to treatment facilities, we used the lung substitute material Gammex LN300. A 20 mm LN300 plate could replace the in-use 3 mm thick RiFi of the 1D design while a 50 mm plate could replace a RiFi making 6 mm energy step sizes possible. Placing them a few centimeters in front of the patient reduces the beam width in proton treatments with approximately 20% for very superficially located tumors at a few cm depth and with 7–10% for tumors at 6–7 cm penetration depth.

Newer thicker RiFis could be applicable in proton therapy too. For proton treatments of superficially located tumours however, such RiFis might result in an unacceptable large broadening of the lateral beam spot sizes due to the required low beam energies. Especially in such treatments, using a block of porous material as a combined RiFi and range shifter to reduce the irradiation time and decrease the beam spot sizes at the same time would be beneficial.

Acknowledgments

The author T P Ringbæk acknowledges the financial support of Zentrales Innovationsprogramm Mittelstand (ZIM) from the German Ministry of Economics, grant number KF2829804AK2. The authors acknowledge the providing of beamtime with corresponding technical support at HIT; thanks are especially given to Stephan Brons and Thomas Haberer. The authors additionally acknowledge the FLUKA forum for insightful and fruitful discussions as well as Alina Santiago for her careful proof-reading.

References

Böhlen T T, Cerutti F, Chin M P W, Fasso A, Ferrari A, Ortega P G, Mairani A, Sala P R, Smirnov G and Vlachoudis V 2014 The fluka code: developments and challenges for high energy and medical applications *Nucl. Data Sheets* **120** 211–4

Bohr N 1915 The penetration of atomic particles through matter *Phil. Mag.* **6** 581

Gottschalk B, Koehler A M, Schneider R J, Sisterson J M and Wagner S M 1993 Multiple coulomb scattering of 160 mev protons *Nucl. Instrum. Methods* B **74** 467–90

Haberer T, Becher W, Schardt D and Kraft G 1993 Magnetic scanning system for heavy ion therapy *Nucl. Instrum. Methods* A **330** 296

ICRU 1994 Icru: Report 49 stopping powers and ranges for protons and alphs particles *Technical Report* (Bethesda, MD: International Comission on Radiation Units and Measurements)

ICRU 2005 Icru: Report 73 stopping of ions heavier than helium *Technical Report* (Bethesda, MD: International Comission on Radiation Units and Measurements)

Kraft G and Weber U 2011 Tumor therapy with ion beams *Handbook of Particle Detection and Imaging* vol 1, ed C Grupen and I Buvat (Berlin: Springer) ch 47, p 1179

Low D A, Harms W B, Mutic S and Purdy J A 1998 A technique for the quantitative evaluation of dose distributions *Med. Phys.* **25** 656–61

Mason D 2011 Su-e-t-33: Pydicom: an open source dicom library *Med. Phys.* **38** 3493

Moliére G 1948 Theorie der streuung schneller geladener Teilchen II. Mehrfach- und Vielfachstreuung *Z. Naturforsch.* **3a** 78

Ringbæk T P *et al* 2015 Fluence inhomogeneities due to a ripple filter induced moiré effect *Phys. Med. Biol.* **60** N59–69

Ringbæk T P, Weber U, Santiago A, Simeonov Y, Fritz P, Krämer M, Wittig A, Bassler N, Cabillic-Engenhart R and Zink K 2016 Dosimetric comparisons of carbon ion treatment plans for 1d and 2d ripple filters with variable thicknesses *Phys. Med. Biol.* **61** 4327–41

Ringbæk T P, Weber U, Thomsen B, Petersen J B B and Bassler N 2014 Monte Carlo simulations of new 2d ripple filters for particle therapy facilities *Acta Oncol.* **53** 40–9

Sawakuchi G O, Titt U, Mirkovic D and Mohan R 2008 Density heterogeneities and the influence of multiple coulomb and nuclear scatterings on the Bragg-peak distal edge of proton therapy beams *Phys. Med. Biol.* **53** 4605–19

Tissue Characterization Phantom Model 467: User Guide 2004 *Technical Manual* (Middleton, WI: Gammex)

Titt U, Mirkovic D, Sawakuchi G, Perles L, Newhauser W D, Taddei P and Mohan R 2010 Adjustment of the lateral and longitudinal size of scanned proton beam spots using a pre-absorber to optimize penumbrae and delivery efficiency *Phys. Med. Biol.* **55** 7097–106

Titt U, Sell M, Unkelbach J, Bangert M, Mirkovic D, Oelfke U and Mohan R 2015 Degradation of proton depth dose distributions attributable to microstructures in lung-equivalent material *Med. Phys.* **42** 6425

Weber U and Kraft G 1999 Design and construction of a ripple filter for a smoothed depth dose distribution in conformal particle therapy *Phys. Med. Biol.* **44** 2765–75

Weber U, Kraft G and Zink K 2014 Benefit of reducing the distance between patient and nozzle and usage of a range shifter *Int. J. Part. Ther.* **1** 462–3

Witt M 2014 Modulationseffekte von kohlenstoffionen bei der bestrahlung von lungen *Master's Thesis* Technische Hochschule Mittelhessen

Witt M, Weber U, Kellner D, Engenhart-Cabillic R and Zink K 2015a Optimization of the stopping-power-ratio to hounsfield-value calibration curve in proton and heavy ion therapy *Z. Med. Phys.* **25** 251–63

Witt M, Weber U, Simeonov Y and Zink K 2015b U-e-t-671: range-modulation effects of carbon ion beams in lung tissue *Med. Phys.* **42** 3491

Supplementary Material

Appendix A. The energy loss straggling of solid material

The intrinsic energy loss straggling in the solid part of a given material (meaning either the entirety of a rigid block or the high-density parts of a porous block) has a similar but not as strong a modulation effect as the straggling of the porosity of porous materials. In this supplementary material section we will try to estimate this effect for comparison. Since we in this work talk about two different kinds of energy straggling (from solid parts and porous parts of a material, respectively), the estimation of a practical formula for $P_{mod,straggl}$, the modulation power from the energy straggling, is thought to be helpful to the reader, although not necessary to understand our results.

The energy loss straggling can be approximated by the standard Bohr formula, which gives the quantity σ_E, which describes the width of the normally distributed fluctuations of the energy loss (ΔE – ΔE_{mean}) from a particle passing through the target with thickness t:

$$\sigma_E^2 = (0.157 \cdot t \cdot Z_1^2 Z_2)/A_2 \tag{A.1}$$

with σ_E in [MeV/u] and t in [g/cm^2], where Z_1, A_1 and Z_2, A_2 are the charge and mass numbers of the projectile and target atoms, respectively. When the target consists of water molecules (as is assumed to be the case here), Z_2 and A_2 is 10.0 and 18.0 respectively. For other materials than water, the electron density can be scaled by $(A_2/Z_2)/1.8)$.

This Bohr formula can then be combined with a rough formula from fitted data of ICRU 49 for the CSDA range of ions in matter being valid for therapy energies from 1 to 500 MeV/u: $R(E) = 2.56 \cdot 10^{-3}(A_1/Z_1^2)E^{1.74}(A_2/Z_2)/1.8$ with E being the initial beam energy in [MeV/u]. The ICRU range-in-water-fit was originally performed by Sjirk Niels Boon in his PhD work from 1998 (Dosimetry and quality control of scanning proton beams. University of Groningen: s.n., PhD thesis, 1998. p. 176).

Combining the derivation of $R(E)$ with the Bohr formula delivers a formula for $\sigma_R(E)$

$$\sigma_R(E) = \frac{dR(E)}{dE} \cdot \frac{\sigma_E}{A_1} \tag{A.2}$$

where the term $1/A_1$ comes from the fact that we measure E in [Mev/u]. The formula for $\sigma_R(E)$ then describes the width of the normally distributed fluctuation of the particle range within the target (range – range$_{mean}$) for a particle with the the initial energy E. If we then define $P_{mod,stragg}$ in a similar manner to P_{mod}:

$$P_{mod,straggl} = \frac{\sigma_R(E)^2}{t} \tag{A.3}$$

we obtain a practical approximate formula of the modulation power from the energy straggling:

$$P_{mod,straggl}(E) \approx 10^{-6} \frac{(E[MeV/u])^{(3/2)}}{Z_1^2} \frac{A_2}{Z_2} \quad [g/cm^2] \tag{A.4}$$

In contrast to the porous materials, this modulation power depends on the energy and the ions species. For a 150 MeV proton beam in water $P_{mod,straggl} \approx 3.3$ mg/cm^2, whereas for a 280 MeV/u carbon-12 beam (having the same range in water) $P_{mod,straggl} \approx 0.23$ mg/cm^2.

It should be noted that the P_{mod} of porous materials as defined and measured in this work does not contain the energy loss straggling of $P_{mod,straggl}$ since P_{mod} is determined by comparison (unfolding) of the non-porous Bragg curve with the porous one, both of which contain the full energy loss straggling. For the estimation of the total range straggling, P_{mod} and $P_{mod,straggl}$ should be added.

7. Appendix

7.1 Academic Faculty

Here is listed the personnel who directly or indirectly in teachings prior to the dissertation work or private conversations during the dissertation work has been of assistance.

In Marburg

K. Zink

R. Engenhart-Cabillic

A. Wittig

G. Iancu

A. Santiago

Y. Simeonov

At the GSI

U. Weber

C. Graeff

M. Krämer

S. Hild

In Aarhus

N. Bassler

J. B. B. Petersen

S. P. Møller

B. Thomsen

7.2 Acknowledgments

First of all I would like to thank my supervisors for making this thesis possible. I thank my first supervisor Prof. Dr. Klemens Zink for believing in the project and for investing a lot of energy and time in solving all sorts of problems, scientific as well as bureaucratic. In addition I thank my second supervisor Prof. Dr. Rita Engenhart-Cabillic for the support and the backing.

A very special thank goes out to Dr. Uli Weber, whose ideas laid the foundations for this thesis and who has been a continuous source of advice and help all around the clock. His aid with getting myself established in Marburg when first I arrived here has been invaluable and even though guided tours to “der römische Limes” and trips in “der Frankfurter Ebbelwoi-Express” have not been strictly mandatory for the dissertation work, it sure feels that way.

I also thank Dr. Niels Bassler for all contributions to this work, including being available for questions and for making SHIELD-HIT12A available, functional and fresh, as well as for introducing me to the world of particle therapy in the first place and to teach me the importance of beer drinking in a research context.

I acknowledge the support from all colleagues who have in one way or another contributed to the creation of this thesis, in particular thanks are given to Dr. Michael Krämer for the access to TRiP98 and the support for everything TRiP-related, to Dr. Gheorghe Iancu for the one year of office sharing in which multiple questions were asked and answered and to Yuri Simeonov who additionally to lending an ear to scientific discussions introduced kicker and table tennis as obligatory (and helpful) parts of my work routine.

Thanks are due to all staff at the Philipp university in Marburg, the university hospital of Marbug-Gießen and the university of applied science Gießen-Friedberg, most off all to Dr. Christina Zinecker for her helpfulness and availability.

I acknowledge the financial support of Zentrales Innovationsprogramm Mittelstand (ZIM) from the German Ministry of Economics, grant number KF2829804AK2, granted to Dr. Weber and Prof. Dr. Zink, under which this dissertation was financed. I furthermore acknowledge the support from Promotionsabschluss-Finanzierung, Strategischer Forschungsfonds der THM, for the last half a year of financial support.

I thank my family and of course my parents, although their only real contribution to this

work has been to give birth to me and raise me to become a (moderately) responsible person.

Last but not least a very heartfelt thank is due to Alina for being a constant personal support as well as available at all times for complaints, scientific discussions, insightful comments and encouragements and of course to our son Leo for integrating into the mix of the dissertation work a routine of nappy-changes and frequent swaying. Both have provided me with a near-endless amount of laughter and smiles.

As the very last, in the revised edition, I would like to include in the acknowledgements my daughter Chloe, born between the time of the dissertation submission and the disputation, who was a big help in the preparation for the actual defence by letting her disagreements with my slide-show be heard as loud, consistent crying and whose charming and smiling personality is a valuable mood changer. She is sitting on my lap as I write these very words.